CREATION AND IMPAIRMENT OF HYDRAULIC FRACTURE CONDUCTIVITY IN SHALE FORMATIONS

A Dissertation

by

JUNJING ZHANG

Submitted to the Office of Graduate and Professional Studies of
Texas A&M University
in partial fulfillment of the requirements for the degree of

DOCTOR OF PHILOSOPHY

Chair of Committee,	A. Daniel Hill
Committee Members,	Ding Zhu
	Eduardo Gildin
	Judith S. Chester
Head of Department,	A. Daniel Hill

August 2014

Major Subject: Petroleum Engineering

ABSTRACT

Multi-stage hydraulic fracturing is the key to the success of many shale gas and shale oil reservoirs. The main objectives of hydraulic fracturing in shale are to create artificial fracture networks that are conductive for oil and gas flow and extensive into the reservoir for high and long-lasting production, while economical to keep the well commercial.

Due to the variation in shale mineralogical and mechanical properties, mechanisms of fracture conductivity creation in shale formations are complicated. Standard fracture conductivity measurement procedures were developed for high concentration propped fractures and need to be modified to measure the conductivity of unpropped fractures and the low concentration proppant packs. Water-based fracturing fluids can interact with the clay minerals in shale and eventually impact shale fracture conductivity. All these challenges require more studies to elevate the understanding of shale fracture conductivity creation and impairment.

The aims of this work are to design an experimental framework to measure fracture conductivity created by different mechanisms, to develop a correlation calibrated by the experimental data to predict shale fracture conductivity, and to investigate the mechanisms of conductivity damage by water. We first present the laboratory procedures and experimental design that can accurately measure fracture conductivity of shale fractures. Then, a program is developed to calculate conductivity considering the physical processes that dictate propped fracture conductivity as observed

in the experiments. After the undamaged shale fracture conductivity is measured by dry nitrogen, water with similar flowback water compositions is flowed to simulate the damage process followed by the second gas flow to measure the recovered fracture conductivity after the water damage.

From this study, we find that the unpropped shale fractures are conductive up to certain closure stress by a variety of mechanisms. The correlation we develop can capture the physical processes in the shale fracture and can reasonably predict propped fracture conductivity. Shale fracture surface softening is identified as the dominant cause for the significant conductivity reduction after water flow.

The systematic study on realistic shale fracture conductivity is the foundation of well performance analysis and production history matching. The investigation on water damage can better guide the fracturing design in shale reservoirs.

DEDICATION

To my beloved and amazing wife, Yu Wang;

without her love and sacrifice,

it would be impossible for me to finish this study.

ACKNOWLEDGEMENTS

I would like to express my sincere gratitude to both Dr. A. Daniel Hill and Dr. Ding Zhu, for admitting me as a graduate student when I was puzzled over my career, for their insight into this interesting subject and the opportunity for me to study it, for their encouragement and patience when I was lost in the technical trivia and for their sharing of career and life experiences. Under their supervision and guidance, the pursuit of the PhD degree not only enhanced my research capabilities and sharpened my engineering skills, but also changed my attitude towards life and my career.

I would like to thank Dr. Eduardo Gildin for being one of my committee members. His class on numerical simulation and his personal advice has been very helpful for the theoretical part of the study.

I would also like to thank Dr. Judith S. Chester for being my committee member and for her continuous support of my work. My numerous discussions with her on microscopic description and grain failure helped to make this work complete and inspired me to pursue further studies on this subject.

Thanks to Dr. Obadare Awoleke who trained me on basic experimental skills and shared his ideas on the subject, as well as Dr. Liangchen Ouyang whose methodology and simulation work broadened the scope of this study.

I thank Anton Kamenov, Kathryn Briggs, James Guzek, and Timothy Jansen – my dear team members in the Hydraulic Fracture Conductivity group for their help and discussions on the experiments. I thank my friends in our research group, particularly Qi

Zhang, Cassandra Oeth, Roberto Martinez, Manabu Nozaki, Kai Dong, Nozomu Yoshida, for the good time we have had during the study. I thank John Maldonado for his help in the experiment.

Last but not least, I would like to give special acknowledgements to Eric R. Davis, my previous supervising manager in ConocoPhillips, for his continuous encouragement, support, and guidance throughout my early career in China and my studies in U.S.

NOMENCLATURE

a_1 to a_6	Coefficients of the selection and breakage functions, dimensionless
B	Breakage function, dimensionless
BI	Brittleness index, dimensionless
C_a	Areal proppant concentration, ML^{-2}, lbm/ft ²
C_f	Fracture conductivity, L^2L, md-ft
C_{f0}	Initial fracture conductivity, L^2L, md-ft
C_{fD}	Dimensionless fracture conductivity, dimensionless
d_{10}	Proppant diameter at the tenth percentile, L, mm
d_{50}	Median proppant diameter, L, mm
d_{90}	Proppant diameter at the ninetieth percentile, L, mm
D_H	Hydraulic diameter, L, m
e_0	Initial void ratio, fraction
e	Void ratio at certain stress, fraction
E	Young's modulus, $ML^{-1}T^{-2}$, MMpsi [pa]
h_f	Width of the sample, L, m
k_f	Fracture permeability, L^2, md [m ²]
k_m	Matrix permeability, L^2, md [m ²]
k_r	Relative permeability, dimensionless

$k_{r\alpha}$	Relative permeability of fluid α, dimensionless
$k_{r\beta}$	Relative permeability of fluid β, dimensionless
L	Length of the sample, L, m
m_P	Weight percentage of the amount of proppants for size increment of dy
M	Mobility ratio, dimensionless
M_g	Molecular mass, $MM^{-1}N^{-1}$, kg/kg mol
p_1	Inlet pressure, $ML^{-1}T^{-2}$, psi [pa]
p_2	Outlet pressure, $ML^{-1}T^{-2}$, psi [pa]
P	Cumulative percentage of proppant
q	Flow rate, V^3T^{-1}, m^3/t
R	Universal gas constant, $ML^2T^{-2}N^{-1}\Theta^{-1}$, J/mol K
S	Selection function, dimensionless
T	Temperature, Θ, K
w_0	Initial fracture width, L, m
w_1	Fracture width at certain stress, L, m
w_f	Fracture width, L, m
v	Fluid velocity in the fracture, LT^{-1}, m/s
V	Volume percentage of minerals, dimensionless
x	Grain size, L, mm
x_f	Fracture length, L, m

y	Dummy variable in the population balance equation
Z	Gas compressibility factor, dimensionless

Greek

α	Displacing fluid
β	Displaced fluid
ϕ	Porosity, fraction
ϕ_0	Initial proppant pack porosity, fraction
ϕ_1	Proppant pack porosity at certain stress, fraction
γ_P	Proppant specific gravity, dimensionless
λ	Mobility, $L^2M^{-1}LT^2T^{-1}$, md/mPa s
$\lambda_{displacing}$	Mobility of the displacing fluid, $L^2M^{-1}LT^2T^{-1}$, md/mPa s
$\lambda_{displaced}$	Mobility of the displaced fluid, $L^2M^{-1}LT^2T^{-1}$, md/mPa s
μ	Fluid viscosity, $ML^{-1}T^{-2}T$, Pa s
μ_α	Viscosity of the displacing fluid, $ML^{-1}T^{-2}T$, Pa s
μ_β	Viscosity of the displaced fluid, $ML^{-1}T^{-2}T$, Pa s
ρ	Fluid density, ML^3, kg/m^3
σ	Closure stress, $ML^{-1}T^{-2}$, psi [pa]
ψ	Phi percentile deviation, L, mm

Superscripts

i	Index for the proppant grain size increment
n	Index for the closure stress increment

TABLE OF CONTENTS

Page

LIST OF FIGURES

Page

LIST OF TABLES

Page

1 INTRODUCTION [*]

1.1 Background

Hydraulic fracturing is a stimulation method to enhance well productivity in low permeability reservoirs by injecting viscous proppant-loaded fluids at pressure exceeding the formation fracturing pressure. After the pump is shutdown, the carrying fluid leaks off into the permeable formation under the differential pressure between the fracture and the reservoir. With continuing fracture pressure fall-off, the fractures close on the proppants and the high conductivity channel for hydrocarbon flow is created. A key parameter to evaluate the quality of the fracturing job is called fracture conductivity, which is defined as the product of fracture permeability and fracture width. To obtain high fracture conductivity, various types of proppant, fracturing fluids, additives, and operational procedures have been developed.

Shale is a fine-grained, clastic sedimentary rock composed of mud that is a mixture of flakes of clay minerals and tiny fragments of other minerals, especially quartz and calcite (Blatt et al. 1996). Hydraulic fracturing in shale has more challenges and uncertainties due to the unique features of shale. Shale rocks are highly laminated and natural fractures are frequently present. During fracturing, the weak laminations and the naturally fractured planes can be activated and sheared creating certain conductivity. To obtain large contact area, smaller size proppants at much lower concentrations are

[*] Part of this dissertation is reprinted with permission from "Laboratory Measurement of Hydraulic Fracture Conductivities in the Barnett Shale" by J. Zhang, A. Kamenov, A.D. Hill, and D. Zhu. Paper SPE 163839 presented at the SPE Hydraulic Fracturing Technology Conference in the Woodlands, Texas, U.S.A., 4-6 February. Copyright 2013 by the Society of Petroleum Engineers.

commonly pumped with a large volume of water-based fracturing fluid. Shale rocks are usually clay-rich. The fracturing water can experience physico-chemical reactions with the clay minerals leading to fracture conductivity damage.

In a word, fracture conductivity creation and damage mechanisms in shale differ from the conventional reservoirs due to unique rock features and fracturing designs. It is under this background that we have conducted a systematic investigation on hydraulic fracture conductivity in shale.

1.2 Literature Review

1.2.1 Hydraulic Fracturing in Shale

The concept of hydraulic fracturing with high viscosity fluids was established after the first successful fracturing job in 1947, where gasoline-based napalm gel frac fluid was used. During the late 1960s, guar-based cross linked fluids were introduced. Since then, it has been the most popular and effective technology in the stimulation of low permeability reservoirs. Subsequently, from the mid-1970s to early 1980s, the so called "river fracs" were conducted in many Hugoton wells in Kansas where water and sand were pumped at 200 to 300 bbl/min with only a few gallons of friction reducer (Grieser et al. 2003). Today, polymer concentrations of less than 20 lb/1000 gallons are typically pumped during slick water fracturing (King 2010).

Shale gas wells are usually fractured with low concentration slurries during early stages (commonly from 0.25 to 1.0 lb of proppant per gallon of fluid, or ppga) with the "tail-in" stage increasing to 2-3.5 ppga (Palisch et al. 2010). Several authors have also

discussed the use of 0.5-1.5 ppga proppant slugs in order to control fracture fluid leakoff during shale fracturing (Wiley et al. 2004; King et al. 2008).

Small size proppants such as 100 mesh and 40/70 mesh are generally used in shale slick water fracturing. Larger proppants such as 20/40 mesh sand are often pumped during the "tail-in" stage to create increased near-wellbore fracture conductivity (Coulter et al. 2004). 100 mesh sands are also used as scouring agents and limiters of fluid loss to encountered fissures (Cramer 2008). Ultra-light weight proppants become increasingly popular in shale fracturing due to their low specific gravity and reduced amount of proppant settling during injection through tubing and into fractures. Ultra-light weight proppants resist settling and thus can be transported farther into the fractures. They are also used to exploit the advantages of proppant partial monolayer (Brannon et al. 2004; Parker et al. 2005; Palisch et al. 2010). Shale reservoir conditions and their fracturing designs are summarized in **Table 1.1**.

It has been demonstrated by the Barnett Shale play development that successful fracturing design can create sufficient conductivity and can stimulate a formation from marginal into commercial production (Shelley et al. 2008). In the Barnett Shale, hydraulic fractures are created by low viscosity fracturing fluid with low proppant concentrations. A review of over 80 published field studies have demonstrated that high conductivity fractures are less affected by multiphase flow and may provide benefit in fracturing past condensate blocks within the reservoir (Vincent 2002). Simulation results show that, with the same created fracture network volume, the scenario with 0.5 md-ft conductivity generates very large pressure drops leading to 20% less effective fracture network after one year compared with a 5 md-ft scenario (Mayerhofer et al. 2006).

There is speculation about the increased conductivity due to displacement of fracture walls created from slick water fracturing (Fredd et al. 2001). The increase in conductivity is produced because the fracture faces no longer match up when the fracture closes. Laboratory and field tests have reported residual fracture widths that can be attributed to the combined effects of surface roughness and fracture displacement of the rock (Branagan et al. 1996; van Dam et al. 1999).

Table 1.1–Summary of the shale reservoir conditions and fracturing designs.

Properties	**Barnett Shale**	**Fayetteville Shale**	**Eagle Ford Shale**	**Marcellus Shale**
True Vertical Depth (ft)	6000~8500	1500~6500	5000~14000	4000~8000
Closure stress gradient (psi/ft)	0.61-0.73	0.59~0.7	0.7~0.95	0.67~0.76
Effective closure stress (psi)	3000~5500	1000~5000	2000~8000	2500~6000
Hydrocarbon	Gas	Gas	Condensate, oil	Gas, condensate
Fracturing design	Water frac	Water frac	Gelled frac, hybrid, high-way	Water frac, foam
Proppant size (mesh)	100, 40/70, 30/50	100, 30/70	40/70, 30/50, 20/40,	100, 40/70, 30/50
Maximum proppant concentration (ppga)	3.5	2	4	4
Average concentration (ppga)	0.6	0.6	1.2	1.2

Fractures may receive no proppant, may be propped open with low concentrations of proppant, or may have regions of high proppant concentration in the lower parts of the fractures because of proppant settling and dune formation (Warpinski 2009). For planar, less complex fractures or where main fractures provide the primary flow route, proppants

tend to accumulate at the bottom of the fracture until an equilibrium height is reached via fluidization and sedimentation; sets of pillars, pinchpoints and void spaces are created in more complex fractures, and allow proppants to become lodged at these irregularities, providing increased fracture conductivity (Palisch et al. 2010).

Non-uniform proppant partial monolayer, which could presumably maintain adequate conductivity in the fracture, is another mechanism of conductivity creation with low proppant loadings. The concept of "partial monolayer" is based on the belief that a partial layer of proppants can achieve significant conductivity due to the open space between sparsely distributed grains (Darin et al. 1959). Lab tests show that the conductivity of partial monolayer with ultra-light weight proppants can be an order of magnitude higher than similarly sized sand at 1 lb/ft^2 (Brannon et al. 2004). Nevertheless, there are concerns on how to achieve monolayer and on the effect of embedment, non-Darcy flow and proppant strength in partial monolayer placement (Palisch et al. 2010).

1.2.2 Fracture Conductivity Measurement Procedure

Laboratory measurement is a direct, controllable, and repeatable approach to study fracture conductivity. Generically, there are two types of laboratory procedures for the measurement, namely, the standard ISO conductivity test and the modified ISO conductivity test. The ISO 13503-5:2006(E) was developed to establish standard procedures and experimental conditions to evaluate conductivity of proppants under laboratory conditions. All test apparatus and conditions under ISO 13503-5:2006(E) are specified to guarantee the proppant evaluation results are comparable. In a word, the standard ISO procedures and apparatus are designed for the purpose of proppant material

studies and the measured conductivity is the baseline value without considering more realistic conditions.

The modified ISO test, or non-ISO standard test, on the other hand, has been made by various research parties for different applications. Among these, the commonest modification is to use a modified API conductivity cell to accommodate 3 times thicker samples to account for fluid leakoff through the sample during the experiment. Instead of flowing 2% KCl through the fracture as specified by ISO standards, the modified tests can flow dry gas, wet gas, fresh water, brine of various concentrations and multi-phase flow for different reasons, such as protecting the shale sample by flowing dry nitrogen (Zhang et al. 2013a), keeping the gel hydrated by wet gas (Awoleke et al. 2012), studying the water sensitivity (Conway et al. 2011), and investigating the effect of multiphase flow and non-Darcy flow (Barree et al. 2009). Both cylindrical core plugs and samples of API dimensions (7 inch long, 1.5 inch wide with curved ends) are used in the non-ISO tests (Ramurthy et al. 2011). Moreover, proppants are placed on smooth saw-cut Berea sandstone samples in ISO tests while any type of rock with either saw-cut smooth faces or rough faces can be used in the non-ISO tests.

1.2.3 Realistic Fracture Conductivity

Extensive studies on propped fracture conductivity under realistic conditions have been done during the past half a century. Darin and Huitt (1959) believed that a partial monolayer of proppant material can obtain high flow capacity and they theoretically derived an equation to calculate fracture conductivity based on the assumption that spherical proppant grains embed into the formation uniformly. Cooke (1973) studied the

effect of high-temperature brine, non-Darcy flow and elevated closure stress on fracture conductivity and determined that these factors can bring down fracture conductivities. The conductivity cell that Cooke used in his study is the prototype of the current API conductivity cell. Cooke (1975) carried on his research to investigate the effect of fracturing fluid. He found that the residue from guar polymer is the most important material in the fracturing fluids that can cause conductivity damage and factors such as proppant concentration, residue of the fracturing fluid, porosity of the proppant determine the conductivity reduction. Following these early works, more studies were done to further understand the damage mechanism by elevated stress, temperature, fracturing fluid filter cake and fluid additives (Reed 1980; Parker et al. 1987).

Systematic research on long term fracture conductivity, the impact of fracturing fluid leak-off, gel damage, non-Darcy flow, multiphase flow, proppant crushing and embedment has been done by Stim-Lab (Now a Core-Lab company) Proppant Consortium. Firstly, they measure the baseline fracture conductivity following ISO standard procedures; then, they derive correlations between fracture conductivity and the damage mechanisms based on the experiment results; eventually, the baseline fracture conductivity is modified by a number of coefficients representing each of the damage mechanisms to generate the realistic fracture conductivity.

Fredd et al. (2001) fractured the East Texas Cotton Valley tight sandstone samples and preserved the fracture surface roughness. They measured the fracture conductivity using natural sands and high strength manmade proppants. They found that the fracture surface displacement can provide significant unpropped conductivity.

Studies on the grain-scale failure processes in sands under elevated stress greatly aided the understanding of sand pack conductivity. It is found that the micro-scale physical processes of sand grains under closure stress include inter-granular slip, grain rearrangement, pore collapse, micro-fracture and grain crushing (Menendez 1995; Chester et al. 2004). Karner et al. (2005) pointed out that porosity evolution is predictable prior to macroscopic grain failure because it is only a function of applied mean stress.

In recent years, dynamic fracture conductivity tests have been successfully run to mimic realistic proppant placement (Marpaung et al. 2008; Awoleke et al. 2012). In dynamic proppant placement, slurry (mixture of proppant and gel) is pumped by a multi-stage centrifugal pump and flows through a created fracture of fixed width in the conductivity cell. After the pump is shut down, the fracturing fluid trapped in the fracture leaks off through the rocks leaving the proppants inside the fracture.

1.2.4 Fracture Conductivity Calculation

One of the earliest fracture conductivity calculation equations was derived by Darin et al. (1959) from the Kozeny-Carman relation based on the partial monolayer assumption. In this equation, fracture width is an input calculated by geometric relations between proppant grain diameter and embedment depth (Huitt et al. 1958).

The most widely used fracture conductivity calculation toolbox is a Stim-Lab product called Predict-K. This program contains the correlations found by the Stim-Lab consortium between fracture conductivity and proppant embedment, proppant crushing, gel filter cake and non-Darcy flow. These relations are established mainly by statistical method such as regression of extensive experimental datasets.

Gao et al. (2012) derived a mathematical model to calculate the proppant embedment depth and fracture conductivity based on the Hertzian elastic contact theory. They matched the predicted results with experimental results by introducing a number of empirical coefficients. A new fracture conductivity correlation was proposed by Awoleke (2013) using factorial design. This correlation links facture conductivity with proppant concentration, temperature, closure stress and gel loading.

Unpropped fracture conductivity calculation has been well studied in acid fracturing where fracture conductivity is created by unevenly etched fracture faces. Conductivity correlations for unpropped rough fractures were derived by Nierode and Kruk (1973), Gong et al. (1999), Mou et al. (2011) and Deng et al. (2012).

1.2.5 Shale-Water Interaction

The sensitivity of shale to water has been studied in the areas of drilling engineering and formation damage. Common authigenic clay minerals present in petroleum reservoirs are kaolinite, chlorite, illite, smectite and mixed-layer (Civan 2007). Clay particles are very small. The maximum dimension of a typical clay particle is less than 5 micron (Hughes 1951).

The movement of water/ions into and out of shale happens in many ways, including convection, osmosis, capillary imbibition and diffusion. Differential pressure between the hydraulic fracture and the matrix can cause water movement. However, convective flow into matrix is limited due to the ultra-low shale matrix permeability and relatively low differential pressure during a fracturing job. When micro-fractures are induced around the embedded proppant in brittle shale rocks (Kassis and Sondergeld

2010), water tends to flow through the fractures under differential pressure. Osmosis is considered as an important mechanism of ion migration because shale acts as a semi-permeable membrane (Low and Anderson 1958). The osmotic efficiency of clay depends on its porosity, salinity, cation exchange capacity, and confining pressure (Fritz and Marine 1983; Mody and Hale 1993). Capillary pressure is the pressure difference across the interface between two immiscible fluids. It is a function of interfacial tension, contact angle and the effective radius. Chenevert and Sharma (1993) believed that the driving force of water movement can be best described by the concept of total aqueous potential differences between shale water and injected water. They also found that the time-dependent shale swelling process is usually followed by a steady state process.

Shale-water interaction in the reservoir leads to reduced effective stress, Young's modulus, uniaxial compressive strength and eventually causes rock failure (Chenevert and Sharma 1993; Chen and Ewy 2002; Lin et al. 2013). When water migrates into clay structure in the above mechanisms, the local pore pressure is increased. The excessive pore pressure is hard to dissipate due to the ultra-low permeability of the shale matrix (Zhang 2005). Therefore, the effective stress of the shale matrix where the water front has reached is reduced. This localized pore pressure increment due to water movement is called "undrained condition" (Detournay and Cheng 1988). Migrated water in the clay lattice causes clay expansion and reduces the interlayer bonding strength of clay (Zhang 2005). The combination of elevated local pore pressure and reduced strength leads to the softening of shale after being soaked in water.

Formation damage caused by clay swelling, dispersion and migration in sandstone reservoirs were identified during water flooding early in the 1960s (Jones 1964). Clay

related porosity and permeability impairment usually happens in two ways: clay swelling and fines migration. Smectite is the most swellable clay mineral. According to Ezzat (1990), smectite is 100% expandable and it causes tremendous loss of micro-porosity and permeability. However, smectite is not as common as the other clay minerals in most of the reservoirs currently being developed (Conway et al. 2011). Mixed layer clay minerals are also believed to have some swelling ability due to the illite-smectite and chlorite-smectite layers. Clay swelling mechanisms, modeling, porosity and permeability reduction were reviewed by Civan (2007).

The other mechanism of formation damage due to water-clay interaction is fines migration. In sandstone, when the fluid velocity exceeds a critical value, fines would be released from the pores (Gruesbeck et al. 1982). Sharma et al. (1985) derived a model to estimate the rates of fine release and deposition in a single pore. Reservoir permeability is severely impaired due to the release, migration and entrapment of fines at the pore throats. Sharma et al. (1986) also investigated fines entrapment using a statistical approach and general population balance equations. Experimentally, fines migration is observed by a standard water shock experiment where the flow through a sandstone core is suddenly switched from brine to fresh water. It was reported that in the water shock experiment, permeability can be reduced by two orders of magnitude (Khilar and Fogler 1983).

In recent years, conductivity damage due to clay-water interaction has been brought into attention due to hydraulic fracturing in shale. During pre-fracturing formation evaluation in shale, unpropped fracture conductivity test (UFCT) is usually done to determine residual fracture conductivity in the shale rock and different fluid

sensitivity. In this test, a horizontal fracture along the shale rock bedding plane is induced in a 1 inch core plug. KCl and NaCl at various concentrations as well as fresh water are flowed through the fracture (Ramurthy et al. 2011). This experiment is also run to determine the differential pressure needed to allow the liquid to flow in the fracture.

1.3 Shale Fracture Conductivity and Production Performance

The importance of shale fracture conductivity tends to be neglected considering the nano-to-micro Darcy matrix permeability. **Fig. 1.1** shows the relationship between the equivalent skin factor and the dimensionless fracture conductivity. Clearly, there is minimum improvement on well productivity if the dimensionless fracture conductivity exceeds the value of 10. Assuming the matrix permeability of a shale formation is 0.0001 md, and the created fracture conductivity is 5 md-ft, for a 1000 ft fracture, the dimensionless fracture conductivity is,

$$C_{fD} = \frac{k_f w_f}{k_m x_f} = \frac{5}{0.0001 \times 1000} = 50 \quad \text{..... (1-1)}$$

However, the fact cannot be neglected that the relationship illustrated in Fig. 1.1 was derived from the fractured vertical well with a strong assumption that a bi-wing planer fracture is created. It was recognized that hydraulic fracturing in shale creates interconnected fracture networks. **Fig. 1.2** shows the microseismic mapping of a Barnett Shale well where each color represents the microseismic events from one stage and each dot represents a microseismic event in that stage.

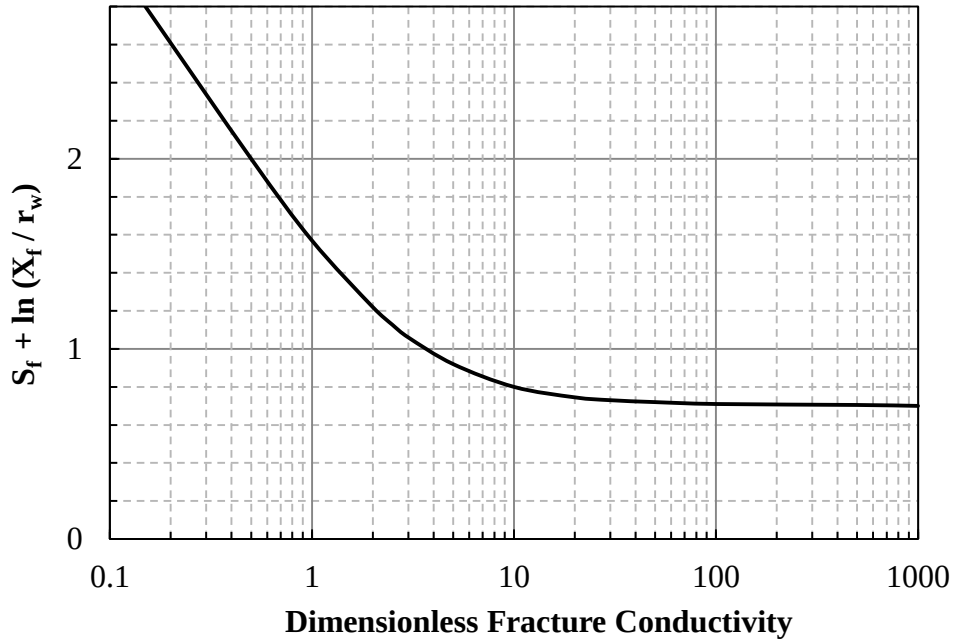

Fig. 1.1–Equivalent fracture skin factor (Cinco-Ley and Samaniego 1981).

Different from the conventional fractured wells, commercial hydrocarbon production from shale reservoirs depends on the large scale artificially created fracture networks with sufficient conductivity. Fracture network structures in shale formation are so extensive that the overall fracture network conductivity plays a critical role in the long term well performance.

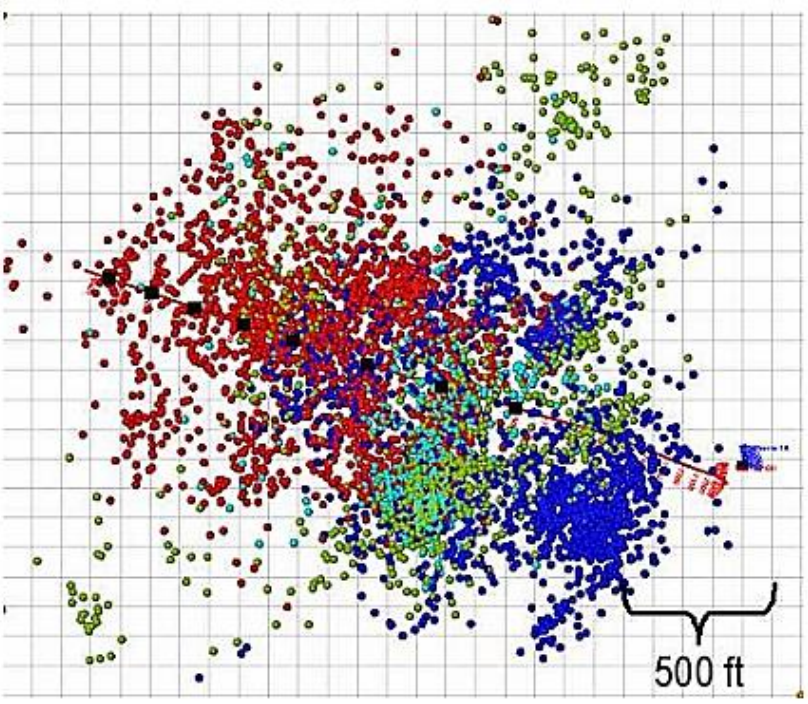

Fig. 1.2–Top view of the microseismic events of a fractured horizontal well in the Barnett Shale (Daniels et al. 2007).

Reservoir simulation studies by Mayerhofer et al. (2006) show that the overall fracture conductivity impacts well production significantly. As shown in **Fig. 1.3**, with the same created network volume, increase of fracture conductivity from 0.5 md-ft to 5 md-ft results in 4 times more production during 5 years of production. Another 40% increment of cumulative production can be achieved by increasing the conductivity to 20 md-ft.

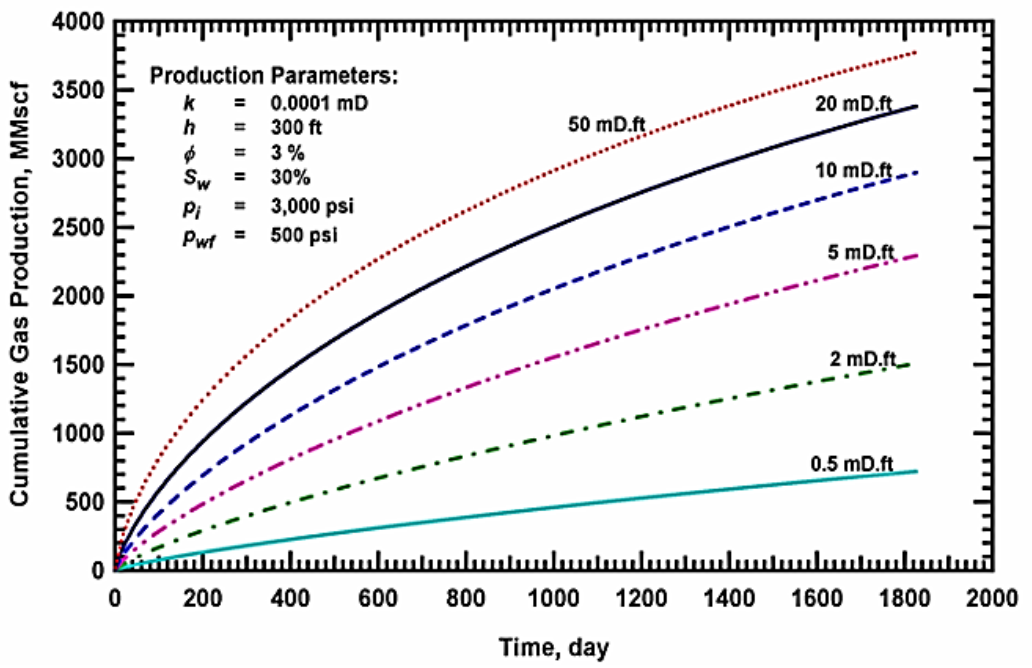

Fig. 1.3–Cumulative gas production affected by the overall network conductivity (Mayerhofer et al. 2006).

1.4 Problem Description, Objectives and Significance

Current conductivity measurement procedures were designed either for benchmarking different types of proppants, or for measuring fracture conductivity under high proppant concentration that is not common for most shale fractures. The widely used conductivity correlations were either generated from extensive tests on sandstones at high proppant concentrations or they were derived under over simplified assumptions. It is still unclear whether these correlations are as valid in shale as they are in sandstone formations. The public literature shows there are very little studies on the conductivity impairment by water using the real rough shale fractures. The water damage mechanisms are yet to be reported with sound laboratory evidence. Therefore, improved laboratory measurement

framework, more accurate conductivity values for various types of fractures, and understanding of the shale fracture conductivity damage mechanisms, are needed.

It is under these motivations that we propose to investigate hydraulic fracture conductivity in shale formations. It will accomplish the following objectives:

(1) To develop new laboratory procedures with good experimental error control for shale fracture conductivity measurement.

(2) To measure conductivity of different types of fractures, such as unpropped and propped natural fractures, and unpropped and propped induced fractures using various proppant sizes and concentrations.

(3) To develop a program that generates fracture conductivity considering factors including proppant grain rearrangement, proppant crushing, embedment, size and concentration.

(4) To investigate the conductivity damage mechanisms due to water and identify the dominant damage mechanism by studying the individual factors.

This study elevates the understanding of hydraulic fracturing in shale. Conductivity measurement of the natural fractures and the unpropped fractures provide insights into the source of production in the nano-to-micro Darcy permeability rocks. Investigations on the creation of propped fracture conductivity help the proppant selection and the design of proppant concentration. Identification of the conductivity damage mechanism provides a potential opportunity for the operator to optimize the fracturing design. Reservoir engineers benefit from this study in that the conductivity values at different locations of the fracture networks and their time dependence can be found in the context to better match the well production history and to estimate the recoverable hydrocarbons.

1.5 Approach

1.5.1 Experimental Approach

Extensive experiments were run to measure the undamaged shale fracture conductivity and to study the shale fracture conductivity damage by water. Procedures for the experimental approach are shown below:

(1) Screen fracturing design variables to be studied, and examine the factors that impact fracture conductivity in shale; review current industry practices to determine reasonable ranges for the parameters; scale these parameters into laboratory conditions.

(2) Collect representative shale rock samples and characterize the rocks.

(3) Design laboratory procedures to induce fractures and prepare the samples to fit into the conductivity cell; acquire experimental materials and consumables.

(4) Perform preliminary tests on the first batch of rock samples to examine the integrity of the apparatus and the modified procedures; review the findings with the advisory committee.

(5) Run experiments extensively to study each of the proposed variables.

(6) Collect evidence that support the findings using microscopic imaging techniques.

The flowchart in **Fig. 1.4** describes the experimental workflow.

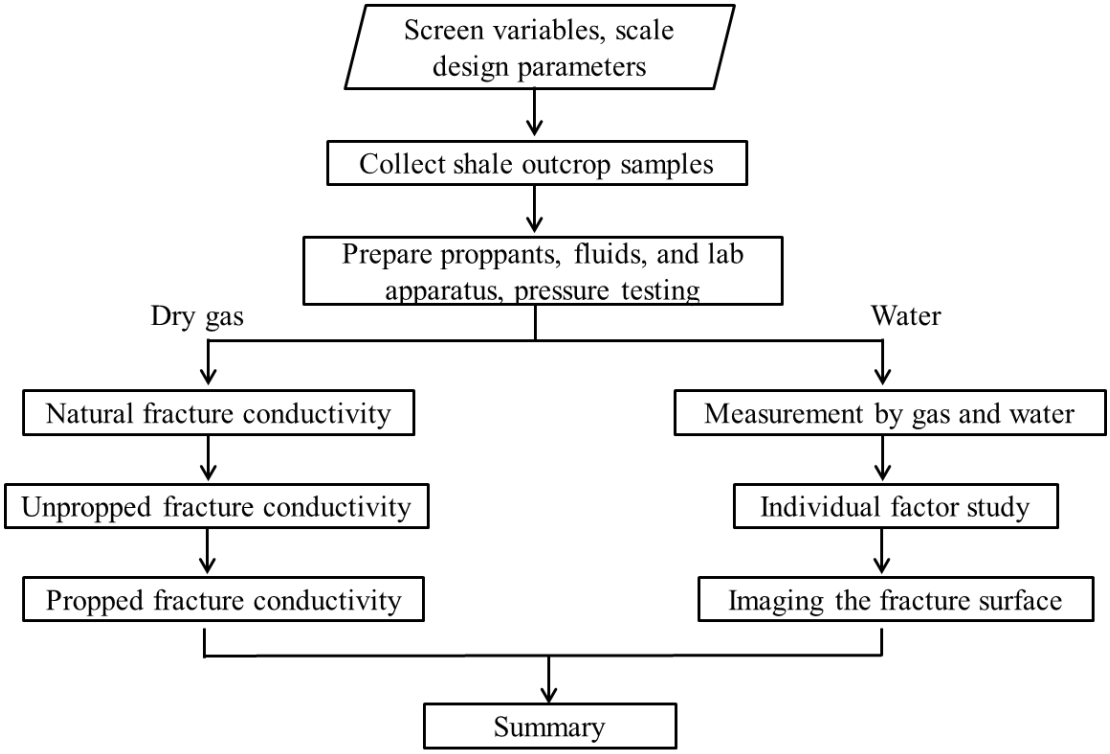

Fig. 1.4–Workflow for the experimental approach.

1.5.2 Theoretical Approach

Fracture conductivity is calculated through the following steps:

(1) Review the recognized correlations for sand pack permeability calculation.

(2) Derive and solve the population balance equation for size reduction that describes proppant crushing in the fracture during elevated stress application.

(3) Validate the solution of the population balance equation by comparing the calculated results with the sieve analysis data.

(4) Measure the initial proppant pack width under zero closure stress and calculate the width change due to grain rearrangement and embedment.

(5) Calculate the fracture conductivity and compare the results with the measured fracture conductivity.

(6) Modify the correlation that is based on the dry gas measurements to consider water damage.

A flowchart describing the conductivity calculation procedure is shown in **Fig. 1.5**.

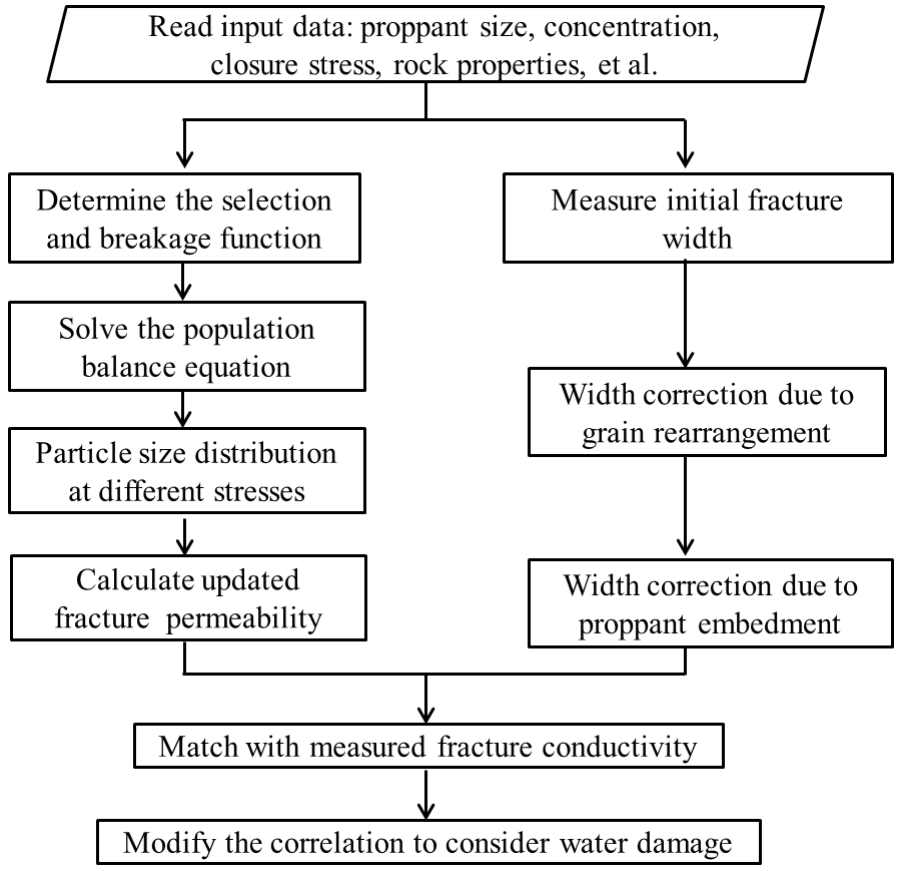

Fig. 1.5–Workflow for the theoretical approach.

1.6 Dissertation Outline

In this dissertation, Chapter I gives the general background of this research by reviewing the literature; then objectives of this research are proposed. The importance of fracture conductivity on long term well production in shale reservoirs is also discussed.

Chapter II introduces the experimental design, laboratory setup, material preparation and general operational procedures. More importantly, this chapter includes the actions we take to control the experimental errors.

Chapter III focuses on the unpropped fracture conductivity in shale reservoirs. It first discusses the unpropped fracture closure by presenting the stress-strain relationship for different shale rocks. Unpropped fracture conductivities of the Barnett Shale, the Fayetteville Shale and the Eagle Ford Shale are presented followed by the relationship between unpropped fracture conductivity and the rock brittleness. Unpropped natural fracture conductivities are also investigated.

Chapter IV presents the measurement and theoretical calculation of propped fracture conductivity. This chapter also discusses the excessive crushing of partial monolayer sands on rough fracture surfaces and the findings are supported by sand grain shear experiments. This chapter highlights the application of population balance equation to predict proppant size distribution over stress to calculate the fracture conductivity.

Chapter V examines the effect of water on shale fracture conductivity. General experimental observations are presented first; then individual factors that might damage the fracture conductivity are studied. Finally, a new correlation to calculate shale fracture conductivity that considers the water damage effect is proposed.

Chapter VI summarizes the work and makes recommendations for future work.

2 EXPERIMENTAL DESIGN AND METHODOLOGY

This chapter presents the experimental design, laboratory setup, material preparation, and the procedural challenges. More importantly, this chapter highlights the key experimental design considerations and the actions we take to control the experimental errors.

2.1 Introduction

The efforts to measure hydraulic fracture conductivity started in the late 1950s, shortly after the birth of this revolutionary technology. The fundamental goal of conductivity measurements is to optimize the proppant usage for well productivity improvement and cost reduction.

After several decades of improvements on laboratory setups and experimental conditions, conductivity measurements are either to (1) benchmark proppant testing as commercial products, or to (2) acquire realistic conductivity values that reservoir simulator can use to match historical data and to predict well performance. Reproducibility and stability are the critical design considerations. To obtain realistic fracture conductivity, laboratory conditions should be as close to reservoir conditions as possible. The conditions include reservoir stress status, temperature, reservoir fluids and compositions, proppant size and concentration, fracturing fluids and additives, production operations such as well shutdown and flowback. In this sense, realistic conductivity measurement is usually reservoir specific. There are more challenges in realistic conductivity measurements to get reproducible results.

The following sections present the experimental preparation, apparatus, and the error controls to generate repeatable results.

2.2 Shale Samples, Fluids and Proppants

The Barnett Shale, the Fayetteville Shale and the Eagle Ford Shale are used for the unpropped fracture conductivity investigation. Only the Barnett Shale is used for the propped fracture conductivity test and the water damage study. The following section will discuss the properties of these shale rocks.

2.2.1 Shale Rock Samples

Locations and properties of the Barnett Shale, the Eagle Ford Shale and the Fayetteville Shale are introduced below:

(1) The Barnett Shale

The Barnett Shale formation was deposited throughout the Fort Worth Basin and tends to thin towards the Llano Uplift in the south with thickness ranging between 30 ft and 50 ft where the outcropped samples were collected (Papazis 2005). Barnett Shale outcrops sampled from a quarry were used for the experiments (**Fig. 2.1**). The shale samples collected for this research are greyish black to black.

The Barnett Shale is generally clay-rich (**Table 2.1**). Depending on the location, carbonate can comprise up to 40%. The clay minerals are mainly illite and mixed layered clay. In some areas, it contains up to 50% mixed layered clay. Other minerals in the Barnett Shale include feldspar and pyrite.

According to X-ray Diffraction tests, the outcropped samples we collected for this study contain 31% quartz, 32% illite, 9% mixed layered illite-smectite, and 5% kaolinite (**Fig. 2.2**). Another major mineral in the Barnett Shale outcrop is anhydrite, which is the main natural fracture infill material.

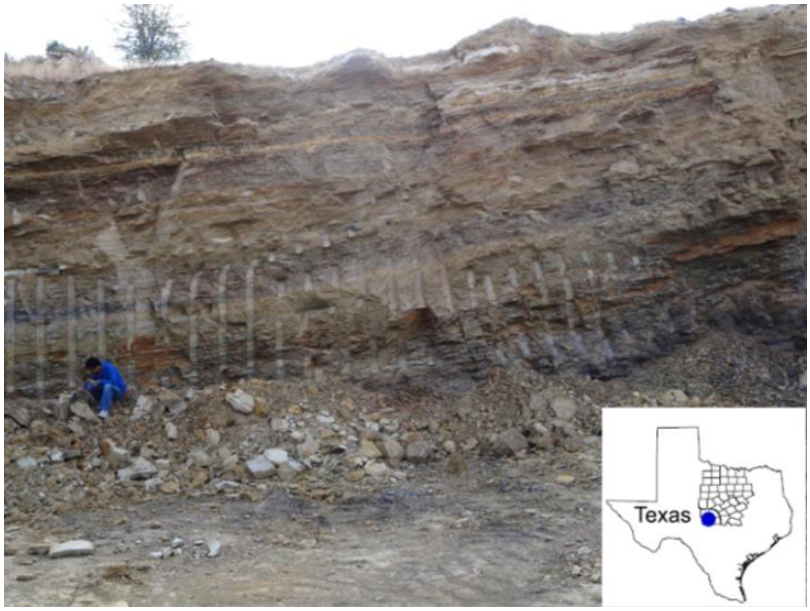

Fig. 2.1–The Barnett Shale outcrop.

Table 2.1–Mineralogy of the Barnett Shale (Shelley et al. 2008).

Quartz	25-65%
Feldspar	2-10%
Calcite	2-30%
Dolomite	2-10%
Kaolinite	0-2%
Illite	0-35%
Smectite	0
Mixed layered clay	5-50%
Chlorite	0-2%
Pyrite	2-10%
Siderite	1-15%

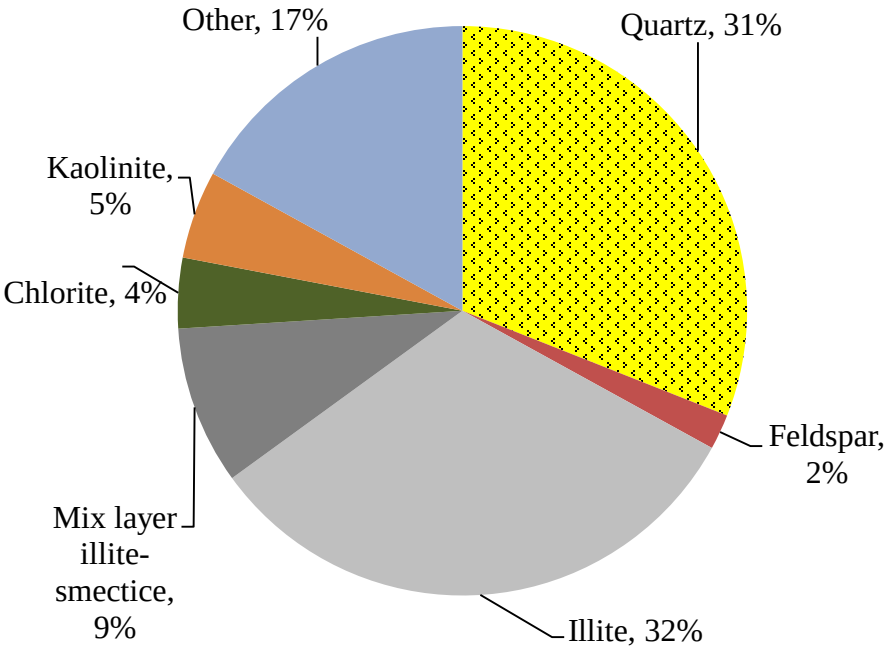

Fig. 2.2–Mineralogy of the collected Barnett Shale outcrop samples.

The Barnett Shale outcrops in the quarry were exposed for such a long time that the surface rocks are too friable to cut into dimensions fit for the modified API conductivity cell. To collect fresh representative shale samples, a frontend loader excavated deep into the outcrop to acquire large shale blocks with preserved natural fractures. The blocks were covered with polyethylene wrap and bubble wrap to prevent damage during transportation or from humidity (**Fig. 2.3**).

Fig. 2.3–The preserved Barnett Shale outcrop samples.

(2) The Eagle Ford Shale

The Eagle Ford Shale is an organic rich fossiliferous marine shale. It was deposited in the Late Cretaceous age and underlies much of the South Texas. The Eagle Ford Shale samples for this study were collected from roadcuts along U.S. Highway 90, about 30 miles northwest of Del Rio, TX. The outcrop exposes 20-30 ft of organic-rich marl and limestone of the middle Eagle Ford formation (**Fig. 2.4**).

It is a misconception to name it as a type of "shale" because the dominant mineral in the Eagle Ford formation is calcite. X-ray Diffraction data show that the outcropped samples we collected contain 62% calcite and 24% quartz. The clay mineral comprises only 8% (**Fig. 2.5**). Technically, the Eagle Ford Shale is an organic-rich mudstone or anecdotally named as "dirty limestone". The Eagle Ford Shale has strong heterogeneity

in lithology. As shown in **Fig. 2.6**, the dark grey to black organic rich mudstone can transit to the light grey calcite layers in an inch-scale sample.

Fig. 2.4–The Eagle Ford Shale outcrop.

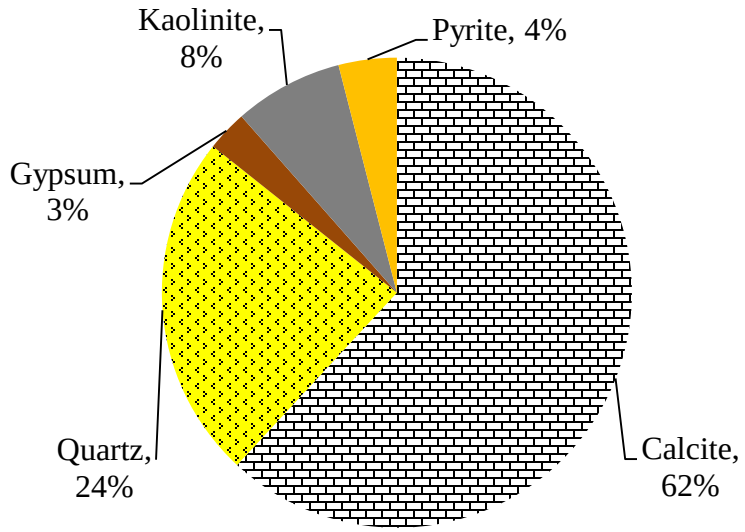

Fig. 2.5–Mineralogy of the collected Eagle Ford Shale outcrop samples.

Fig. 2.6–The broken face of the Eagle Ford Shale outcrop sample (ConocoPhillips, Eagle Ford Field Excursion manual, 2011).

(3) The Fayetteville Shale

The Fayetteville Shale extends across northern Arkansas. It is the geologic equivalent of the Mississippian Barnett Shale. The Lower Fayetteville in the Fayetteville Shale reservoir is divided into three zones, among which the FL2 is the ideal target interval. FL2 has the lowest clay content and the highest gas porosity (Harpel et al. 2012).

In our study, samples from the two zones FL2 and FL3 of the Lower Fayetteville were collected from the Killebrew outcrops in Arkansas by Southwestern Energy (**Fig. 2.7**). The Fayetteville Shale contains high percentage of illite and mixed layered illite-smectite. X-ray Diffraction test data from published literature are shown in **Fig. 2.8** where illite and mixed layer clay minerals account for about 50% of the total mineral content (Deville et al. 2011).

Fig. 2.7–The Fayetteville Shale outcrop (Image provided by Southwestern Energy).

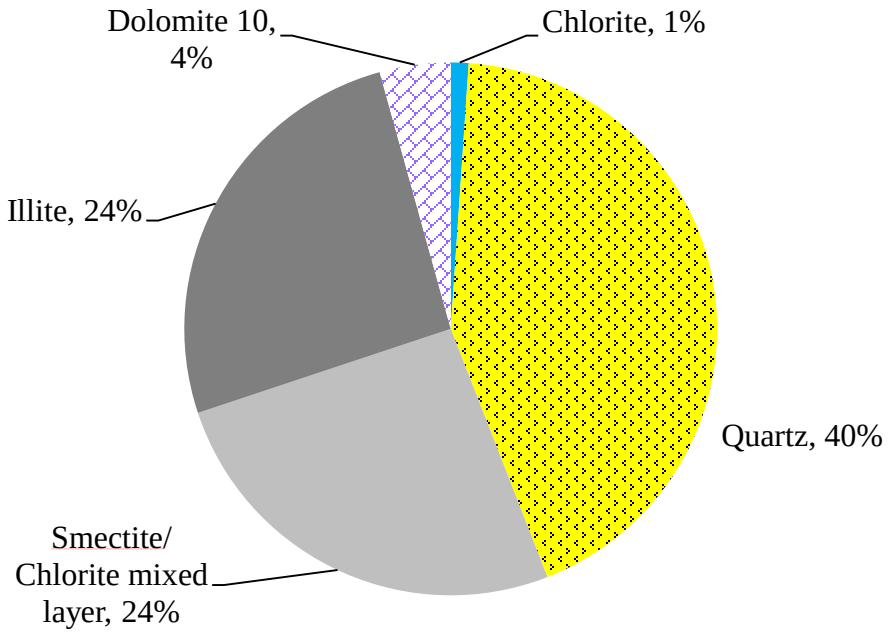

Fig. 2.8–Mineralogy of the Fayetteville Shale (Deville et al. 2011).

2.2.2 Shale Fracture Creation

The samples were cut into dimensions fit for the modified API conductivity cell. Due to thickness limitation of the outcrop, sandstones were cut to make the 1-1.5 inch thick shale samples up to 3 inches required by the conductivity cell (**Fig. 2.9**).

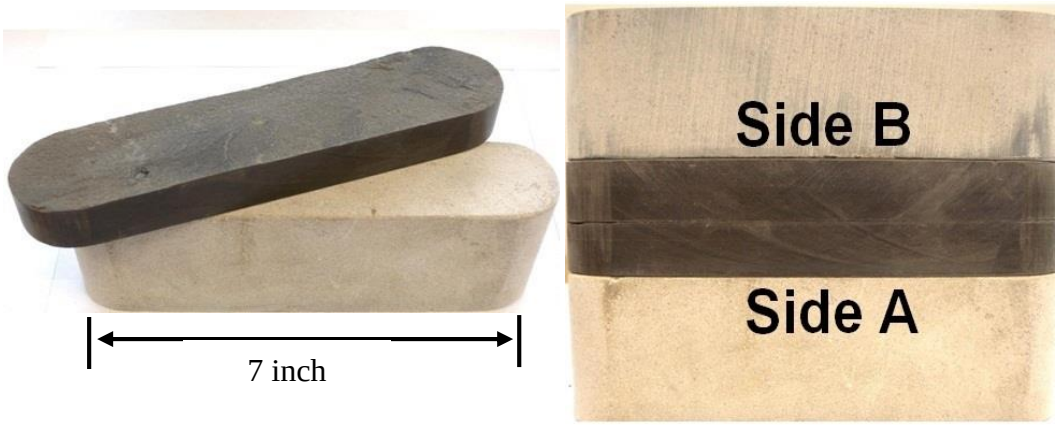

Fig. 2.9–Barnett Shale samples shaped to fit into the conductivity cell.

The easiest way to induce an artificial fracture in shale is to open the highly laminated bedding plane. In field fracturing, vertical fractures are more likely to be created cutting across the bedding planes. Nevertheless, the fracture surfaces along the bedding planes are representative in conductivity creation, because the shale fracture conductivity is dictated by properties that are not directional, such as fracture surface hardness to resist embedment, mineralogy or clay content to interact with water, and proppant size, concentration and distribution.

To open natural fractures is tricky because the infill can be loosely attached to the fracture faces. It is critical to keep the vibrations to a minimum when cutting samples and not to tilt the samples during transportation.

2.2.3 Fluids and Proppants

Industrial grade dry nitrogen is used for the gas-measured conductivity. The liquids include fresh water, 2% KCl, and brine with a similar chemical composition as typical flowback water. A typical flowback water sample in the Barnett Shale has total dissolved solids (TDS) of 39,000 mg/L (Horner 2011). In our study, we formulated the brine with the total dissolved solids of 38,000 mg/L (**Table 2.2**). In the following context, the referred "flowback water" in the conductivity measurement has the chemical compositions shown in Table 2.2.

Table 2.2–Chemical compositions of the reconstituted water sample (Horner 2011).

Ions	Barnett (mg/L)	Lab (mg/L)
Na^{+}	12453	12646
Mg^{2+}	253	
Ca^{2+}	2242	2244
Sr^{2+}	357	
Ba^{2+}	42	0.0807
Mn^{2+}	44	0.0066
Fe^{2+}	33	
SO_4^{2-}	60	
HCO_3^{-}	289	9
Cl^{-}	23797.5	23170
TDS	39,570	38,060

Proppant concentrations in this study are 0.03, 0.06, 0.10 and 0.15 lb/ft^2, equivalent to 0.25-1.25 ppga in slick water fracturing assuming a 0.20 inch wide fracture at the end of pumping without proppant settling and before the fracture closure. The

minimum proppant concentration on the surface area to obtain a full monolayer is calculated by the following equation (Brannon et al. 2004).

$$C_a = 5.20(1-\phi)\gamma_p d_p \quad \text{(2-1)}$$

Where C_a is the minimum areal concentration required to obtain a full monolayer in lbm/ft²; ϕ is the minimum obtainable porosity of proppant pack in fraction; γ_p is the proppant specific gravity in g/cm^3; and d_p is the average proppant diameter in inch. For 100 mesh sand, assuming a porosity of 0.4 and an average diameter of 0.0059 inch, with a specific gravity of 2.65, the minimum surface concentration for a full monolayer is 0.05 lb/ft^2. However, proppant partial monolayer is hard to obtain due to the surface topography, even at a concentration of 0.03 lb/ft^2. The rough surface of the sample causes sand grains to have a tendency to roll from the surface peaks and to collect in the valleys. At the peaks a proppant partial monolayer may form but in the valleys multiple sand layers exist, as illustrated by **Fig. 2.10**.

A top view of typical proppant distribution before an experiment can be seen in **Fig. 2.11**. Under the same areal concentration in lb/ft², the larger the proppant size is, the less the amount of proppant grains are. The peaks of the fracture surface are not covered by the 100 mesh sands. For 40/70 mesh and 30/50 mesh sands, more areas of the bare fracture faces are exposed. In order to prevent the nitrogen flow from carrying proppants out of the sample, conductivity measurements start from 500 psi closure stress to stabilize the proppants. After each experiment, the outlet cap of the conductivity cell is taken out to check for proppant migration.

Proppants used in this research are 100 mesh sand, 40/70 mesh Badger sand and 30/50 mesh Badger sand supplied by ConocoPhillips. Proppants are randomly sampled

from a 5-gallon bucket. To get a reasonable range of fracture conductivity, experiments are repeated with different shale samples.

The proppants were manufactured in compliance with ISO 13503-2. Some quality parameters of the proppants are shown in **Table 2.3**. Sieve analysis was done to understand the particle size distribution (**Fig. 2.12**).

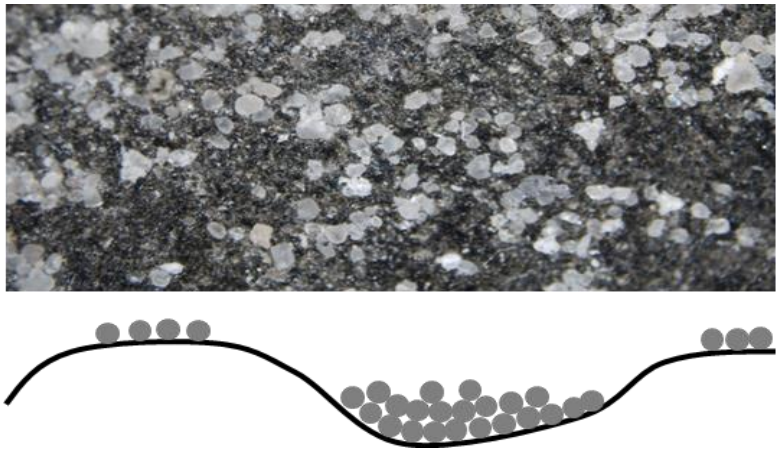

Fig. 2.10–Proppant distribution on the rough shale fracture surface.

Fig. 2.11–Placement of 100 mesh sands on rough fracture surface at 0.03 lb/ft^2.

Table 2.3–Quality parameters of the proppants.

Mesh size	Nephelometric Turbidity Units (NTU)	Roundness	Sphericity
40/70	53	0.75	0.75
30/50	43	0.75	0.75

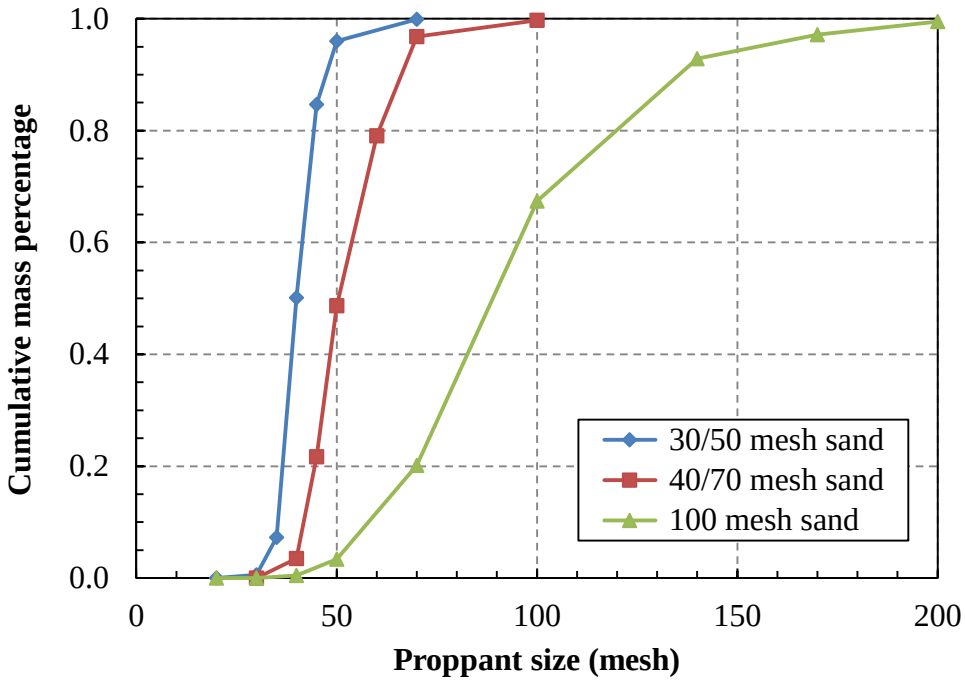

Fig. 2.12–Sand particle size distribution.

2.3 Methodology for Conductivity Measurement by Gas

2.3.1 Experimental Apparatus for the Dry Gas Measurement

Most of the experimental apparatus has been introduced by previous studies (Awoleke 2013; Kamenov 2013). The following section will focus on the operating conditions of the pre-existing devices and functions of the newly added devices.

The main components of the experimental apparatus include:

(1) Hydraulic load frame

(2) Gas flow controller

(3) Modified API conductivity cell

(4) Back pressure valve

(5) Pressure sensors

The hydraulic load frame can apply 208,000 lbf at the rate of 1,215 lbf/minute (stress rate 100 psi/minute). The position sensor of the load frame has an accuracy of 4×10^{-4} inch. The gas flow controller has a full range of 0.35 ft^3/minute with an accuracy of 3.5×10^{-5} ft^3/minute. All other aspects of the modified conductivity cell are designed as per the API conductivity cell except the dimensions. Differential pressure sensor diaphragms can be switched and the pressure ratings for this study are 0.32 psi, 2.5 psi, 5 psi and 20 psi. Flow line diameter is 0.25 inch. Awoleke (2013) reported the detailed procedures of pressure sensor calibration in his dissertation. The schematic of the setup for gas measurement is shown in **Fig. 2.13**. Pictures of the hydraulic load frame and the conductivity cell can be found in the thesis of Kamenov (2013).

The newly added device for the conductivity measurement by water is the Totalizer Input/Output Controller package (TIO). TIO can record the total gas volume that flowed through the fracture and output digital flow rates into the configuration and monitoring utility software. The continuous gas flow rates are used to calculate the conductivity when gas displaces water out of the fracture. Operational procedures for using TIO are in **Appendix A**.

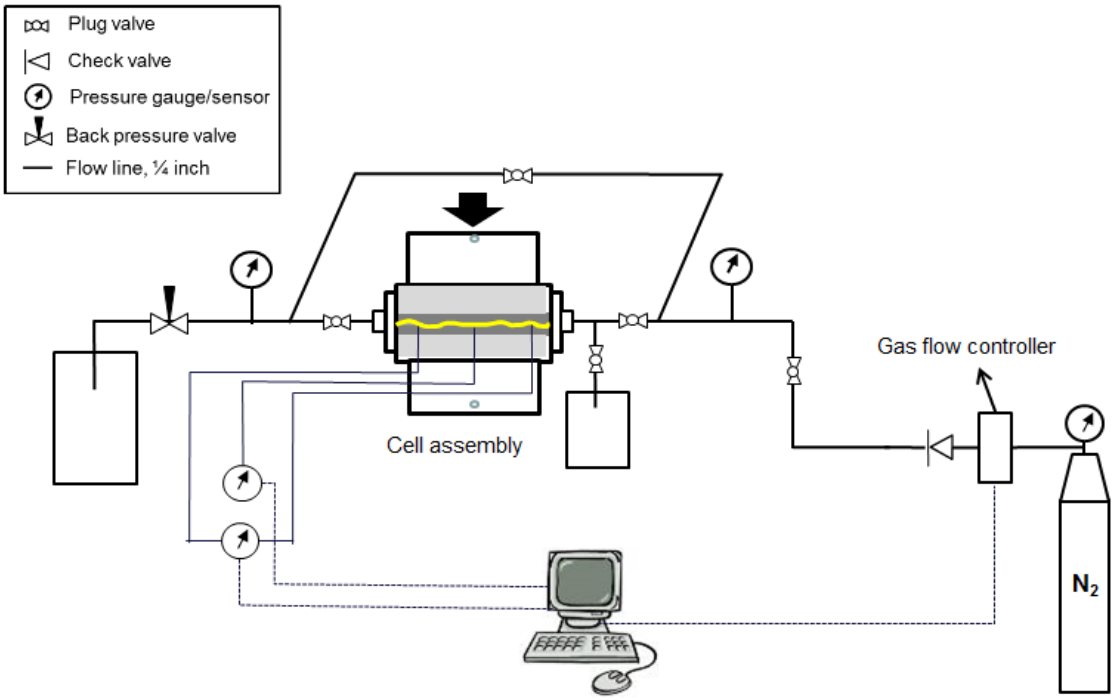

Fig. 2.13–Schematic of the experimental setup for conductivity measurement by gas.

2.3.2 Experimental Design Permutations and General Procedures

Experimental design is shown in **Fig. 2.14**. Unpropped fracture conductivity is measured with natural fractures, aligned and displaced induced fractures. Propped fractures utilize 100 mesh, 40/70 mesh, and 30/50 mesh sands at concentrations from 0.03 lb/ft ²to 0.15 lb/ft ². Experiments are run at room temperature.

Experiments under the same conditions are repeated with different samples due to the stochastic nature of proppant sampling and fracture surface asperities. The uncertainties of proppant sampling and proppant placement will be discussed later.

General procedures for the experiment include inducing fractures in shale, coating samples by silicone rubber, proppant placement, loading samples into the conductivity

cell, and flowing gas to measure conductivity. Detailed procedures have been reported by Kamenov (2013) and will not be repeated here.

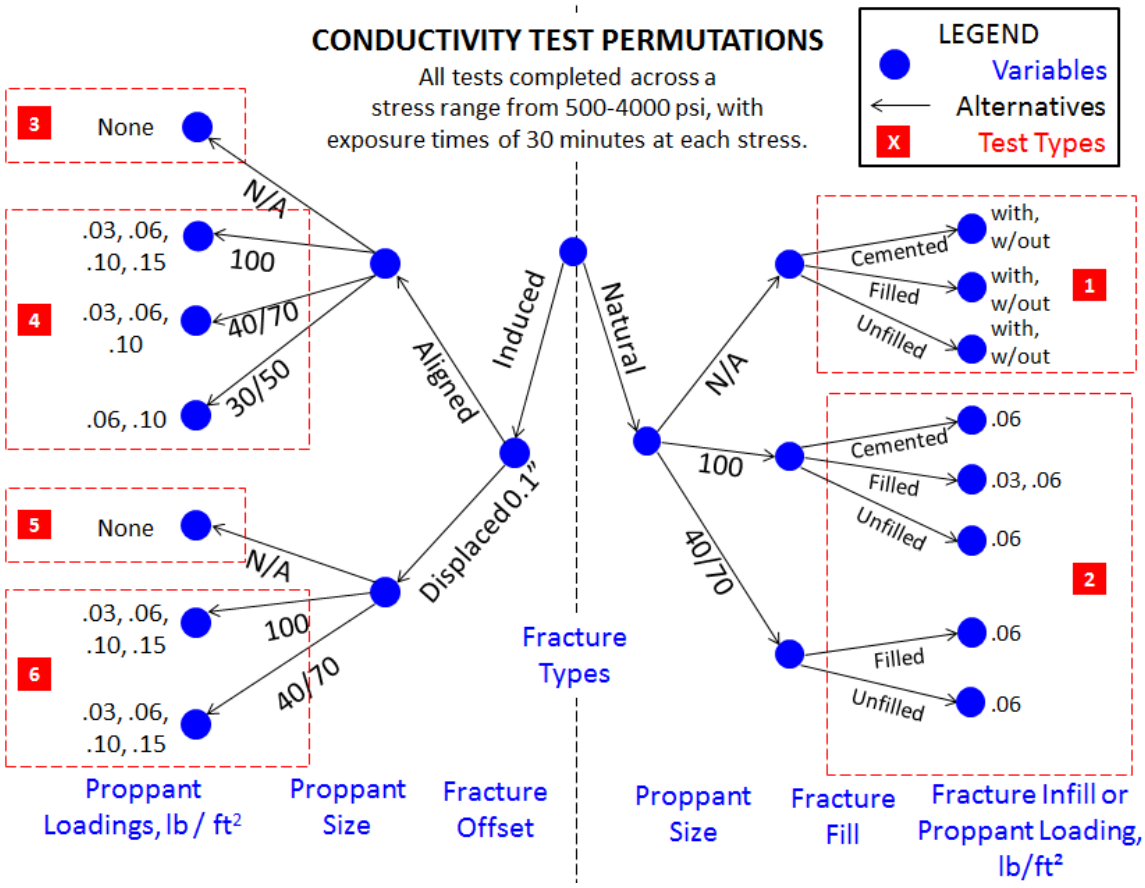

Fig. 2.14–Experimental design permutations for conductivity measurement by gas.

2.4 Methodology for Conductivity Measurement by Water

A new experiment was proposed to study shale fracture conductivity damage by water through sequentially flowing nitrogen, water, and nitrogen. The first nitrogen flow measures the undamaged fracture conductivity since nitrogen does not react with clay; water or brine is then flowed following the nitrogen until steady state is reached; finally, nitrogen is flowed again to remove the water from the fracture and to measure the

recovered fracture conductivity. The difference in undamaged and recovered fracture conductivity is used to evaluate the severity of water damage. Detailed experimental procedures are provided in this section.

2.4.1 Experimental Apparatus for the Water Measurement

The entire apparatus consists of five separate units:

(1) Gas injection unit

(2) Liquid injection unit

(3) Conductivity cell assembly

(4) Closure stress application unit

(5) Pressure sensors and data acquisition unit

Fig. 2.15 shows the schematic of the apparatus for water experiment. The photograph of the setup is shown in **Fig. 2.16**.

The gas injection unit simply consists of a nitrogen tank containing industrial grade dry nitrogen and a pressure regulator. The liquid injection unit includes a 1000D Teledyne ISCO Syringe pump, a PVC refilling accumulator, two stainless steel displacement accumulators, an AW-32 hydraulic oil reservoir and the flow line manifolds.

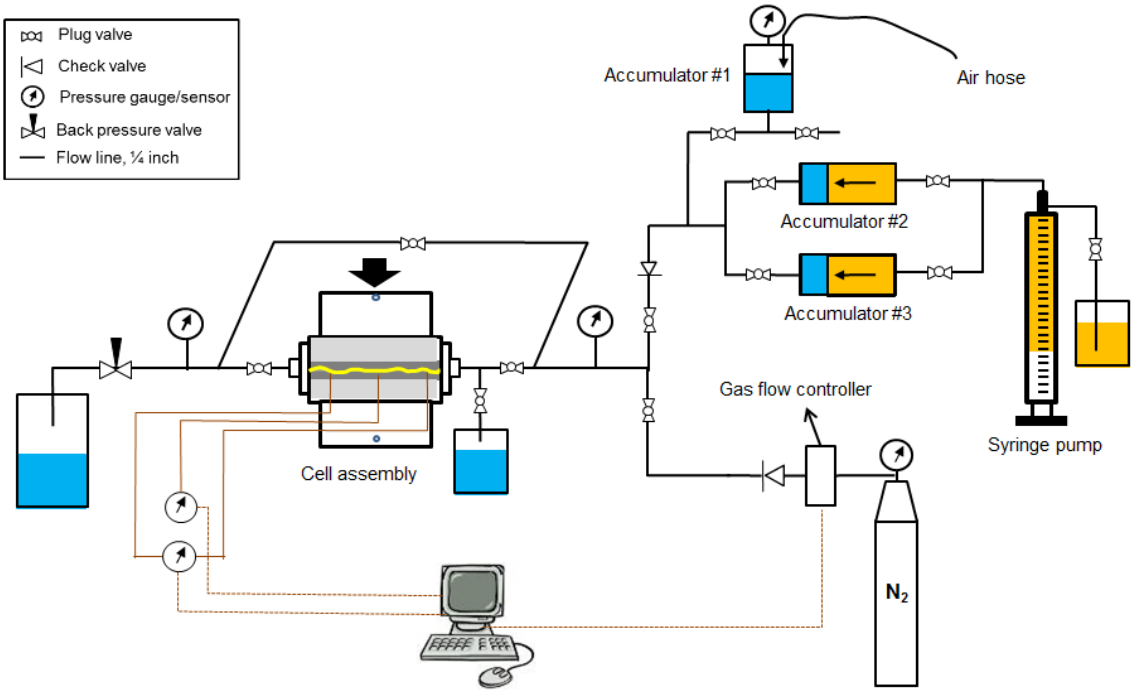

Fig. 2.15–Schematic of the setup to evaluate the conductivity damage by water.

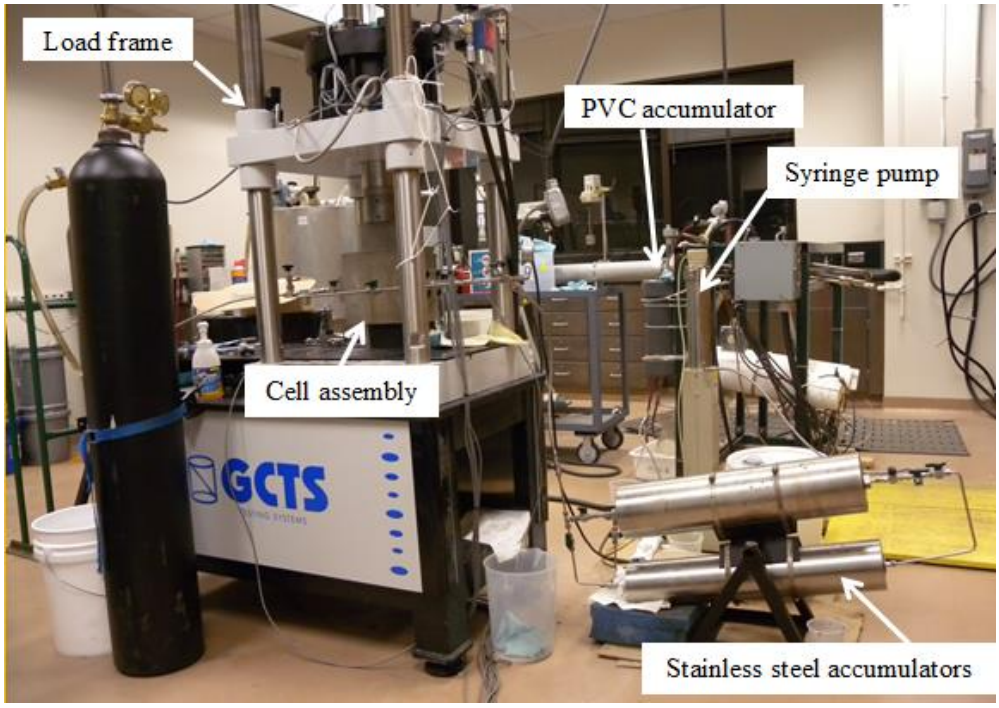

Fig. 2.16–Photograph of the setup to evaluate the conductivity damage by water.

The 1000D Teledyne syringe pump has one liter nominal capacity. The flow rate range for this pump is 0.1-408 mL/min. The working pressure is 0-2,000 psi. The parts in Fig. 2.15 highlighted by orange are only in contact with AW-32 hydraulic oil.

The capacity of the PVC accumulator is 2 liters and the pressure rating is 100 psi. The top of the accumulator has a 0.5 inch tubing fitting and can be connected to the air hose. The compressed gas pressure in the lab is 100 psi. So, a pressure regulator is installed on the rack to control the accumulator working pressure between 60-80 psi.

The stainless steel brine/fresh water accumulator has 4-liter capacity. During the experiment, we need to keep track of the brine or fresh water volume in the accumulator, because once the piston reaches the end of the accumulator, the pump will pressure up until it reaches its maximum working pressure. The flow line in the manifold is composed of 0.25 inch 316 stainless steel tubing and Swagelok tubing fitting. The air hose on the PVC accumulator is connected with the lab compressed air outlet by a quick connector. For future reference, the order number and specifications for all the parts are summarized in **Appendix B**.

2.4.2 Experimental Design

Fracture conductivity measured by liquid is influenced by rock type, fluid type, flow rate, proppant and experimental procedures. Variations of these conditions are made to study the effect of rock type, shale fines migration, proppant fines migration, rock creep, brine concentration, and residual water content. The experimental conditions are summarized in **Table 2.4**. By comparing with the results of control experiments, the effect of the individual factors can be investigated.

Table 2.4–Conditions to study the individual factors in water experiments.

Studied Factors	Experiment Conditions	Control Experiment Conditions
Rock type	Barnett Shale	Berea sandstone
Shale fines migration	Forward flow	Forward and reverse flow
Proppant fines migration	White sand	Half white sand and half green resin coated sand
Rock creep	Short term (0.5 hour)	Longer term (50 hours)
Brine concentration	2% KCl	Fresh water
Residual water	Dry gas under room temperature	Dry gas at 220 ℉ to fully remove water from the fracture face

Various authors have emphasized the importance of stabilized flow in conductivity measurement (Barree and Conway 2009; Conway et al. 2011). We controlled the rate to be in the laminar flow regime. The Reynolds number in the porous media is given by,

$$R_e = \frac{\rho v D_H}{\mu(1-\phi)} \quad \text{..... (2-2)}$$

Where the hydraulic diameter D_H for a slot is defined as,

$$D_H = \frac{2h_f w_f}{(h_f + w_f)} \quad \text{..... (2-3)}$$

The Reynolds number for the liquid flow in the experiments are calculated and reported in **Fig. 2.17**. In the water experiments, the maximum flow rate is 5 mL/min in propped fracture. Obviously, the laminar flow assumption is valid in this study.

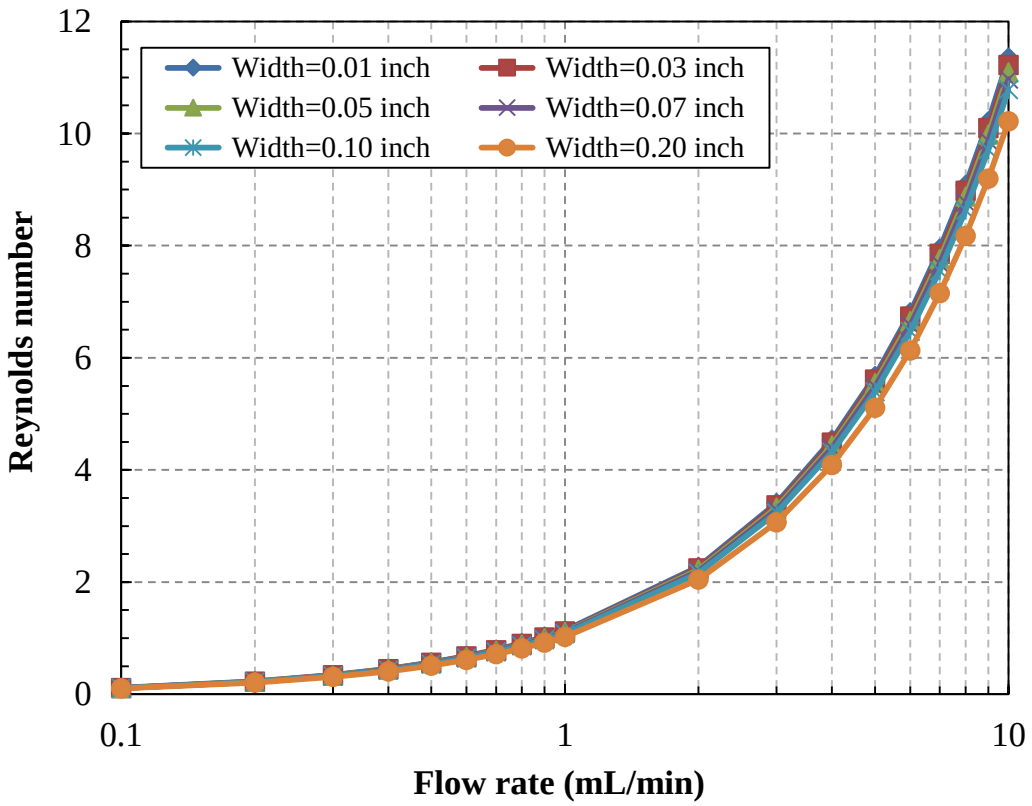

Fig. 2.17–Reynolds number for the liquid flow at various fracture widths.

2.4.3 Procedures for the First Nitrogen Flow

The undamaged fracture conductivity is measured by the first nitrogen flow. The procedures to prepare the sample and to load the sample into the conductivity cell are the same as the dry gas experiments. Since the undamaged conductivity is critical for the determination of liquid flow rate, the following steps need to be exercised with great caution:

(1) Create the execution file beforehand and ramp up the closure stress to the target value strictly at the rate of 5.4 kN/min or 100 psi/min. This is to make sure the gas measured conductivities are comparable for all the experiments because the laminated rock samples can be cracked longitudinally at high stress rates.

(2) Wait for the same amount of time before the measurement. Rock creeps under normal stress. In this study, we wait for 2 hours before flowing gas for each experiment. The waiting time is set to account for the missing time in the dry gas measurement from 500 psi to 3,000 psi, because the water experiment is run at 4,000 psi only.

2.4.4 Procedures for Brine and Fresh Water Flow

After the undamaged fracture conductivity measurement, liquid is flowed to simulate the damage process by exposing the fracture face to water. Step-by-step procedures are outlined below:

(1) Mix the flowback water as per the chemical compositions shown in Table 2.2 and record the brine volume.

(2) Disconnect the ½ inch tubing fitting on the top of the PVC accumulator and pour the brine in it. Keep track of the brine volume.

(3) Switch the plug valves on the manifold to recharge the stainless steel accumulators. Make sure the plug valve on the refill hose of the syringe pump is open. Put the outlet of refill hose in a beaker.

(4) Connect the compressed air hose to the PVC accumulator.

(5) Adjust the regulator to apply 60 psi to displace the brine out of the PVC accumulator.

(6) Monitor the syringe pump refill hose for hydraulic oil and record the effluent oil volume. This volume is equal to the brine volume injected into the stainless steel accumulator.

(7) Switch off the compressed air when 1,800 mL hydraulic oil is collected from the refill hose. The residual 200 mL brine plays the role of a safety factor to prevent the gas flowing into the accumulator.

(8) Repeat the procedure to refill the other accumulator with fresh water.

(9) Record the volume of brine and fresh water in the accumulators (3,600 mL for each is preferred) and switch the plug valves back to the pump position.

Note: Though the objective of this study is not to study the liquid compatibility, steady state flow is still reached before switching to the second gas flow.

(10) Calculate the expected differential pressure and select the right pressure sensor diaphragm. Pressure sensor calibration after changing the diaphragm has been reported by Awoleke (2013).

(11) Refill the pump barrel with hydraulic oil from the AW-32 oil reservoir. The full capacity for the 1000D series syringe pump is 1015 mL.

(12) Connect all the flowlines.

Note: Strictly follow the instruction by Swagelok on how to install tubing fittings. Never wrap tubing fittings with Teflon tape, which completely destroys the threads of tubing fittings.

(13) Switch the plug valves as shown in **Fig. 2.18** to divert the flow through the bypass lines to displace the air out of the system and to check the flow path.

(14) Close the back pressure valve to pressure up the system to 50 psi; stop the pump; hold for 15 minutes; check all the connections for leakage. Flow rate is 5 mL/min during this step. In the case of leakage, bleed off the pressure, and reconnect the broken fittings.

(15) Open the back pressure valve; direct flow to the fracture when continuous liquid flow is observed in the outlet.

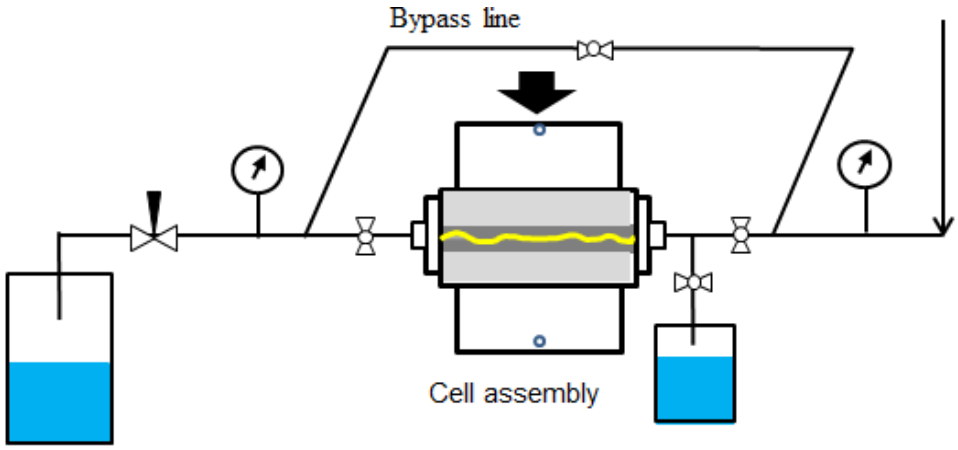

Fig. 2.18–Flow through the bypass line.

(16) Decrease flow rate to prevent the pressure surge-up. Depending on the initial fracture conductivity, the starting liquid flow rates are recommended in **Table 2.5**.

Table 2.5–Recommended starting liquid flow rate.

Initial Conductivity (md-ft)	Starting liquid flow rate (mL/min)
0.1-10	0.1
10-50	0.2
50-100	0.5
100-500	1

(17) Adjust the flow rate according to the pressure response. It is recommended to step up the flow rate. The increment of flow rate should not elevate the differential pressure up to 80% of the pressure rating of the sensor diaphragm.

(18) Record the cell differential pressure, cell pressure, pump rate, pump pressure and pump volume every 5 minutes before the liquid breaks through the proppant pack.

(19) Keep monitoring the pressure response until steady state flow is reached.

Note: To reach steady state flow, it might take several hours as a function of the initial conductivity.

2.4.5 Procedures for the Second Nitrogen Flow

The second nitrogen flow is designed to measure the recovered fracture conductivity after the water flow. This is realized by the following procedures:

(1) Stop the pump and bleed off the pressure; secure accumulators; cut off the connection between the accumulator and the cell assembly.

(2) Plug in the TIO into the computer and open the program to record gas flow rates.

(3) Connect the lines in the same way as the first nitrogen flow; close the back pressure valve.

(4) Switch the ball valves to divert the gas flow through the bypass lines.

(5) Open the nitrogen tank regulator until the upstream pressure gauge reads 50 psi.

(6) Slowly open the back pressure valve to drain the liquid in the bypass lines and the shared flow lines by liquid and gas.

(7) Adjust the back pressure valve and the nitrogen tank regulator to get gas flow rate of 0.5 L/min and upstream pressure gauge reading of 50 psi.

(8) Switch the plug valves to direct the gas flow into the fracture when the bypass lines are fully drained with no liquid flowing out.

(9) Monitor the gas flow rate, upstream gauge pressure, cell pressure, differential pressure, and the effluent flow. Record all the values every 3 minutes.

(10) Open the nitrogen tank regulator to increase the upstream gauge pressure to 70 psi, if there is no effluent flow after 30 minutes and the cell pressure stays at zero with the upstream gauge reading 50 psi.

(11) Record the pressure and rate data; wait for 30 minutes for the effluent flow.

(12) Once continuous gas flow is established, keep flowing gas until gas flow rate, cell pressure and differential pressure are stabilized.

(13) Verify the measurement by stepping up the flow rate and record the differential pressure response.

(14) When finishing the measurement, shut off the nitrogen tank first and then bleed off the pressure through the tank regulator.

(15) Gradually open the backpressure valve to bleed off the pressure in the cell assembly.

(16) Disconnect the flow lines, pressure sensors, TIO; dismantle the flow inserts from the conductivity cell with closure stress acting on the assembly.

(17) Use the hand pump to push the sample out.

Note: This is a two-man operation. One handles the hand pump while the other holds the samples. Otherwise, the samples will drop on the table and the proppants will be disturbed.

(18) Shut down the pump and the data acquisition controller.

2.5 Key Design Considerations and Procedural Challenges

Main components of the setup were developed for gel damage studies in tight gas and the general procedures were included in various literatures (Marpaung et al. 2008; Awoleke 2013). Kamenov (2013) summarizes the modifications to the operational procedures for shale fracture conductivity study in his thesis. The steps will not be repeated in this dissertation but the key procedural challenges and solutions that are not covered by Kamenov (2013) are reported below.

2.5.1 Before Experiment

This section discusses the design considerations and procedural challenges before experiments:

(1) Inducing fracture in shale samples

In standard API conductivity tests, the saw-cut sandstone samples have smooth fracture faces. To make the experiments more realistic, fracture surface roughness is taken into account in this study.

Fredd et al. (2001) split the tight sandstone samples using masonry rock splitter blades (**Fig. 2.19**). Recently, cylindrical core samples of 1 inch or 1.5 inch diameter have been used with fracture surfaces either saw cut or by Brazilian test (Morales et al. 2011; Ramurthy et al. 2011). Core samples like these are put in Hassler sleeve core holder to flow different fluids through the unpropped fracture (**Fig. 2.20**).

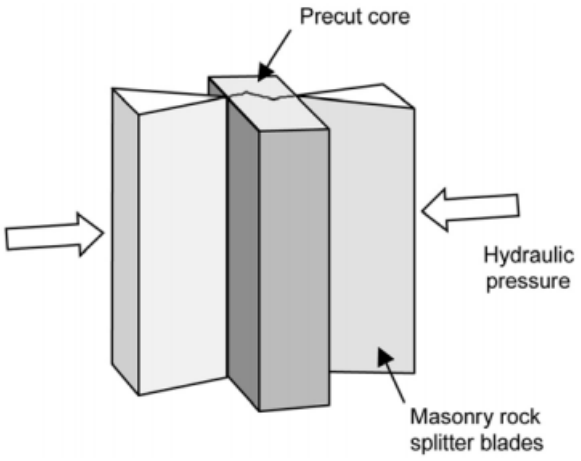

Fig. 2.19–Splitting the tight sandstone sample by Fredd et al. (2001).

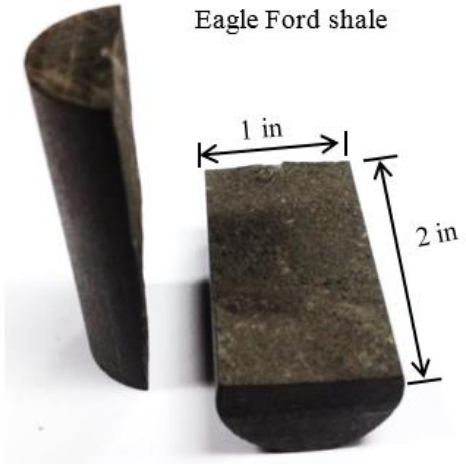

Fig. 2.20–Induced fracture in the shale core plug.

In this study, we break the shale samples along the laminations. Bedding planes in shale are the surfaces that are perpendicular to the direction of sediment settling. So, bedding planes are horizontal during deposition. We recognize that unless the shale bedding layers thrust up to a high dip angle, the bedding planes are not usually the fracture faces as in the horizontal fractures. However, in the outcrop and roadcuts where

our samples were collected, we observed the pre-existing fractures can be vertical, horizontal or slanted in certain degrees. This means the weak planes can be of any angle. As stated in the previous section, the properties that dominate fracture conductivity in shale are not directional. Therefore, results generated on fracture faces by opening the laminations are representative.

Another consideration of opening weak bedding planes is to have better experiment reproducibility. The modified API conductivity cell requires good fracture alignment to expose the fracture to the pressure sensor ports. Otherwise, differential pressure measurements could be erroneous. This is illustrated in **Fig. 2.21**. We attempted to induce fracture perpendicular to the bedding planes. But the fracture deviates towards the horizontal direction along the bedding planes after growing for less than 1 inch. To ensure the measurements are repeatable, we have been using the bedding planes as our fracture faces.

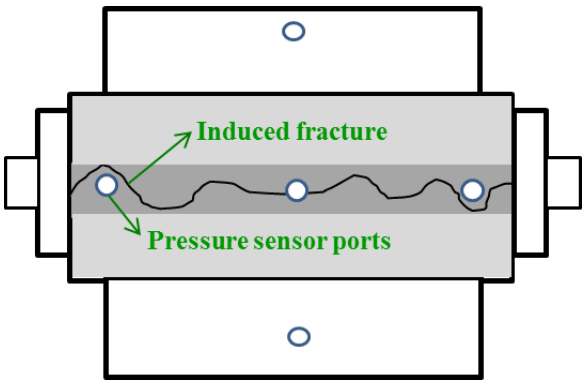

Fig. 2.21–Induced fracture bypassing the pressure measurement ports.

(2) Sample coating mold slot width vs. cell slot width

A mold was built to coat the shale sample with silicone rubber. The mold has

similar dimensions as the conductivity cell except that the slot width is 0.003 inch larger than the width of conductivity cell slot width (**Fig. 2.22**). The extra 0.003 inch silicone rubber is squeezed into the conductivity cell and can provide good seal between the rock and the cell walls. The mold is wire-cut to prevent the vibration by a drill bit. The height of the mold is 3.5 inch.

(3) Cure the silicone rubber compound under optimal time and temperature

To seal the gap between the rock sample and the inner wall of the conductivity cell, shale samples are coated with a silicone rubber layer in the mold. In this study, Momentive RTV 627 silicone rubber compound is utilized. Momentive SS4155P primer is applied to the shale surface to increase the adhesion of the silicone rubber to the rock. In more permeable rocks, the liquid silicone rubber filtrates into the rock face and firmly attaches there; however, shale matrix is so tight that the silicone rubber peels off after the RTV 627 cures.

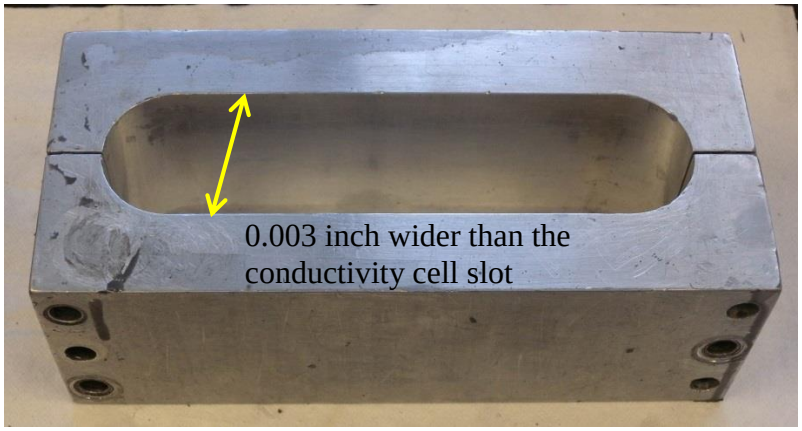

Fig. 2.22–Silicone rubber compound coating mold.

Another challenge is the dehydration of SS4155P on shale because the water

species in the primer solution diffuses into shale matrix leaving the white power solute on the shale face. Here are a couple of solutions to this problem. First, fill in the liquid silicone rubber compound into the mold while the shale face is still wet; second, replace SS4155P with SS4004P primer. SS4004P primer elevates the adhesion to impermeable surface such as metals. But the potential problem is the rubber stain on the aluminum mold if the silicone release spray is not applied evenly and correctly.

Another key step that is often neglected is the baking time of the silicone rubber mixture in oven. RTV627 silicone rubber cure time and temperature relationship is plotted in **Fig. 2.23**.

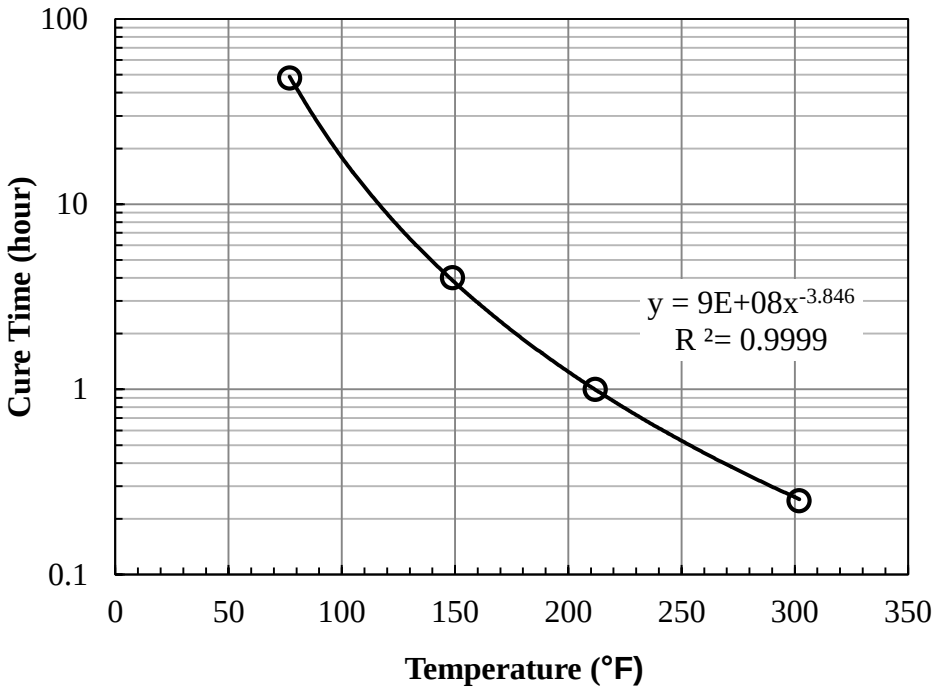

Fig. 2.23–Temperature and cure time relationship for RTV627 compound system.

A common mistake in coating the sample is to overheat the silicone rubber and shale sample asserting that the longer samples are kept in elevated temperature, the

stronger the rubber would be. In our practice, overheating the shale samples can cause some issues in practice: (1) micro-fissures in the shale samples are induced because of the heat stress; (2) silicone rubbers are more brittle and thus are more prone to be broken apart when pushing the sample out of the mold; (3) high temperature evaporates the bound water and might disturb the structural water in clay minerals. With these concerns, it is recommended to follow the cure time-temperature relationship. From our practice, we suggest to bake the sample at 150°F for 4 hours.

(4) Coating the shale sample with silicone rubber

A "4-step method" was developed to coat the fracture seamlessly. This method is illustrated by **Fig. 2.24**.

Step 1: Samples are aligned and both sides are labeled.

Step 2: Before pouring the liquid silicone compound into the mold, the fracture should be covered by paint tape so that the liquid epoxy cannot encroach into the rough fracture surface. Then, coat the bottom 1.5 inch of the sandstone sample. After the 1.5 inch section is cured, continue coating the middle 3 inch section.

Step 3: Coat the top 1.5 inch sandstone section. Take the sample out from the mold. This is called a blank sample because the rock sample is completely covered by the silicone rubber. Cut to expose the inlet and outlet, and the three ports to expose the fracture to the pressure measurements ports.

Step 4: Plastic bands (Teflon tape) are wrapped between the measurement ports to isolate the three pressure sensors. High vacuum grease is applied where the Teflon tapes are wrapped to reduce frictional pressure when pushing the samples into the cell. Grease should be applied at a reasonable distance from the fracture in case that it will be

squeezed into the fracture.

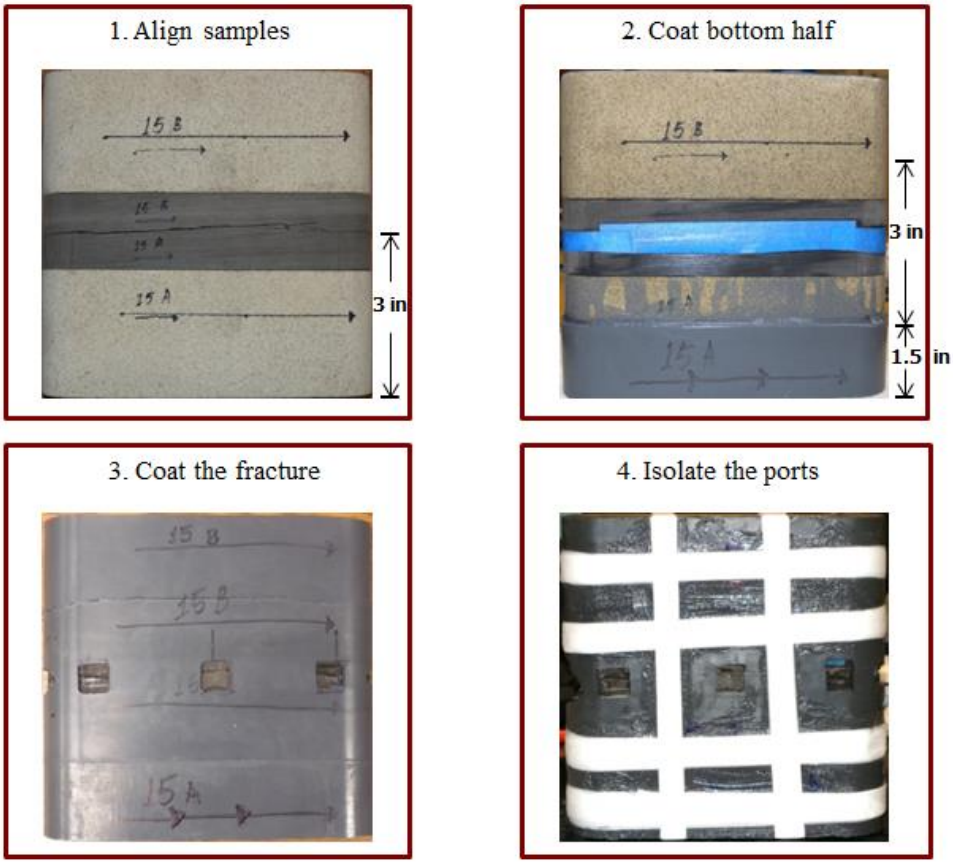

Fig. 2.24– "4-step method" to coat the sample with silicone rubber.

2.5.2 During Experiment

This section discusses the design considerations and procedural challenges during experiments:

(1) Pressure test the system integrity

Cell assembly integrity is tested to detect gas leakage both parallel and perpendicular to the flow direction. System integrity test procedures and pressure/rate response are discussed below.

As shown in **Fig. 2.25**, to detect the vertical flow leakage, close plug valve 2 and 3 and open valve 1. Give a flow impulse to the cell assembly and record the response of differential pressure sensor and absolute pressure sensor. Gas rate, cell pressure and differential pressure responses are plotted in **Fig. 2.26**.

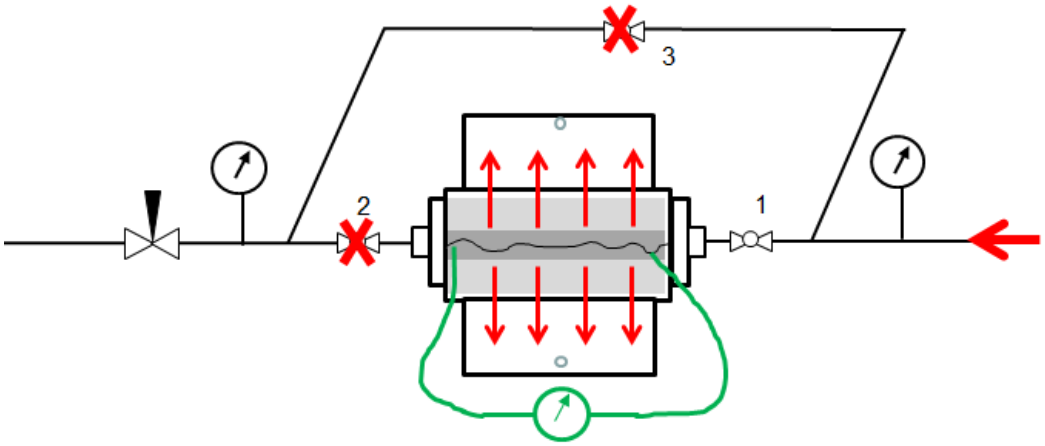

Fig. 2.25–Pressure test the system to detect the vertical gas leakage.

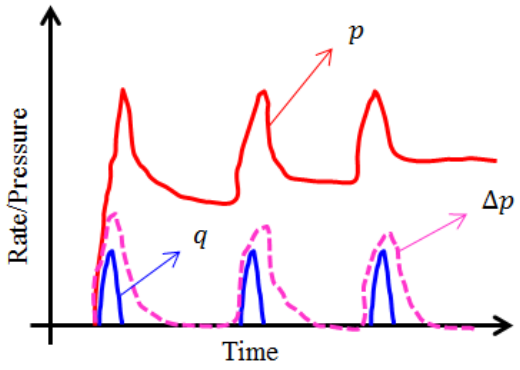

Fig. 2.26–Pressure and rate response to flow impulse to detect the vertical leakage.

The rate impulse is represented by the blue line; pressure responses should be observed instantaneously by the differential pressure (pink dashed line) and cell pressure

(red solid line) sensors. The cell pressure sensor is attached to the middle measurement port. The differential pressure should drop back to zero because there is no flow rate, while the cell pressure stays at a certain level. Repeating the rate impulse, similar pressure/rate signatures should be observed but the cell pressure now is higher than the previous impulse. Repeat this for a third rate impulse and stop. If the differential pressure line doesn't drop back to zero; instead, it stays at a certain value, then a vertical leakage occurs in the cell assembly.

The solutions are to (1) spray foam soap to check all the connections; (2) take out the sample to double check if it is the correct sample dimension to match with the cell; (3) re-apply the Teflon tapes and high vacuum grease, and (4) to ensure alignment of the sample stack with the cell when pushing it into the cell slot using the hand pump, since this might be caused by the crushed rubber at the curved edges.

To detect the horizontal flow leakage, close plug valve 3, open valve 1 and 2, then put a blank sample into the conductivity cell, as shown in **Fig. 2.27**. A blank sample is fully covered by the silicone rubber without cutting the measurement ports or inlet/outlet ports. Gas rate, cell pressure and differential pressure responses are plotted in **Fig. 2.28**.

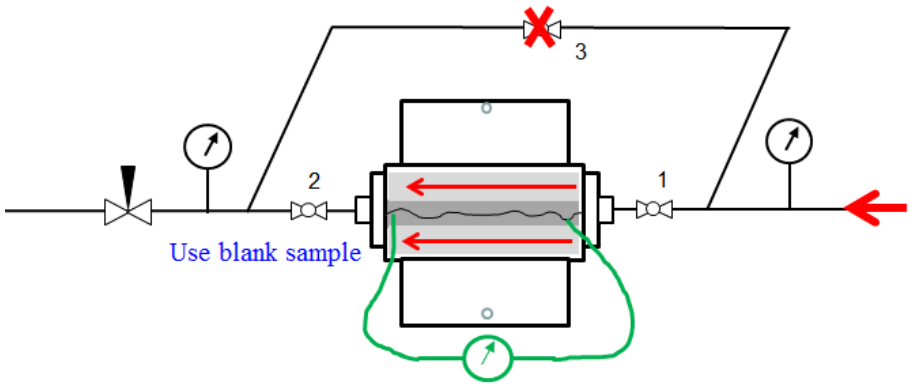

Fig. 2.27–Pressure test the system to detect the horizontal gas leakage.

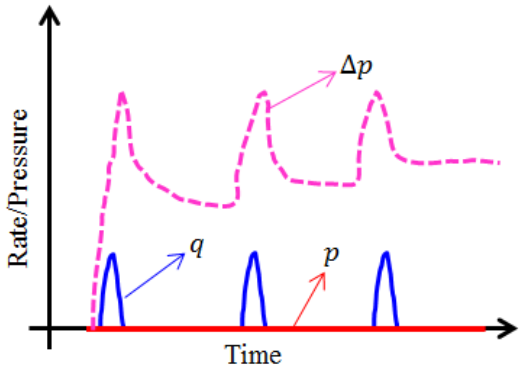

Fig. 2.28–Pressure and rate response to flow impulse to detect the horizontal leakage.

After the first flow impulse, an immediate rate and differential pressure responses should be seen as represented by the solid blue line and the dashed pink line. However, the cell pressure sensor should not sense any pressure response if there is no horizontal leakage flow bypassing the sample. Repeat the same rate impulse following the same procedure. If the cell pressure does not keep zero at any of the flow impulses, there is horizontal flow leakage between the blank sample and the cell walls. The measured conductivity would be higher than its real value. The solution to fix the horizontal leakage is to take out the sample to: (1) check the dimensions of the blank sample and make sure it matches with the cell; and (2) add more layers of Teflon tape to isolate the pressure sensors. If it still does not work, use the caliper to measure the cell opening widths at both ends. Past experience shows that the cell could be deformed if the load frame execution file is damaged or unreasonable operational procedures are applied.

(2) Flow rate and different pressure control

Awoleke (2013) has discussed the relationships between interstitial velocity, proppant pack porosity and the interstitial Reynolds number proposed by Huang and Ayoub (2008). He recommended using Darcy plot to better fit the experiment data for

low velocity experiments and Forchheimer plot for higher velocity experiments. We attempt to find the boundary between using Darcy plot and Forchheimer plot through varying the flow rate in experiments.

Fig. 2.29 shows the conductivity calculated by Darcy equation and Forchheimer equation using the same experiment data. The first data point at 200 psi closure stress is measured by flow rates at 1.5, 3.5, 5.5 and 7.5 L/min; the second data point at 500 psi closure stress is measured at rates 0.15, 0.35, 0.50, and 0.80 L/min. As we can see from the plot, when flow rate is less than 0.80 L/min, it is reasonable to use Darcy equation for gas to calculate fracture conductivity. This observation through the experimental work is consistent with the finding by Awoleke (2013) that at higher flow rates than 0.9 L/min, the Forchheimer equation should be used. To better fit the experimental data, we control the flow rate to be lower than 0.80 L/min where the Darcy equation is valid to use. This is operationally viable because we conduct experiments with small size proppants at low concentrations or with unpropped fractures. Flow rates lower than 0.80 L/min can induce measurable response in the pressure sensors.

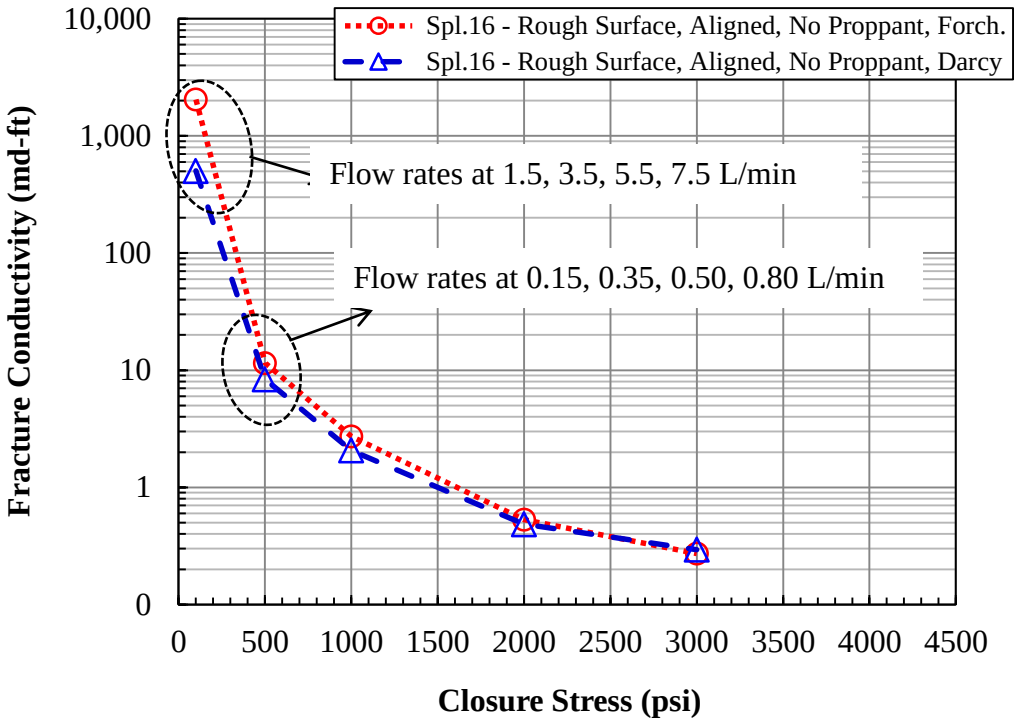

Fig. 2.29–Conductivity calculated by Darcy equation and Forchheimer equation using the same experiment data.

A constant volumetric flow rate is assumed in the conductivity calculation. To validate this assumption, the cell pressure (metered by the middle measurement port) is increased so that the differential pressure is less than 5% of the cell pressure.

2.6 Determination of Fracture Conductivity

Fracture conductivity is calculated using the Darcy equation (**Eq. 2-4**) and the Forchheimer equation (**Eq. 2-5**) for gas based on four measurements of volumetric gas flow rate, differential pressure, and cell pressure.

$$-\frac{dp}{dL}=\frac{\mu v}{k_f} \quad \text{..... (2-4)}$$

$$-\frac{dp}{dL}=\frac{\mu v}{k_f}+\beta\rho v^2 \quad \text{..... (2-5)}$$

Eq. 2-6 and **Eq. 2-7** are the general Darcy equation and Forchheimer equation for gas derived by Tek et al. (1962), and used by Marpaung et al. (2008), and Awoleke (2013).

$$\frac{M_g\left(p_1^2-p_2^2\right)}{2ZRTL}=\frac{\mu\rho q}{h_f}\frac{1}{w_f k_f} \quad \text{..... (2-6)}$$

$$\frac{M_g\left(p_1^2-p_2^2\right)h_f}{2ZRTL\mu\rho q}=\frac{\rho q}{h_f\mu}\frac{\beta}{w_f{}^2}+\frac{1}{w_f k_f} \quad \text{..... (2-7)}$$

Where M_g is the molar mass of gas in kg/mol; p_1 and p_2 are the upstream and downstream pressures in Pascal along the fracture; h_f is the sample width in meter; Z is the gas compressibility factor (dimensionless); R is the universal gas constant in J/mol K; T is the temperature in Kelvin; μ is the gas viscosity in Pa s; L is the length of fracture over pressure drop in meter; ρ is the density of gas in kg/m^3; q is the volumetric flow rate of gas in m^3/s; β is the inertial factor in 1/m; w_f is the fracture width in meter; and k_f is the fracture permeability in m^2.

Experiments for all the unpropped fractures and propped fractures with concentrations below 0.10 lb/ft^2 are run at flow rates smaller than 0.80 L/min. Eq. 2-6 can be used for these cases. For experiments where higher flow rates are needed to generate measurable pressure response, Eq. 2-7 is used for conductivity calculation.

In the current lab setup, a differential pressure sensor measures $(p_1 - p_2)$ as Δp, and an absolute pressure sensor measures the cell midpoint pressure as p_{cell}. By replacing fracture conductivity $w_f k_f$ with C_f and assuming $(p_1 - p_{cell})$ is equal to $(p_{cell} - p_2)$, Eq. 2-6 and Eq. 2-7 can be expressed as,

$$\frac{2p_{cell}\Delta pM_g}{2ZRTL} = \frac{\mu\rho q}{h_f}\frac{1}{C_f} \quad \text{..... (2-8)}$$

$$\frac{2p_{cell}\Delta pM_g h_f}{2ZRTL\mu\rho q} = \frac{\rho q}{h_f \mu}\frac{\beta}{w_f{}^2} + \frac{1}{C_f} \quad \text{..... (2-9)}$$

In Darcy flow (**Eq. 2-8**), when plotting $\frac{2p_{cell}\Delta pM_g}{2ZRTL}$ against $\frac{\mu\rho q}{h_f}$, the inverse of the slope of the line is the fracture conductivity. In turbulence flow (**Eq. 2-9**), when plotting $\frac{2p_{cell}\Delta pM_g h_f}{2ZRTL\mu\rho q}$ against $\frac{\rho q}{h_f \mu}$, the inverse of the y-axis intercept is the fracture conductivity. **Fig. 2.30** shows an example plot to calculate fracture conductivity using Eq. 2-8 by taking multiple measurement points.

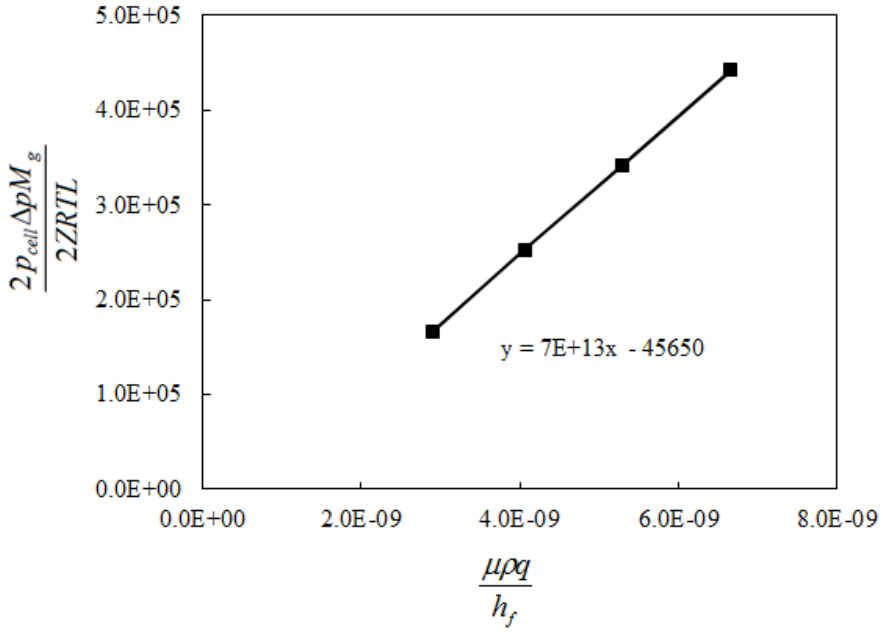

Fig. 2.30–An example plot to calculate fracture conductivity using Eq. 2-8.

2.7 Chapter Summary

This chapter introduces the shale samples, fluids and proppants, as well as the experimental apparatus used in this study. It emphasizes the key design considerations specifically for shale and the procedural challenges during sample preparation and laboratory measurement. Finally, equations to calculate fracture conductivity are presented.

3 UNPROPPED SHALE FRACTURE CONDUCTIVITY

This chapter focuses on the unpropped fracture in shale, highlighting its mechanical behavior, fracture conductivity creation and variation, and the sources of unpropped natural fracture and unpropped induced fracture conductivities. The correlation between the unpropped fracture conductivity and rock brittleness is also discussed.

3.1 Introduction

In a hydraulic fracturing treatment, the fracture might receive no proppant during fracturing for reasons that the fracture width is too small for proppants to enter, or proppants settle down to the bottom of the fracture leaving the top of the fracture unpropped, or the fracture is induced by pad but the slurry fails to transport such a long distance. After the fracture closes, the fracture faces cannot go back to its original place due to the missing debris or disturbance of the shale flakes and fragments. Thus, residual fracture width can be created. Laboratory and field tests have reported residual fracture widths that can be attributed to the combined effects of surface roughness and fracture displacement of the rock (Branagan et al. 1996; van Dam et al. 1999).

3.2 Effect of Unpropped Fracture on Production Performance

The contribution of the unpropped fracture to overall production in shale formations has been studied by Cipolla et al. (2009). In their work, it is assumed that unpropped fractures are created at the top of the cracks where the bottom part is occupied by the settling

proppant bed (**Fig. 3.1**). Different conductivities are assigned to the vertical grids to mimic the unpropped fracture, fracture arch and the propped fracture.

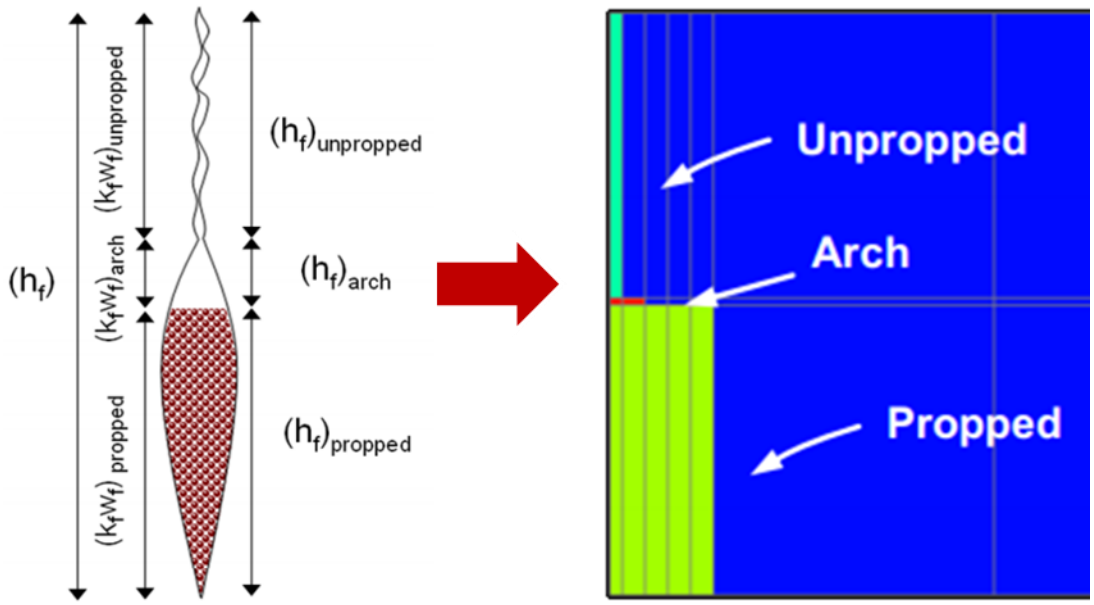

Fig. 3.1–Unpropped fracture in shale fracture networks (Cipolla et al. 2009).

The sensitivity of unpropped fracture conductivity to the cumulative production is then examined and the results are shown in **Fig. 3.2**. In this case, the proppant bed takes up 25% along the height. The arch is assumed to be propped by 100 mesh sand. Unpropped fracture conductivities vary between 0.5 md-ft and 5 md-ft. Then 10 years cumulative production is simulated. Clearly, the higher unpropped fracture conductivity leads to higher well production over the well life whether the arch is present or not. With the arch, if the unpropped fracture conductivity is 5 md-ft, one year cumulative production is about 1,300 MMscf while it is only 500 MMscf if the unpropped fracture conductivity is 0.5 md-ft. Though not reported in this study, it is expected that the production would be significantly reduced if there are no unpropped fractures.

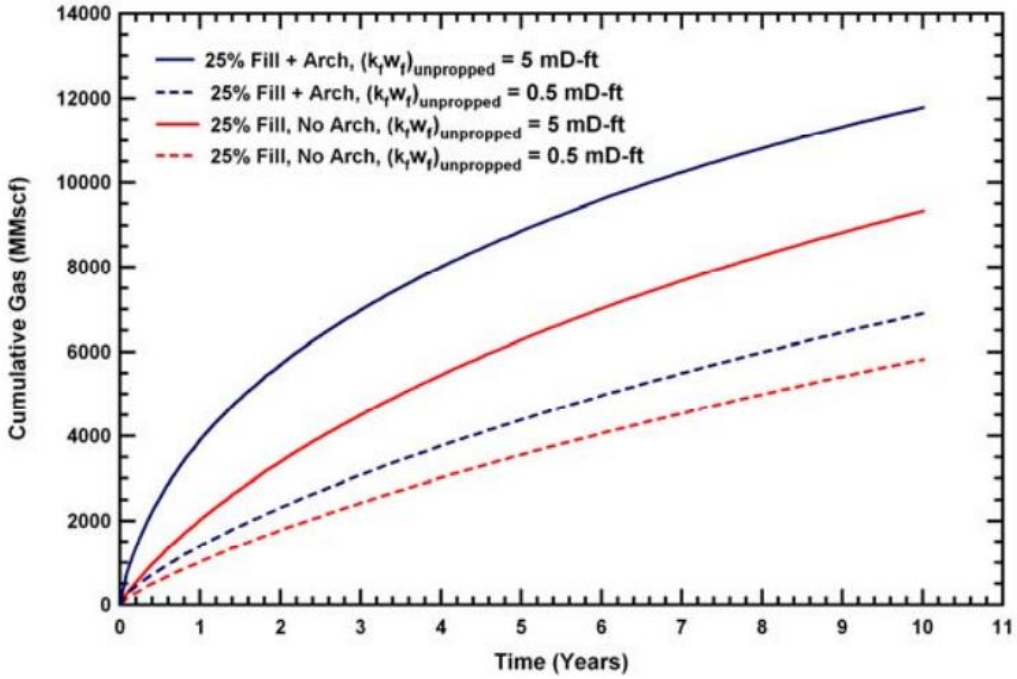

Fig. 3.2–Impact of unpropped fracture conductivity on long term well production (Cipolla et al. 2009).

It has been shown that the unpropped fracture conductivity plays a significant role in contributing to the long term well production. The following sections will discuss the mechanical features of unpropped fracture closure, the measurement and the sources of unpropped fracture conductivity.

3.3 Unpropped Shale Fracture Closure

3.3.1 Typical Fracture Closure Behavior

For natural joints or fractures, the ideal stress-strain behavior is shown in **Fig. 3.3**, where the limestone bedding is subject to the increasing normal stress. Different from the ideal stress-strain behavior where there is a distinct boundary between elasticity and plasticity, the stress-deformation curve of a limestone joint exhibits a sharp slope change until the full closure of the joint is reached. The linear elasticity region exists only at very low stress.

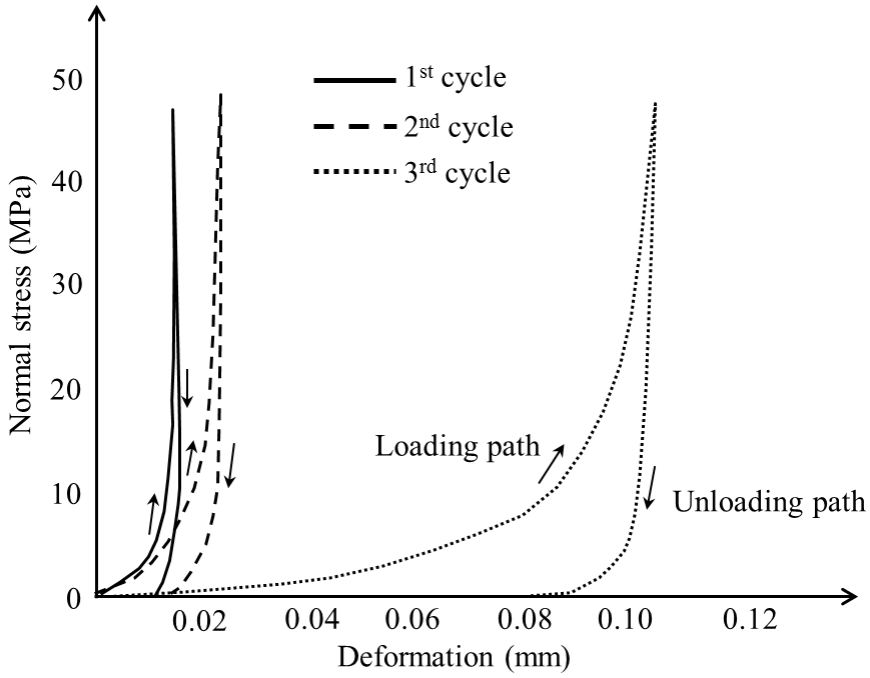

Fig. 3.3–Stress-deformation relationship of cyclic loading of natural joints (Committee on Fracture Characterization and Fluid Flow of the National Academy of Sciences, 1996).

Another interesting finding of the diagram is the unrecoverable deformation after each cyclic loading. This happens because of the crushing of the joint surface asperities

during each loading. The amount of permanent loss at each loading depends on the material strength and the rock texture.

3.3.2 Data Acquisition and Processing

Stress and deformation data are acquired by the GCTS uniaxial testing system (UCT-1000) and data acquisition system (**Fig. 3.4**). To study the shale fracture closure, we apply a load ranging from 0 to 216 kN on the rough shale fracture surface, equivalent to 0-4,000 psi closure stress.

Fig. 3.4–GCTS uniaxial testing system and data acquisition system.

The load frame has a sensor at the top of the load piston to detect its displacement. At a given stress, set the displacement reading as the initial value; then keep increasing the stress and record its displacement. The difference between the displacement and the

initial displacement is considered as the rock/fracture deformation. A step-by-step testing procedure is presented below:

(1) Prepare rock samples and measure their thickness by a caliper.

(2) Put the stack on the load frame and make sure it is aligned with the hydraulic loading piston as shown in **Fig. 3.5**. To eliminate the compressibility of the spacer rocks, the 316 stainless steel pistons are used to lift up the stack into the measurement range.

Fig. 3.5–The shale sample stack loaded on the testing frame.

(3) Gradually apply load to 10.8 kN using the load activation module; record the displacement when the load reaches 10.8 kN. These are the original values of the stress and deformation, σ_0 and d_0.

(4) Create an execution file in the GCTS data acquisition system loading from 0 to 216 kN at a rate of 5.4 kN/min.

(5) Stop the experiment; output the load and displacement files; exit.

(6) Calculate the stress and strain.

3.3.3 Stress-Strain Relationship Diagrams

Stress-strain relationship for the shale samples containing fractures reflects: (1) severity of the surface asperity crushing; (2) compaction of the laminations in the shale matrix; and (3) stiffness of the rock. The stress-strain relations of the saw-cut smooth Barnett Shale sample (**Fig. 3.6**), Barnett Shale sample containing the rough fracture, and the flat Berea sandstone sample are presented; then the stress-strain relations of the four types of shale are compared.

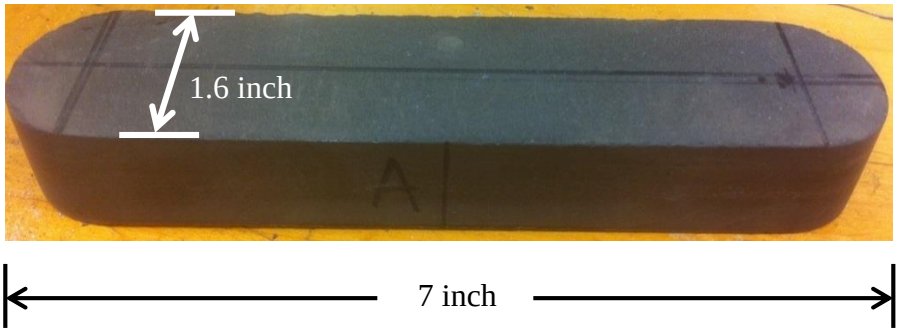

Fig. 3.6–The one inch thick flat Barnett Shale sample.

Fig. 3.7 presents the relationship between the normal closure stress and the axial strain of the Barnett Shale and the Berea sandstone samples. The flat Barnett Shale sample curve represents the averages of two samples; the rough Barnett Shale sample curve represents the averages of seven samples. It can be considered as one dimensional

stress application. All three curves exhibit the typical plastic-elastic behavior that at the lower stresses, the slope of the curve increases with higher stress. This reflects the compaction of the rocks because the rock stiffness increases as normal stress goes up. After the compaction phase, the slope of the curves keeps increasing but at a much smaller rate until it reaches the elastic deformation phase where the slopes of the curves tend to be constant.

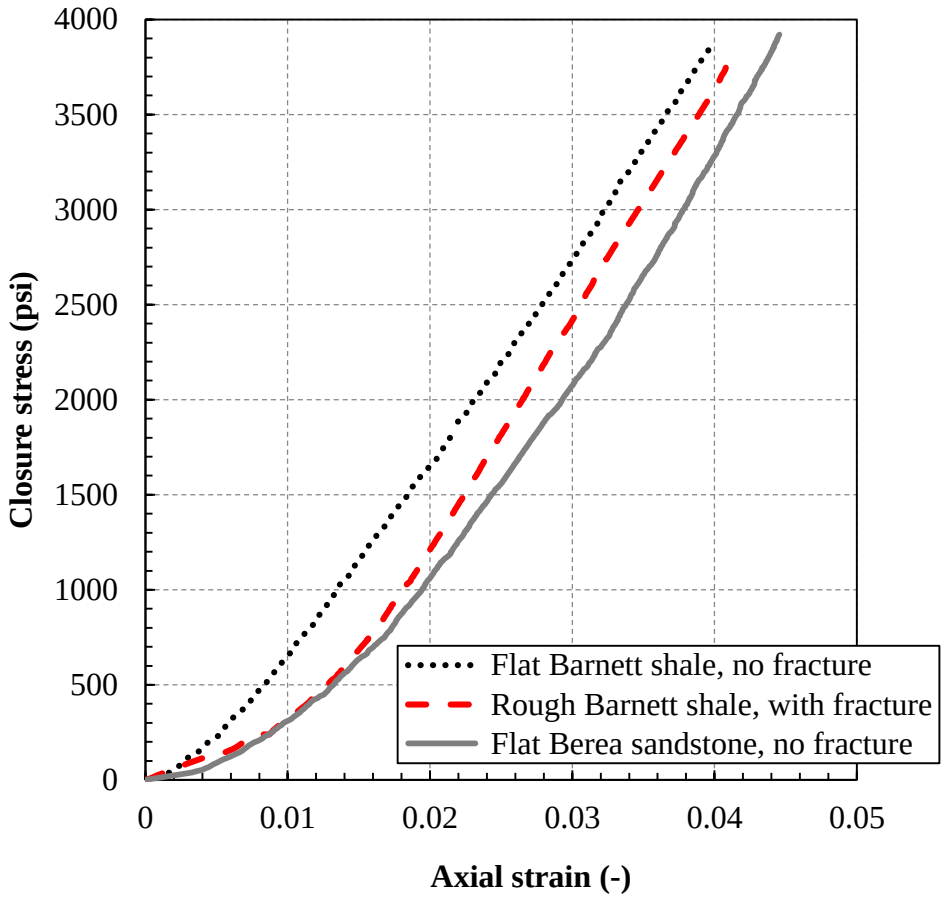

Fig. 3.7–Stress-strain relationships of Barnett Shale and Berea sandstone samples.

Because the flat rock faces allow the full rock contact to overcome the stress (no shear stress), the strain should reflect the compaction of the bedding laminations and the

creep of the matrix. The Berea sandstone exhibits a larger axial strain than the shale samples. This is caused by the poro-elasticity effect because the porosity of the Berea sandstone is 3 times higher than shale. Both pore collapse and grain failure greatly contribute to the strain increment in the sandstone.

Plasticity behavior of the flat shale sample occurs only when the normal stress is smaller than 500 psi. Above this stress, axial strain linearly increases with stress. Obviously, the final 4,000 psi normal stress is not sufficient to induce the failure of the rocks. Compared with the flat Barnett Shale slab, the sample containing rough fracture faces has the largest deformation discrepancy at stresses lower than 1,000 psi. This portion of deformation mainly arises from the fracture surface asperity failure during the normal stress application. For rough fractures, the stress acting on the fracture face in a micro-scale can be decomposed into two components with one in a direction perpendicular to the surface and the other in a direction parallel to the surface (Committee on Fracture Characterization and Fluid Flow of the National Academy of Sciences, 1996). The latter is the shear stress against the rough surface. At very low normal stress, the shear component can cause one side of the fracture to slide up and it is resisted by the frictional force between the two rough faces. This phenomenon is called "shear dilation" in soil mechanics. However, at higher normal stresses such as in a confined conductivity cell environment, the adhesion force of the surface asperity overcoming the slip can go higher than the rock strength so that the fracture surface asperities will be sheared off. Even in cases where the fracture faces are originally aligned, the micro-scale mismatching can still cause the rock surface to fail.

Towards the high normal stress region where the matrix is compacted, the flat and the rough Barnett Shale samples have parallel stress-strain curves. So, the modulus of elasticity would be close. The disparity between the two curves can be attributed to the failure of fracture surface asperities in the rough fracture. From this plot, it can also be seen that the surface asperity is not significantly crushed. So, reuse of the sample for unpropped and propped tests is reasonable.

A comparison of the stress-strain relationships for the four different types of shale is shown in **Fig. 3.8**. Obviously, the shale rocks respond to stress very differently. The Eagle Ford Shale shows the least plasticity behavior at low stresses. A linear relationship is quickly reached at 250 psi closure stress. Both the Fayetteville Shale rocks exhibit strong compaction of the shale laminations at stresses lower than 200 psi. At 2,000 psi, the strain for FL3 is 1.5 times, 3 times and 7 times as much as the strain of the FL2, the Barnett Shale, and the Eagle Ford Shale, respectively. The trend coincides with the rock fabric that FL3 consists of thin laminations stacking on each other while the Eagle Ford Shale sample is usually one solid piece.

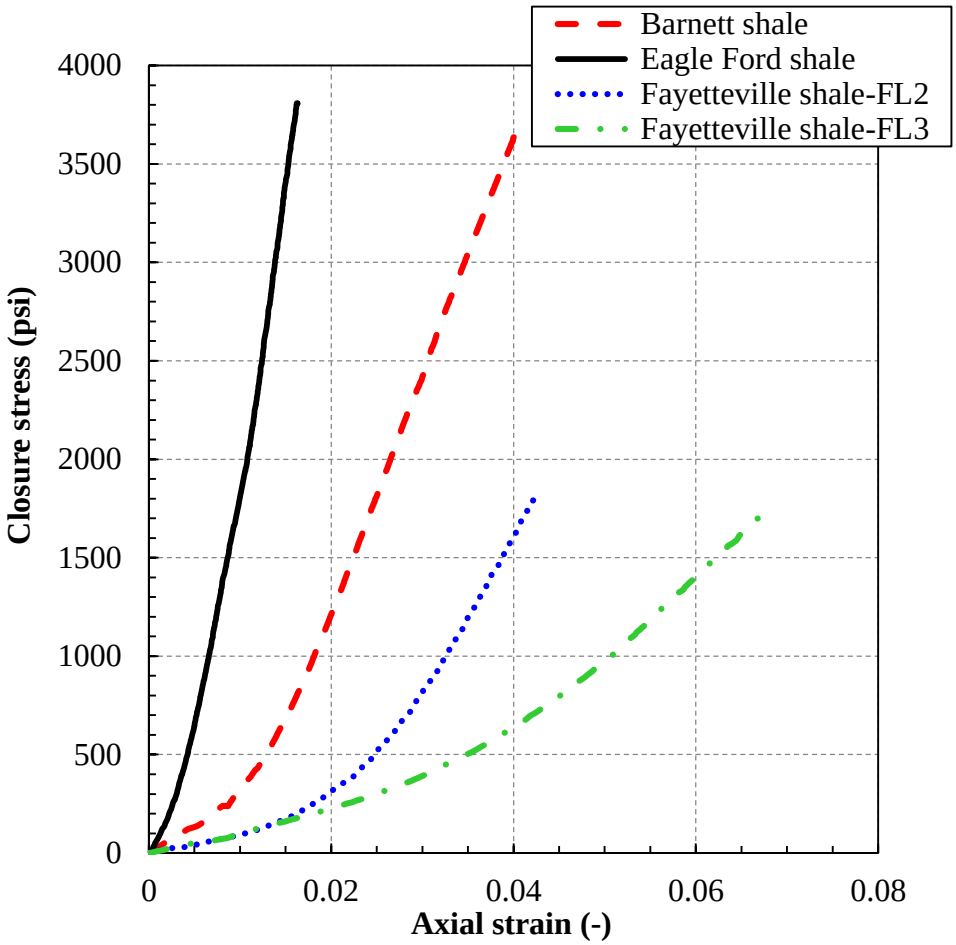

Fig. 3.8–Stress-strain relationships of the four types of shale.

Hysteresis effects in fracture deformation are common during normal stress loading and unloading, as shown in **Fig. 3.9**. Rock hysteresis is a function of the surface contact features, mineralogy, rock fabric, and if natural fractures or joints are present, the fracture infill material and its strength. In this study, the Barnett Shale is highly laminated and has high clay content. The combination of matrix compaction and fracture asperity crushing leads to the hysteresis at elevated stresses.

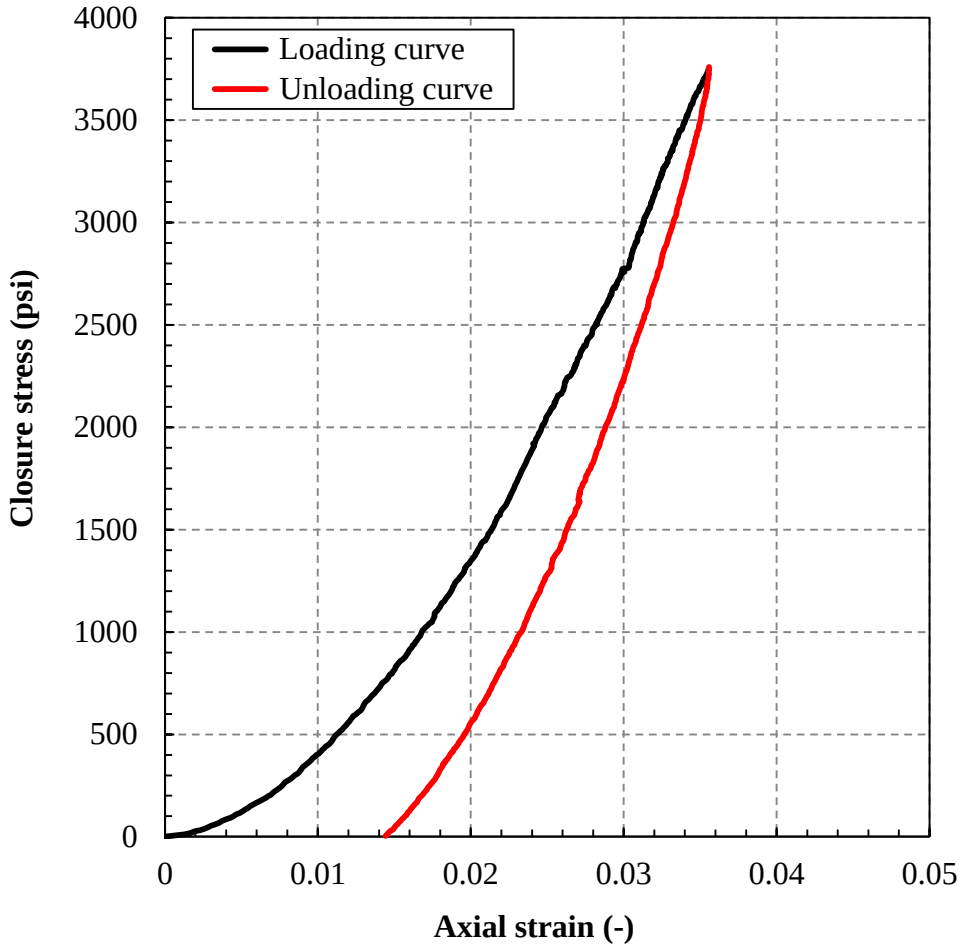

Fig. 3.9–Hysteresis of the loading and unloading curves in the Barnett Shale samples containing rough fracture surfaces.

3.4 Unpropped Natural Fracture Conductivity of the Barnett Shale

3.4.1 Characterization of the Natural Fracture

The Barnett Shale is selected for the natural fracture study because natural fractures are proven to exist in the subsurface (Gale et al. 2007) and they consistently distribute in the outcrop (**Fig. 3.10**).

Fig. 3.10–Natural fractures in the Barnett Shale outcrop.

Based on the fracture opening mode and pattern of the infill, three types of naturally fractured samples are identified in the Barnett Shale: cemented, filled and unfilled (**Fig. 3.11**). Cemented naturally fractured samples have two sides that stay attached even after the unpropped conductivity test. Different from cemented natural fractures, both filled and unfilled natural fractures are originally in the opening mode. Filled natural fractures are fully occupied with the infill material while unfilled natural fractures are just partially occupied. The classification of natural fractures will be used for the following context.

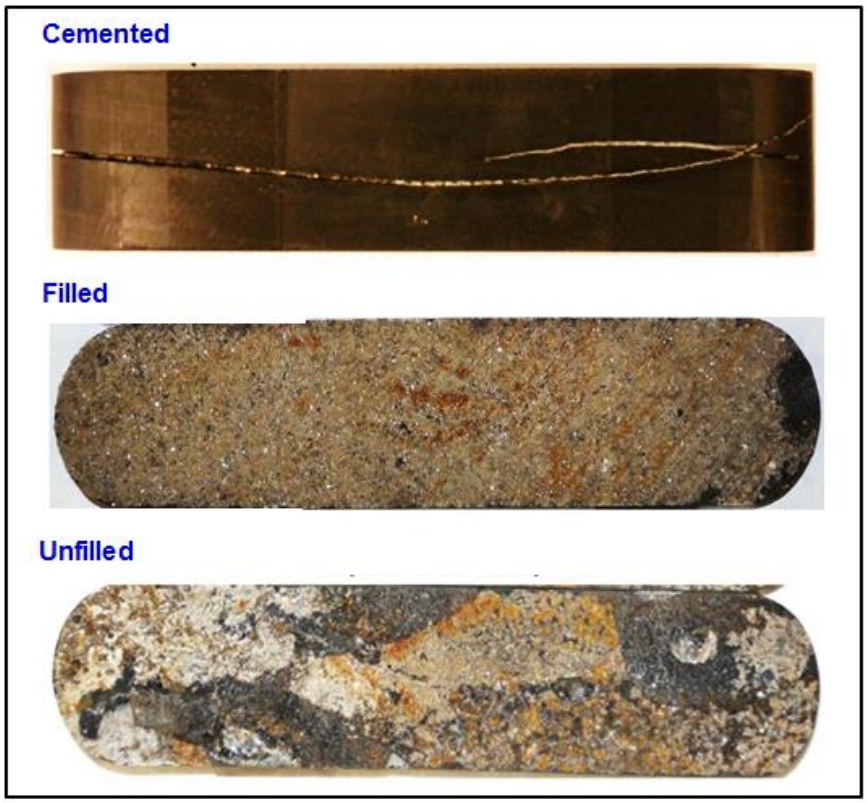

Fig. 3.11–Different types of natural fractures in the Barnett Shale.

Scanning Electron Microscope-Energy Dispersive X-ray tests show that anhydrite is the main mineral in the fracture infill (**Fig. 3.12**). Silica and aluminum indicate the residual clay impurities on the fracture surface or in the infill crystalline pores.

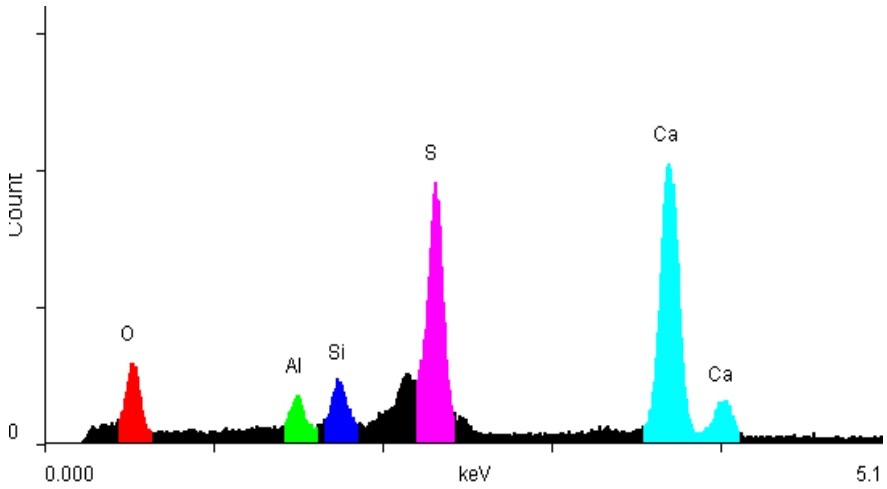

Fig. 3.12–Element intensity of the natural fracture infill in the Barnett Shale.

3.4.2 Conductivity of the Unpropped Natural Fracture

The fracture infill in the Barnett Shale natural fractures is taken into account in the conductivity measurement. For cemented and filled fractures, the infill material is kept for the unpropped conductivity measurement. Infill is removed from the unfilled natural fractures before the tests except for a few cases because the unevenly distributed anhydrite provides infinitely conductive flow paths. In the Barnett Shale, most of the samples we collected are partially filled with anhydrite with a fracture width of 0.1~ 0.2 inch under zero closure stress.

The distribution of fracture infill, its grain size and strength determine the unpropped natural fracture conductivity. **Fig. 3.13** shows the conductivity of unpropped natural fractures with infill on the fracture surfaces. As we can see, an unfilled natural fracture has larger conductivities than a filled natural fracture, and a cemented natural fracture has the lowest conductivity. At 3,000 psi closure stress, the conductivities of the three types of natural fractures are 4.1 md-ft, 1.2 md-ft and 0.37 md-ft, respectively. All

three curves decline exponentially when closure stress is over 2,000 psi. The infill material of the unfilled natural fracture distributes in the way that high conductivity channels are formed. These channels stay open even at elevated stresses.

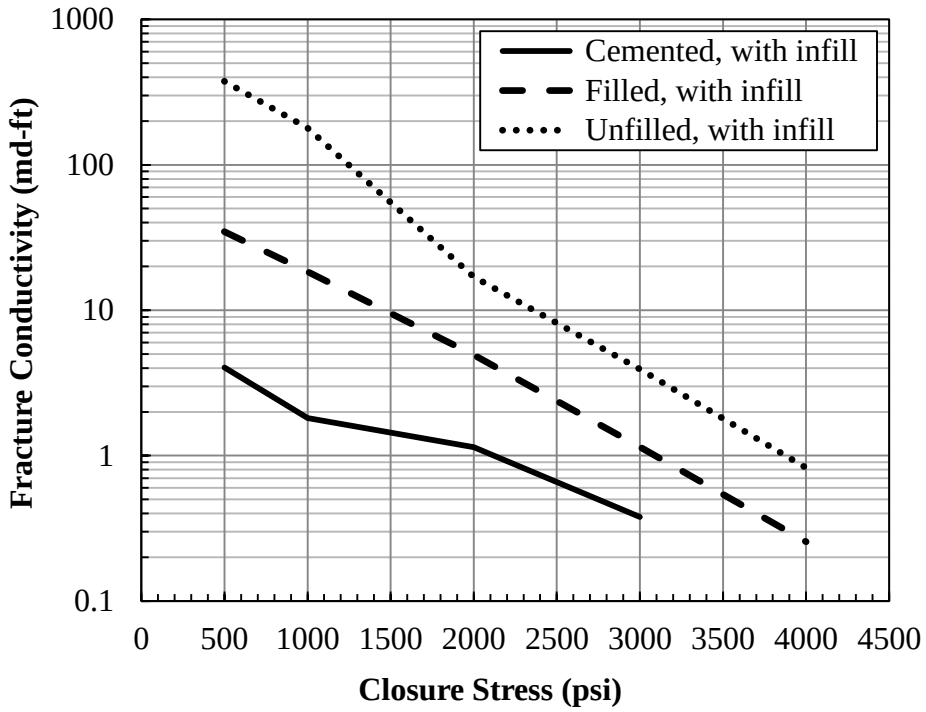

Fig. 3.13–Conductivities of unpropped natural fractures with infill.

Then the infill was removed, unpropped natural fracture conductivity was measured again. The results are shown in **Fig. 3.14**. For cemented natural fracture, anhydrite infill is so tightly attached that about 20% of the infill remains on the surface. Therefore, conductivity of the cemented natural fracture departs from the trend at 2,000 psi because the residual fracture infill still keeps the fracture open. At 4,000 psi closure stress, the 20% residual anhydrite on the fracture surface raises conductivity to 2.4 md-ft which is one order of magnitude higher than the unpropped conductivity provided by a

filled natural fracture. Conductivities vary depending on the arrangement and strength of fracture surface asperities. The deflection of the unfilled conductivity curve at 2,000 psi indicates the major failure of the fracture surface asperity; after that, fracture conductivity declines significantly to 0.7 md-ft at 4,000 psi.

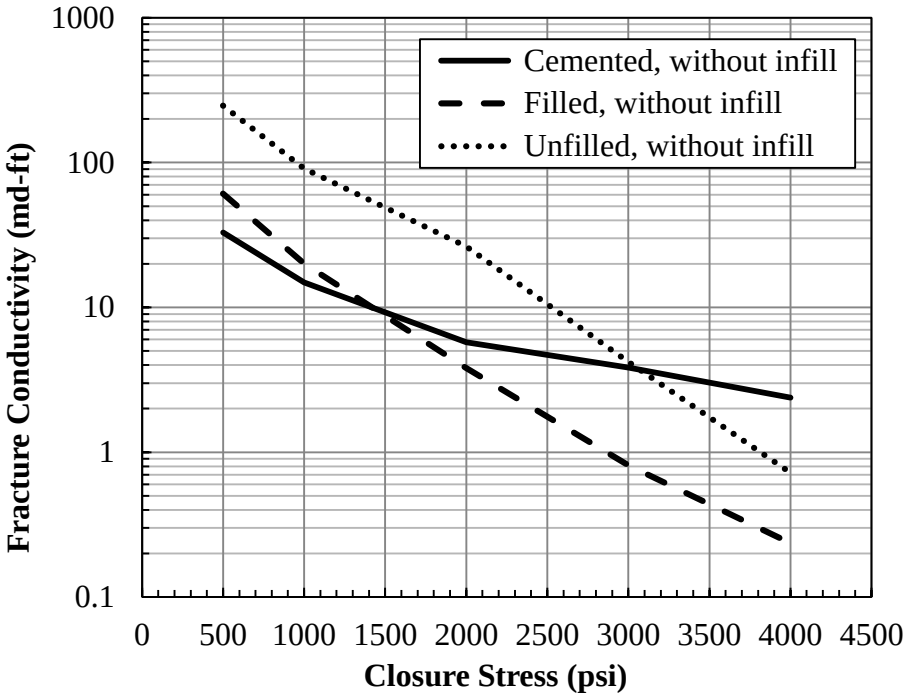

Fig. 3.14–Conductivities of unpropped natural fractures without infill.

3.5 Unpropped Aligned Fracture Conductivity of All the Shales

Aligned fractures are induced through the bedding planes and then the two parts are put back together with zero offset. Since the two parts still match on a macro-scale, the unpropped conductivity is expected to be low, if not zero. We first put the unpropped conductivities of all the Barnett Shale samples on the same plot to study the source of conductivity creation; then unpropped fracture conductivities of the Barnett Shale, the

Eagle Ford Shale and the Fayetteville Shale are compared to investigate the relationship between rock brittleness and fracture conductivity.

3.5.1 Conductivity of the Unpropped Aligned Fracture

Free particles and debris are observed when opening the Barnett Shale bedding planes. Removal of these fragments potentially creates the unpropped fracture conductivity. Conductivity drops dramatically when closure stress increases from 200 psi to 500 psi (**Fig. 3.15**). Four experiments were aborted at 1,000 psi because the conductivity was so low that it was unrealistic to wait for the gas to reach steady state. At 1,000 psi closure stress, the conductivity varies from 0.28 md-ft to 4.5 md-ft and decreases to an average of 0.71 md-ft at 2,000 psi.

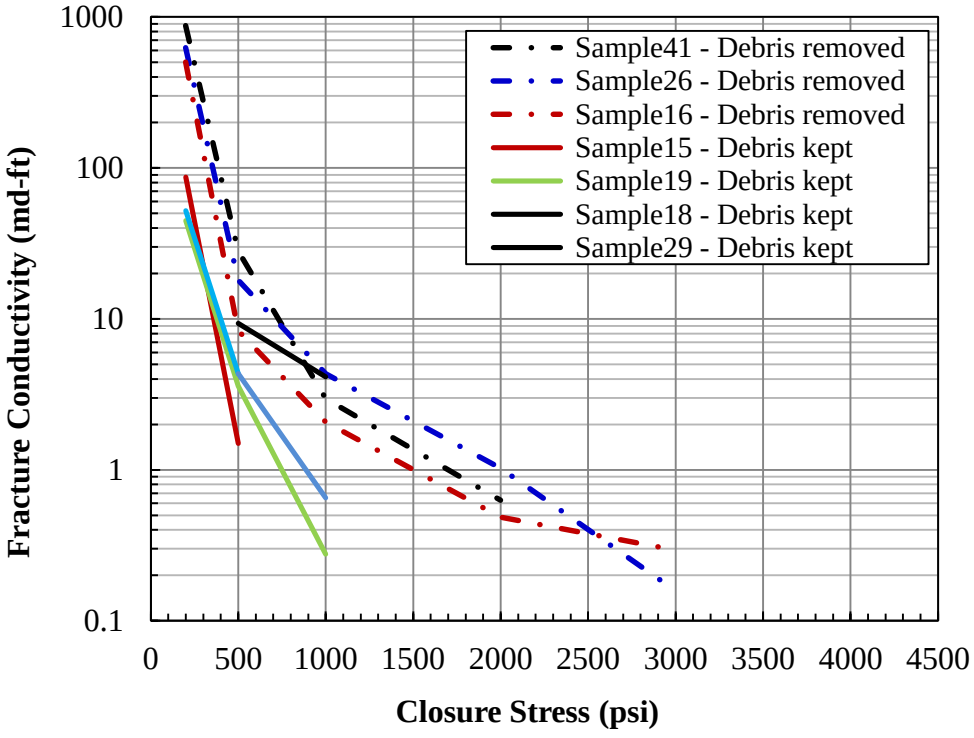

Fig. 3.15–Unpropped aligned fracture conductivity of the Barnett Shale.

The debris and particles were removed intentionally from a group of three samples before experiment. Conductivities of this contrast group after removal of the debris are represented by the dot-dashed lines. Under the same experimental conditions, at 3,000 psi closure stress, the mean conductivity is 0.23 md-ft.

Different from the natural fracture infill which is mainly anhydrite, the particles and debris we removed from the fracture faces are parts of the shale matrix. Unpropped natural fracture conductivity can be one order of magnitude higher than the unpropped induced fracture. This is mainly because the natural fracture conductivity is created by the porous infill material or larger scale unmatched surfaces, while conductivity of the unpropped induced fracture is formed by the much smaller unmatched asperities due to the removal of the limited amount of particles and debris.

Unpropped aligned fracture conductivities of different shale rocks are plotted together to study the impact of rock types on fracture conductivity (**Fig. 3.16**). Each curve represents the averages of multiple conductivity measurements. All the Barnett Shale samples were collected from locations adjacent to each other. So, they represent the same geologic formation. The Fayetteville Shale samples from zones FL2 and FL3 are tested separately. The Eagle Ford Shale was sampled from the Upper Cenomanian part of the Eagle Ford formation.

Conductivity of unpropped FL2 fracture in the Fayetteville Shale is about two orders of magnitude larger than the rest of the unpropped fractures. At 3,000 psi where conductivities of the Barnett Shale, FL3 and the Eagle Ford Shale scatter between 0.2 and 0.7 md-ft, FL2 can still maintain unpropped conductivity up to 50 md-ft. The trends of the conductivity decline for all the shale samples are similar.

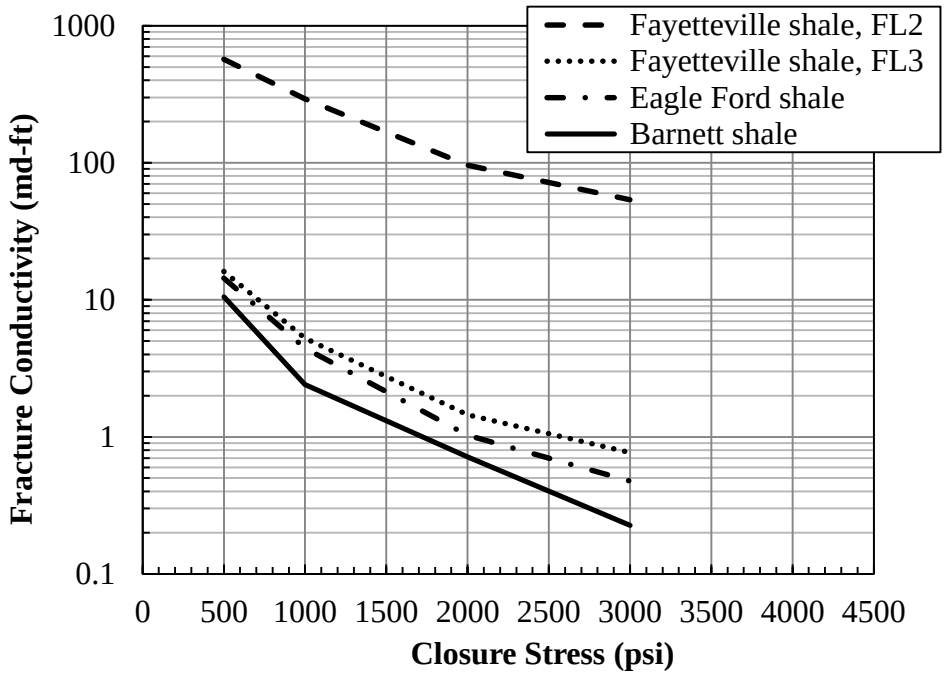

Fig. 3.16–Unpropped aligned fracture conductivity of different shales.

3.5.2 Shale Brittleness and Unpropped Fracture Conductivity

The physical process of shale flakes and clumps generation is a mechanical failure of rock mass which is dictated by the rock brittleness. Over 20 different definitions and correlations of rock brittleness are listed by Andreev (1995). While there is yet to be a universally accepted definition of brittleness, in geotechnical engineering, brittleness is considered as a material condition characterized by its reduced ability to carry load as the strain increases (Hajiabdolmajid and Kaiser 2002). Guo and Chapman (2012) pointed out that the higher quartz content in the Barnett Shale contributes to the increase of brittleness index after running experiments with formation samples. Portas and Slatt (2010) also observed an abundance of fractures in the local Woodford shale where there is high quartz content. Similar findings are also reported by Varacchi et al. (2012). Wang

and Gale (2009) modified the definition of brittleness index proposed by Jarvie et al. (2007) and it can be expressed as,

$$BI = \frac{V_{quartz}+V_{dolomite}}{V_{quartz}+V_{dolomite}+V_{limestone}+V_{clay}+V_{TOC}} \quad \text{(3-1)}$$

The denominator is almost equal to 1 for most of the shale rocks. Only trace of the dolomite is identified in shale. So, brittleness index is primarily decided by the quartz content in shale. X-Ray Diffraction tests are done to acquire the mineralogical compositions. The results are shown in **Fig. 3.17**.

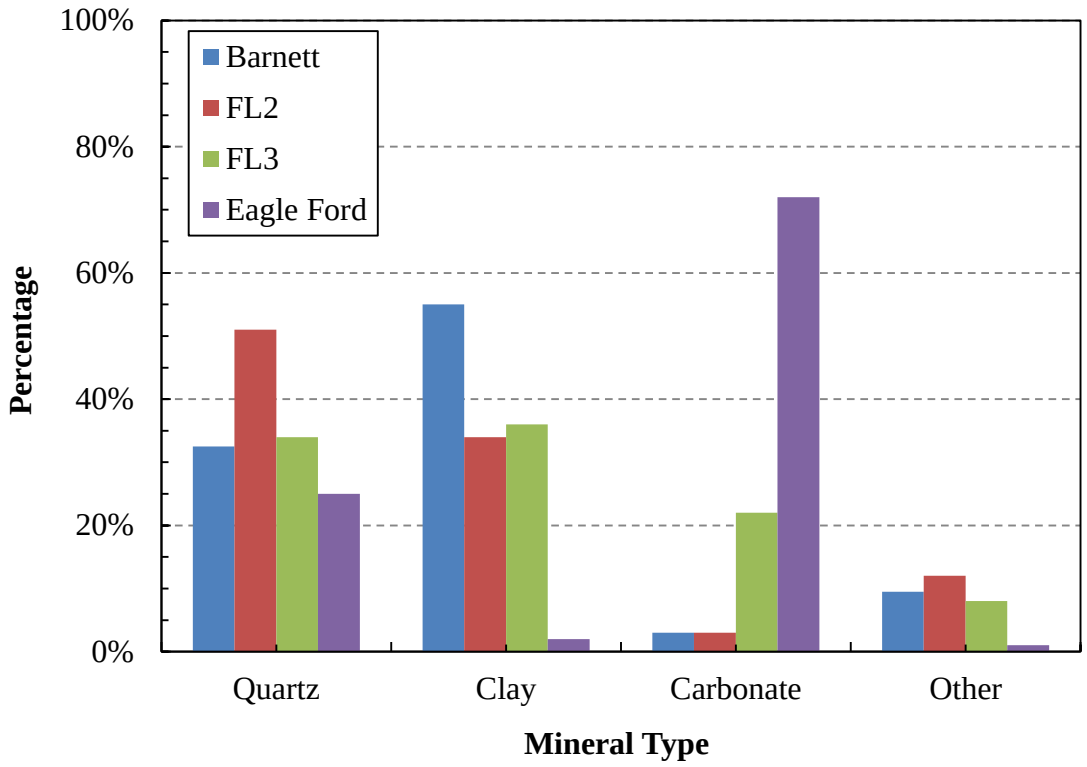

Fig. 3.17–Mineralogical compositions for the shale samples.

The Barnett Shale contains the highest clay content up to 55% and the Eagle Ford has only 2% clay. The average carbonate content in the Eagle Ford Shale is as high as 72% while for the Barnett Shale and FL2 in the Fayetteville Shale, carbonate content is only 2%. FL2 of the Fayetteville Shale contains the highest quartz content of 51% while the other three shale rocks have about 30%. Other minerals present in the shales are feldspar, pyrite and anhydrite.

Interestingly, the trend of the brittleness index is consistent with the unpropped fracture conductivity at 3,000 psi closure stress (**Fig. 3.18**). In this plot, higher brittleness index corresponds to higher unpropped fracture conductivity. The only outlier is the Barnett Shale. Considering the shale heterogeneity, this is probably due to the limited amount of Barnett Shale X-Ray Diffraction data.

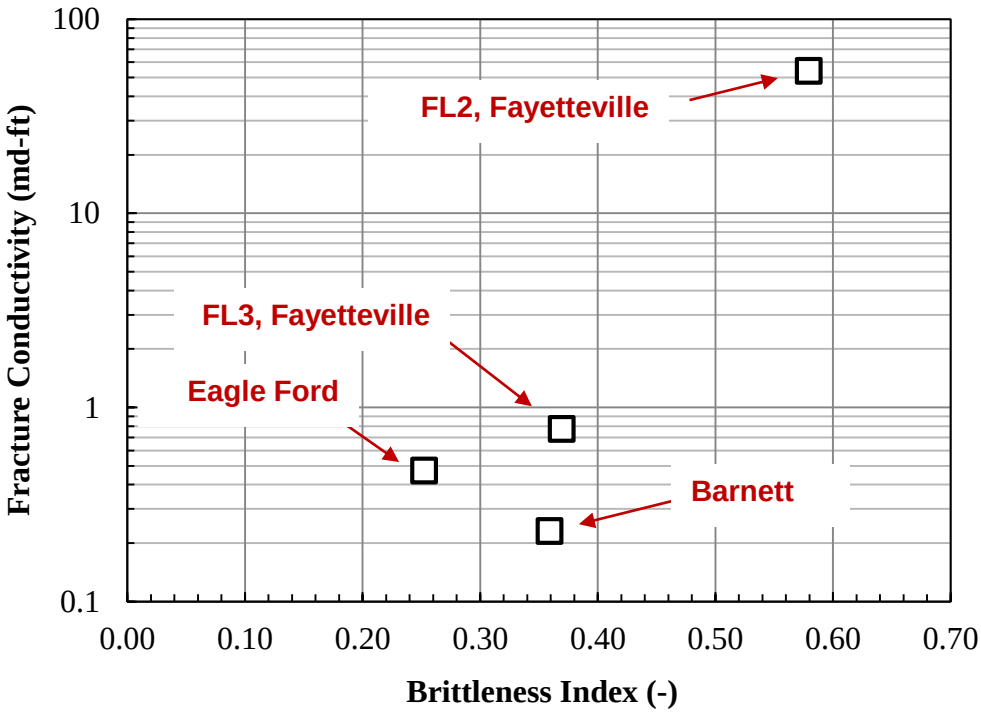

Fig. 3.18–Correlation between rock brittleness and unpropped fracture conductivity.

3.5.3 Sources of Unpropped Aligned Fracture Conductivity

It has been shown in the Barnett Shale that conductivity of the unpropped aligned fracture is created by the removal of the shale flakes, particles and fragments. The size of the debris generated from the shale fracture significantly influences the unpropped fracture conductivity. Larger pieces of debris on the fracture face have more chances to be disturbed or misaligned. The mismatched large fragments can create orders of magnitude higher conductivity than that created by tiny pieces of debris.

For the Barnett Shale, the Eagle Ford Shale and FL3, the generated particles and debris are usually small with diameters usually less than half a millimeter, typically around 200 μm (**Fig. 3.19**). This image shows the collected fracture surface particles after the conductivity test. However, the clumps dropping off from FL2 samples of the Fayetteville Shale are much larger (**Fig. 3.20**).

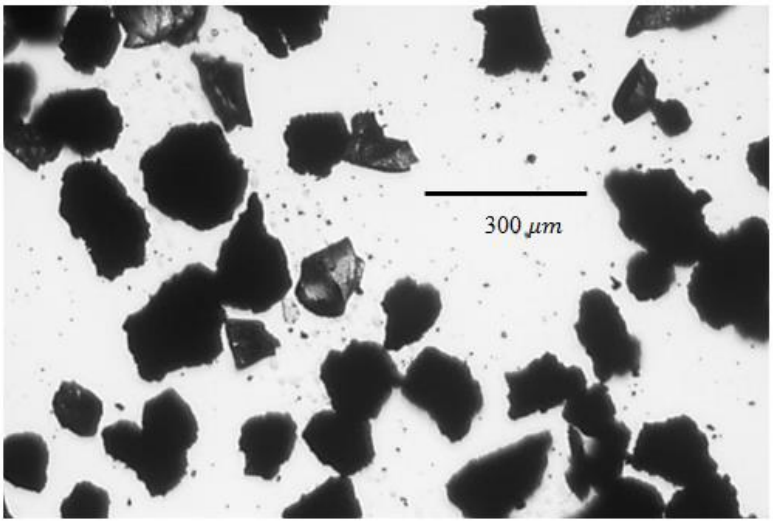

Fig. 3.19–Microscopic image of shale flakes from the Barnett Shale.

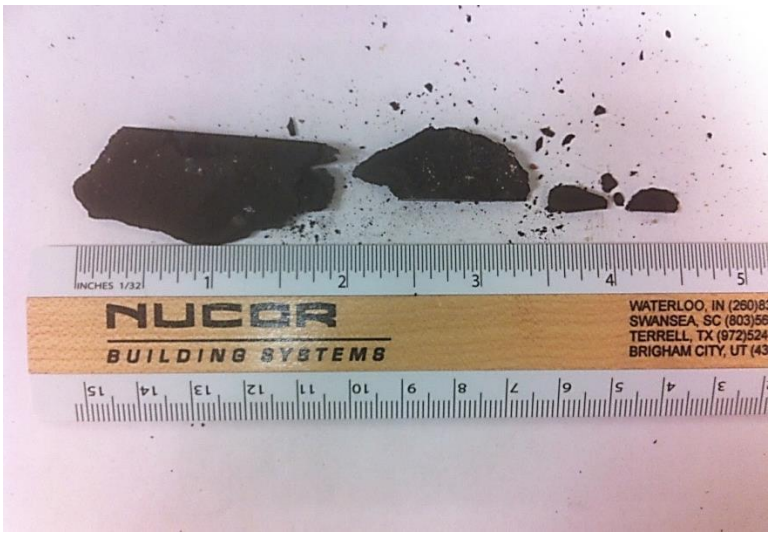

Fig. 3.20–Image of the broken shale pieces from the FL2 in the Fayetteville Shale.

Besides the fragment size, larger altitude difference between the fracture surface hills and valleys improves the chances to disturb the shale debris due to the shear component of the applied stress, and increases the unpropped fracture conductivity. **Fig. 3.21** shows the surface asperity of a typical FL2 sample. The surface valleys are usually 0.1~0.2 inch deep. On the other half of the sample, the bulges that match up with the depressions are usually loose and are easy to slide or to be sheared off under stress. Surface scanning images of the FL3, the Barnett Shale and the Eagle Ford Shale are presented from **Fig. 3.22** to **Fig. 3.24**. Surfaces of these samples are much flatter compared to FL2. The altitude difference between the peak and valley for FL2 is over 0.5 inch. The FL3 sample is smooth for most of the surface area except the plateau in the middle of the sample. The surface of the Barnett Shale fracture has large scale depressions but the altitude difference is just 0.03 inch. The Eagle Ford Shale sample shows a slope; but along the length direction, the altitude varies by only 0.04 inch.

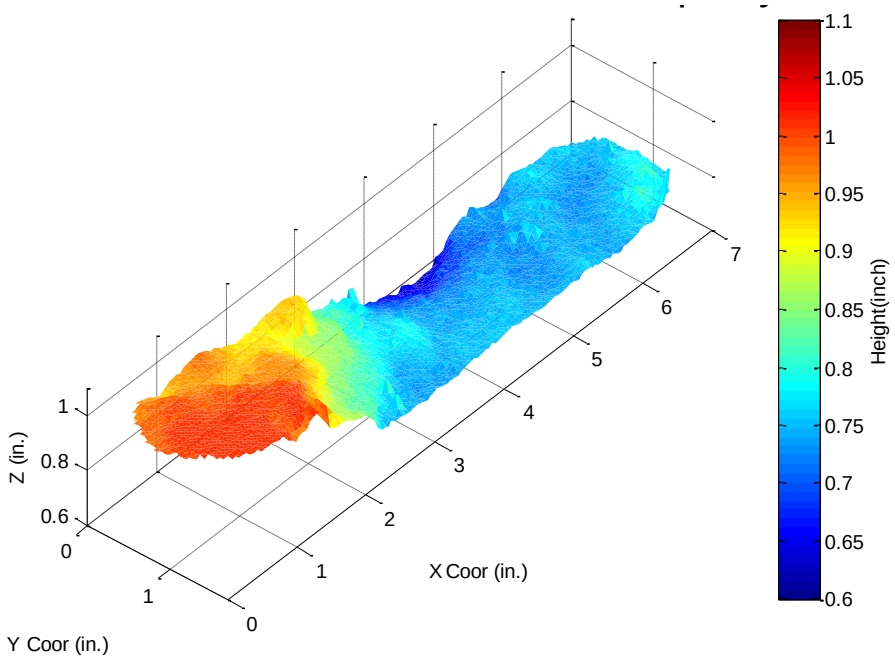

Fig. 3.21–Fracture surface asperity of the FL2 sample in the Fayetteville Shale.

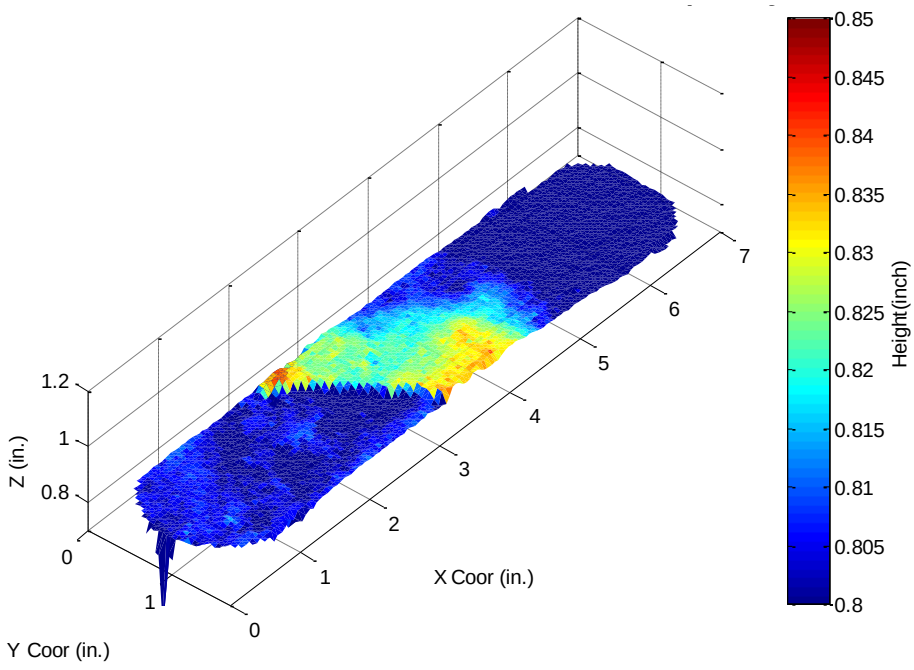

Fig. 3.22–Fracture surface asperity of the FL3 sample in the Fayetteville Shale.

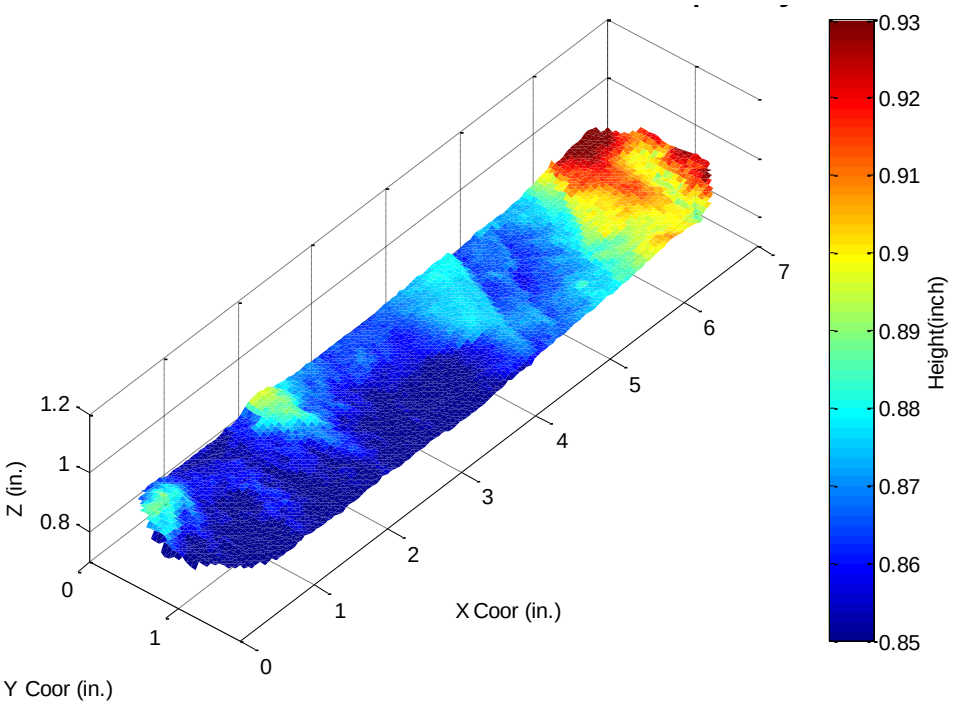

Fig. 3.23–Fracture surface asperity of the Barnett Shale sample.

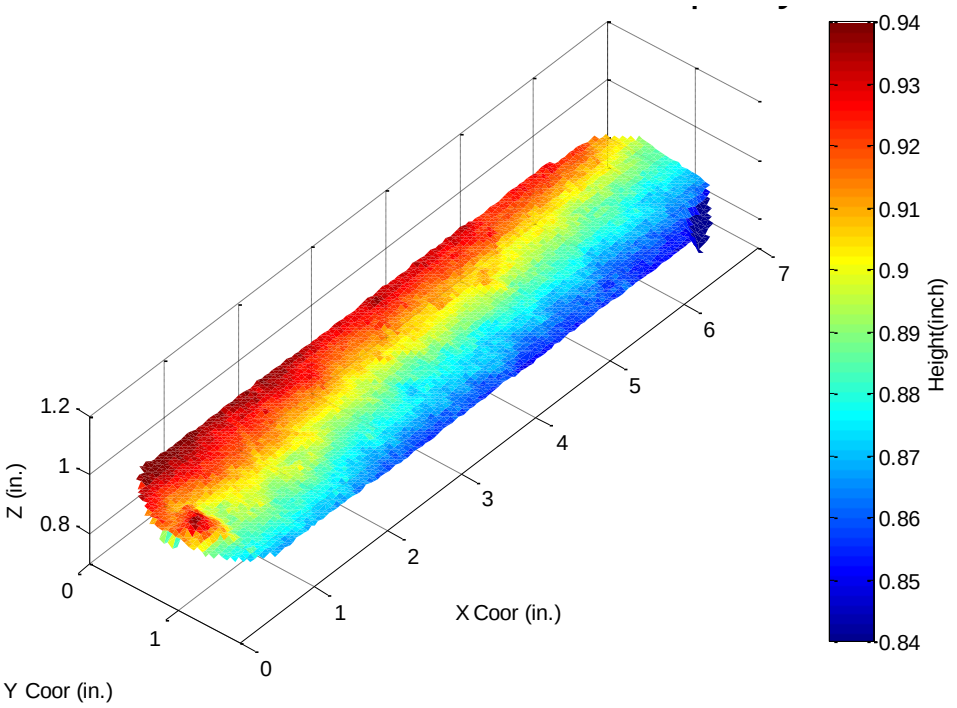

Fig. 3.24–Fracture surface asperity of the Eagle Ford Shale sample.

The creation of conductivity for the unpropped aligned shale fracture can be summarized as:

(1) Relatively high quartz content in shale increases its brittleness.

(2) Brittle rocks are more prone to rock mass failure, which generates flakes, fragments and in some cases clumps from the shale.

(3) Rock fragments can be disturbed, rearranged, or sheared off due to the shear component of the applied stress.

(4) Unpropped aligned fracture conductivity is created because the shale fracture faces cannot go back to its intact state.

3.6 Unpropped Displaced Fracture Conductivity

Rock samples are broken apart and two sides of the samples are offset by 0.10 inch. This offset is kept constant while shaping the sample into dimensions fit for the conductivity cell. The 0.1 inch offset represents the most optimistic scenario of possible unpropped fracture conductivity creation in reality. So, the conductivities measured with displaced samples are the upper bounds of unpropped shale fracture conductivity.

The particles and debris generated when inducing fractures were removed before the conductivity experiments. Unpropped fracture conductivities for the displaced Barnett Shale samples are shown in **Fig. 3.25**. In this figure, all data were obtained from different samples but under the same experimental conditions. The conductivity of an individual sample exponentially declines from 500 psi to 4,000 psi closure stress but the values vary significantly at the same closure stress. At 500 psi, the conductivity range is from 30 md-ft to as high as 855 md-ft and decreases to 0.15 md-ft to 2.6 md-ft at 4,000 psi.

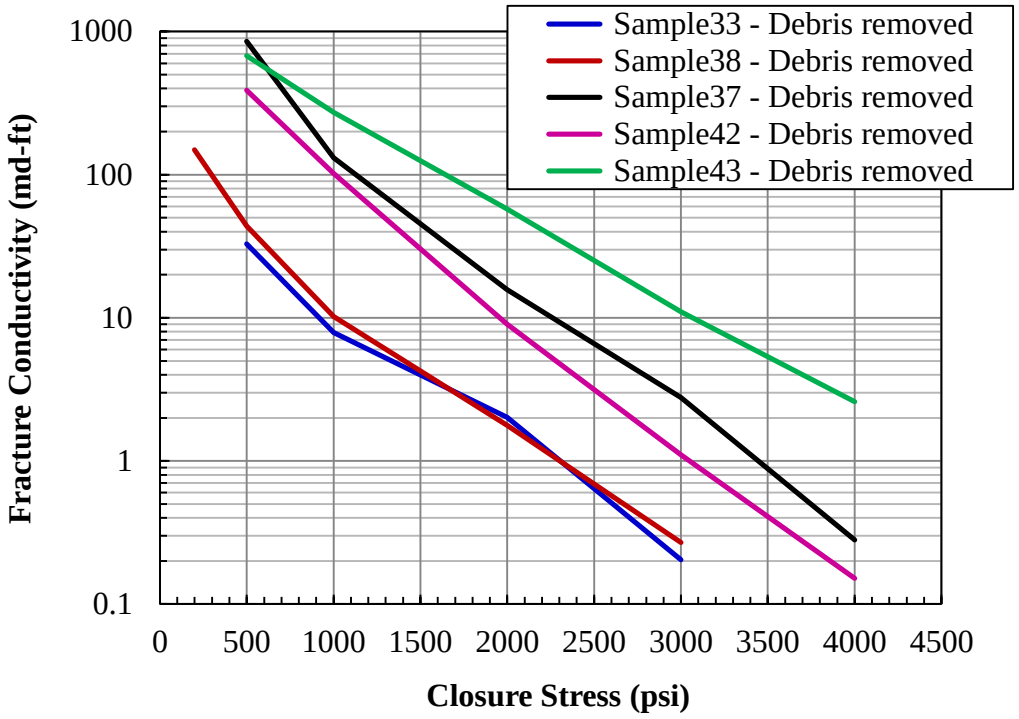

Fig. 3.25–Conductivities of the unpropped displaced fractures of the Barnett Shale.

It was recognized that displaced fracture conductivities are dependent upon the degree of fracture displacement and rock mechanical properties but with weak correlation to asperity heights (Fredd et al. 2001). Unpropped displaced fractures may have conductivities that vary by orders of magnitude depending on the shale mineralogy and mechanical properties.

Unpropped displaced fracture conductivity can be 1-2 orders of magnitude higher than that of the unpropped aligned fracture. The elevated conductivity of displaced fracture is created by the displacement of the two fracture faces and by the removal of the generated particles and debris. To illustrate the mechanism of the displaced fracture conductivity creation, we use the profilometer to scan one side of the sample surface and match up with the corresponding location on the other side (**Fig. 3.26**). The fracture

surface asperity for both sides is shown in **Fig. 3.27** where the residual widths can be found.

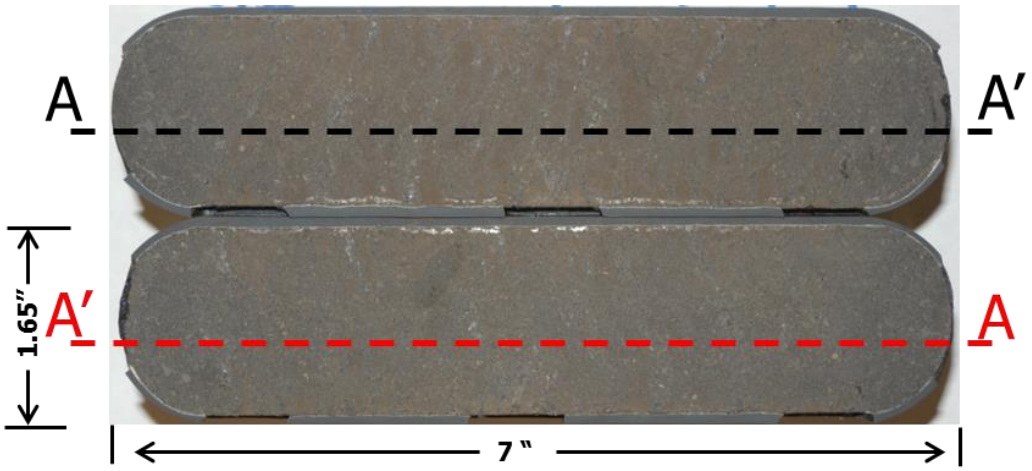

Fig. 3.26–Scanning the Barnett Shale fracture surface using a surface profilometer.

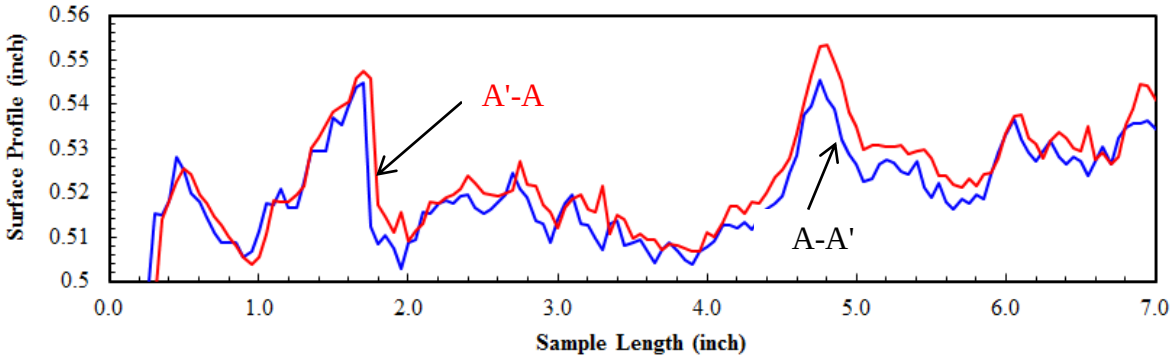

Fig. 3.27–Surface profilometry of the Barnett Shale fracture.

3.7 Chapter Summary

This chapter focuses on unpropped fracture conductivity for shale. A typical stress-strain relationship diagram is presented to understand the unpropped fracture closure process. Then, we reported the unpropped natural fracture conductivity, unpropped aligned

fracture and unpropped displaced fracture conductivities. Particularly, we correlate the shale brittleness with fracture conductivity and integrate the shale mineralogy, fracture surface profiles with fracture conductivities to investigate the sources of conductivity creation in the aligned fractures and displaced fractures.

4 PROPPED SHALE FRACTURE CONDUCTIVITY

This chapter first introduces the experimental results of propped fracture conductivity under low proppant concentrations and compares the propped fracture conductivity with the unpropped fracture conductivity. Then, details on how to predict propped fracture conductivity based on the solution of a population balance equation are presented.

4.1 Introduction

Compared with hydraulic fracturing in conventional reservoir rocks, fracturing in shale tends to pump smaller size proppants at lower concentrations. Standard API tests measure fracture conductivity at the concentration of 2 lb/ft^2, which is much higher a value than the real fracture design can obtain. However, there are many challenges in the low concentration proppant placement at the lab scale for reproducible and representative measurements. The rough fracture surfaces in this study complicate the proppant behavior under stress because the sands are much more unstable on rough surfaces than on smooth surfaces. Only the Barnett Shale samples were used for this part of the study.

This chapter presents the measurement of propped fracture conductivity and more importantly, how to predict the propped fracture conductivity given proppant information, reservoir conditions and fracturing design.

4.2 Propped Fracture Conductivity of the Barnett Shale

4.2.1 Uncertainties of Proppant Sampling and Placement

The discrepancy in conductivity measurements under the same conditions can be attributed to the broad proppant size range. For example, 40/70 mesh sands only contain 30% sands that have diameters falling between 50 mesh and 60 mesh. The remaining 70% of the sand grains have diameters either smaller than 60 mesh or larger than 50 mesh. The proppants mass needed for certain areal concentration is the product of the concentration and the fracture surface area. With 10 $inch^2$ fracture surface area, proppant mass for 0.1 lb/ft^2 is 3.2 grams. The proppants are randomly sampled from a 5-gallon bucket. So, there is a great chance that each sampling of the 3.2 grams contains different size distributions. Sieving 3.2 grams of sand is challenging because the sieve analysis requires much more sand to account for the mass loss during shaking.

One solution to this problem is to sieve the proppants and put each size range into separate bags. Then sample the proppants from each size range as per the particle size distribution by the field report. For example, to collect 40/70 mesh sands at 0.1 lb/ft^2, **Table 4.1** can be used to sample from each size range for the total 3.2 grams. Proppant allocation for other concentrations can be derived from this table.

Table 4.1–Sand mass needed for each size range to mix 40/70 mesh Badger sand at the concentration of 0.1 lb/ft^2.

Size range (mesh)	30-40	40-45	45-50	50-60	60-70	70-100
Proppant mass (gram)	0.112	0.582	0.864	0.973	0.566	0.102

The difference in proppant layout on rough fracture surfaces is another cause for varying conductivities under the same experimental conditions. The placement of proppants on rough surfaces at low concentrations is challenging because realistically, the ideal "even distribution" of proppants cannot be achieved (**Fig. 4.1**). In an ideal distribution, proppant pack widths are the same everywhere as shown in Fig. 4.1(a). This is practically impossible to realize on rough surfaces because proppants roll on slopes. The realistic distribution of sands shown in Fig. 4.1(b) has varying pack widths on the fracture face because the sands tend to collect in the surface valleys while the hills receive no proppants or simply form a monolayer of proppants. The initial fracture width of the realistic case is larger than the ideal case. To account for this uncertainly, we run multiple experiments at the same conditions and calculate the average conductivities.

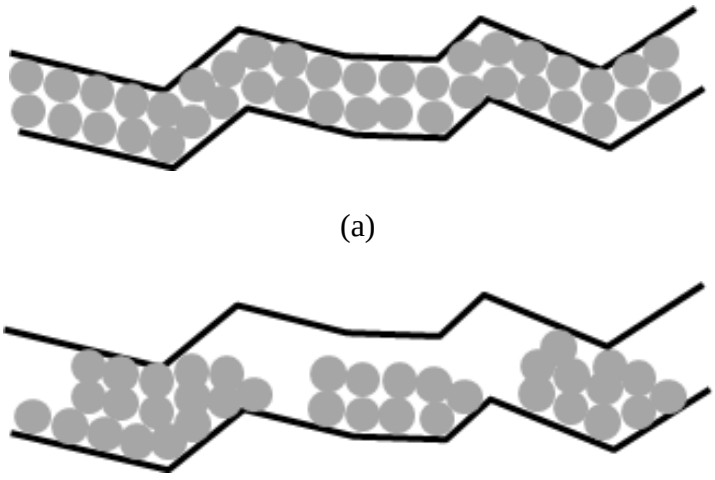

(a)

(b)

Fig. 4.1–Proppant placement on rough fracture surface: (a) ideal proppant packing; (b) realistic proppant packing.

4.2.2 Conductivity of the Propped Shale Fractures

The propped natural fracture conductivity is measured using the Barnett Shale samples. As we mentioned earlier, there are three types of natural fractures identified in the Barnett Shale: cemented, filled and unfilled. For cemented natural fractures, most of the fracture infill was removed with about 20% firmly attached to the fracture face. The 20% residual fracture infill was kept during propped conductivity test so that the surface asperity would not be disturbed during the removal process. For filled natural fracture, tests with infill and without infill were conducted. Infill of the unfilled natural fractures was removed before placing proppants. A sponge paint brush was used to remove the infill to avoid the surface asperity change.

By comparing the conductivity of filled natural fractures with 100 mesh sand at 0.06 lb/ft^2 before and after removing the infill (**Fig. 4.2**), we find that conductivity with infill in the fracture is lower than that without infill. This is because the small grains of 100 mesh sand enter the inter-particle pores of the infill and reduce the flow path. Conductivity is dominated by the unsorted fracture infill if it is present. A mismatched fracture surface was created after the fracture infill is removed. The presence of the proppant pack even with 100 mesh sand can greatly improve fracture conductivity.

Conductivities of 40/70 mesh sand at 0.06 lb/ft^2 are measured with filled and unfilled natural fractures (**Fig. 4.3**). The discrepancy between the two curves becomes smaller at higher closure stresses, indicating less impact of surface asperity on conductivity than proppant pack. The concentration of 0.06 lb/ft^2 is sufficient to create a multi-layer sand pack. Together with the evidence of lower conductivity reduction rate

with increasing closure stress, the proppant pack dominates the conductivity of propped natural fractures at concentrations higher than 0.06 lb/ft^2.

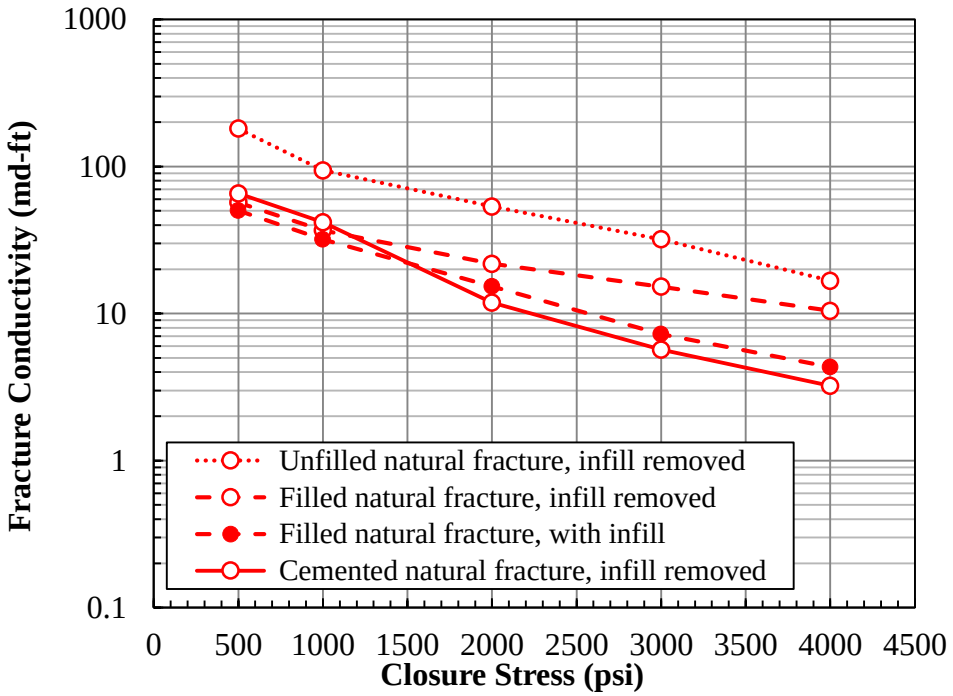

Fig. 4.2–Conductivities of propped natural fractures, 100 mesh, 0.06 lb/ft^2.

Conductivities of propped aligned fractures are plotted to study the effect of proppant size and concentration as well as to contrast with unpropped fracture conductivity. Within the size and concentration range in this study, higher proppant concentration leads to higher fracture conductivity with the same size proppant; larger sand consistently provides higher conductivity than smaller sand at the same concentration (**Fig. 4.4**).

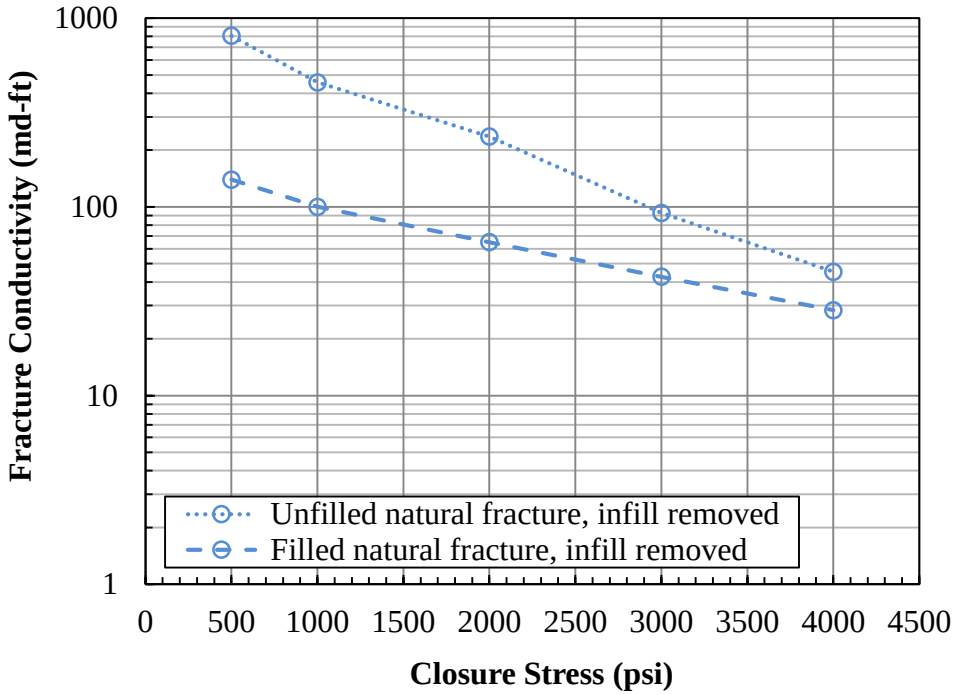

Fig. 4.3–Conductivities of propped natural fractures, 40/70 mesh sand, 0.06 lb/ft^2.

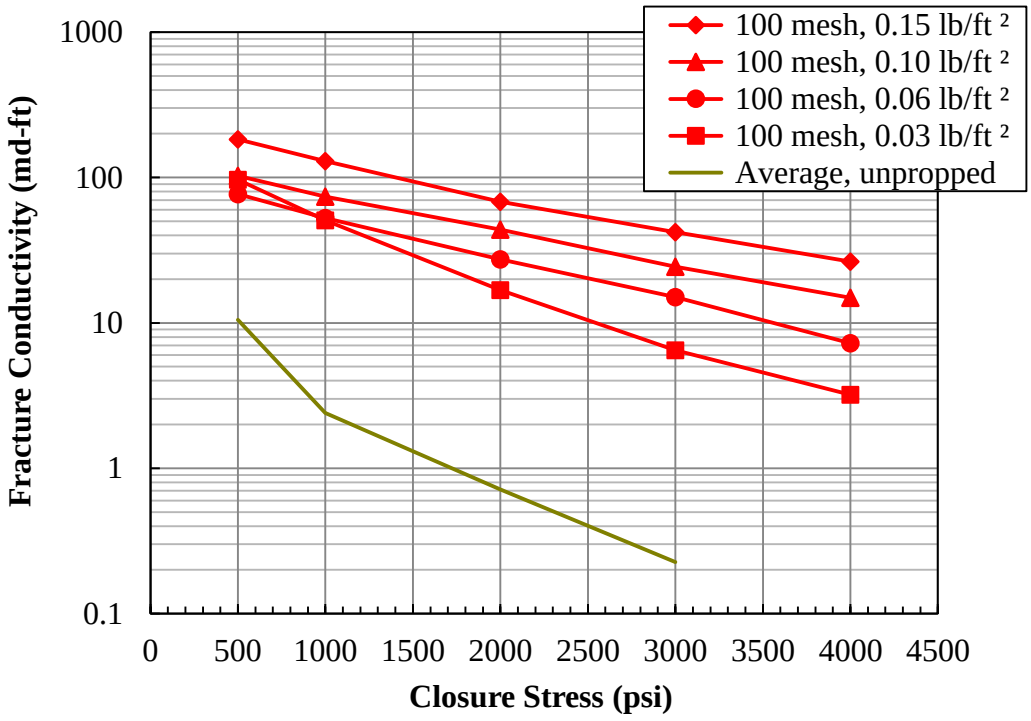

Fig. 4.4–Conductivities of propped aligned fractures.

An interesting observation is the significant conductivity increment with 100 mesh sand at 0.03 lb/ft^2 compared with unpropped fracture conductivity. This is mainly caused by the uneven distribution of sands at the ultra-low concentration so that the fracture closes on the surface valleys where multiple sand layers are collected. At 0.03 lb/ft^2 concentration, conductivity declines at a higher rate with increasing stress due to more chances of point loading and closure of the unpropped fracture faces. An image of the 100 mesh sand on the fracture face at 0.03 lb/ft^2 after the experiment is shown in **Fig. 4.5**.

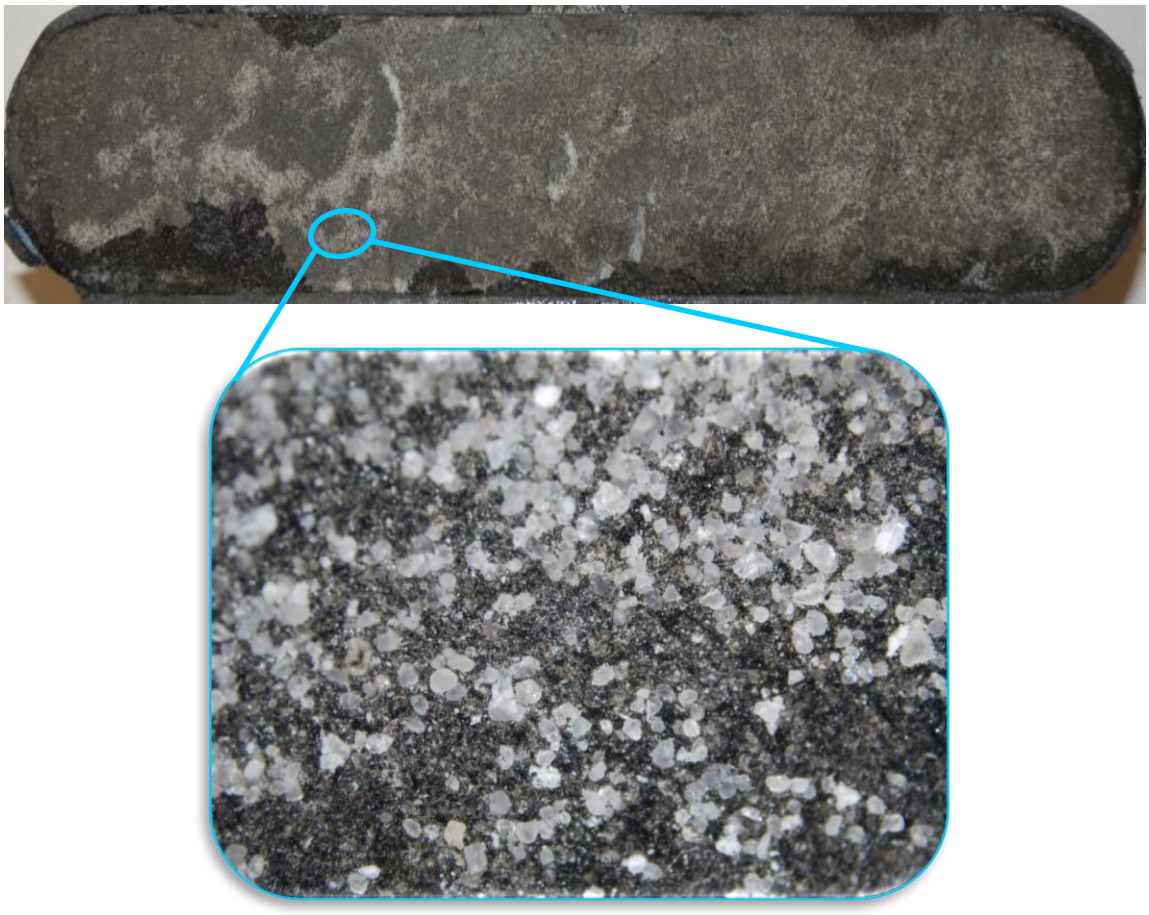

Fig. 4.5–Proppant distribution after experiment with 100 mesh sand, 0.03 lb/ft^2.

Fig. 4.6 shows the conductivities of displaced fractures propped by 100 mesh sand at concentrations of 0.03, 0.06, 0.10 and 0.15 lb/ft^2. Conductivities all decline exponentially with increasing closure stress. Interestingly, the unpropped displaced fracture supported by randomly distributed surface asperities outperforms propped fracture conductivities at lower closure stress. With increasing stress, unpropped fracture conductivity drops quickly and the advantage of proppants is demonstrated by the fact that higher sand concentration results in higher fracture conductivity.

Surface topography of displaced fractures can be altered due to the asperity crushing. Direct evidence was observed from the dark grey particles mixed with the proppants collected after experiment. Besides, the fracture surface exhibits parallel strips of crushed asperities due to rock failure at the contact locations as highlighted in **Fig. 4.7**. Nevertheless, the change in surface asperity is believed to be mitigated by the presence of multiple sand layers. This can be reflected by the conductivity decline rate over closure stress. By comparing conductivities of the propped aligned fractures with the propped displaced fractures, we find that the fracture displacement has a minor influence on propped fracture conductivity over various concentrations.

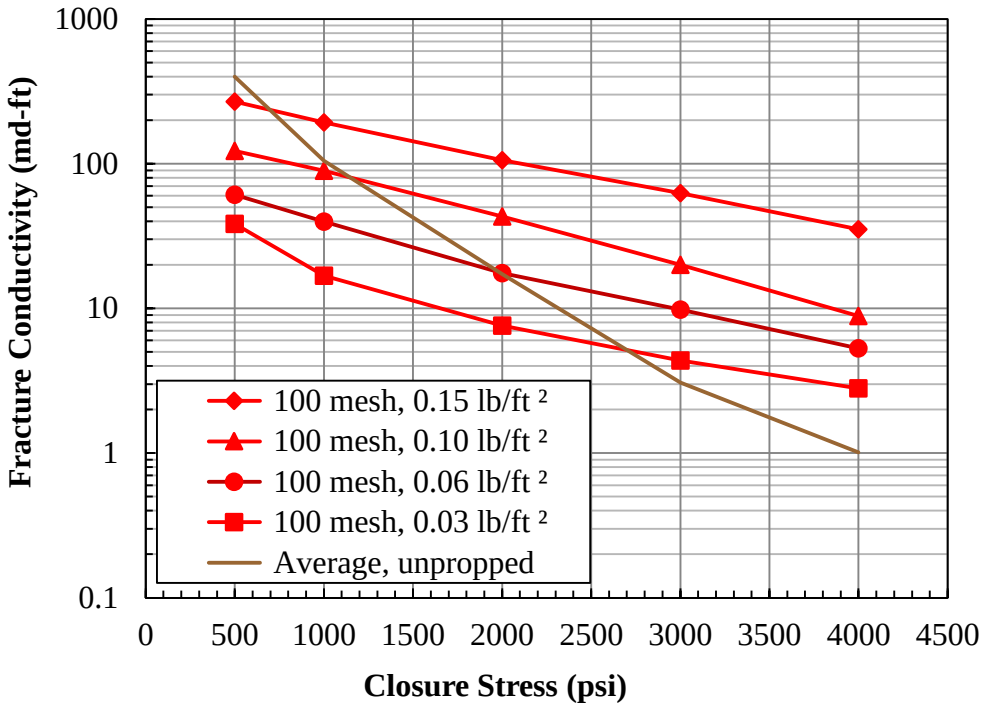

Fig. 4.6–Conductivities of propped displaced fractures and unpropped displaced fractures.

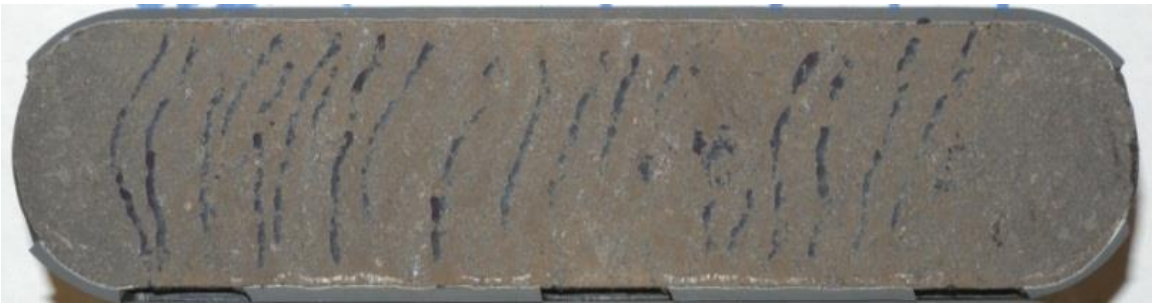

Fig. 4.7–Fracture surface marked to show crushed asperities on a displaced fracture.

4.2.3 Crushing of Partial Monolayer Proppants on Rough Surfaces

Bigger sand particles tend to create a proppant partial monolayer on the fracture surface at low concentrations. The partial monolayer exhibits higher fracture conductivity at lower closure stresses, because the sparsely distributed grains on the fracture surface

create flow channels around them which provide a better conduit for fluid flow than the interconnected pore spaces within the proppant pack. However, at elevated closure stresses the monolayer cannot maintain high conductivity because the stress on each grain becomes too high and many of these sand grains experience point loading. As shown in **Fig. 4.8,** conductivity at 0.03 lb/ft^2 is higher than conductivity created by 0.10 and 0.20 lb/ft^2 when closure stress is lower than 2,000 psi; at elevated closure stress, conductivity increases with higher proppant concentration.

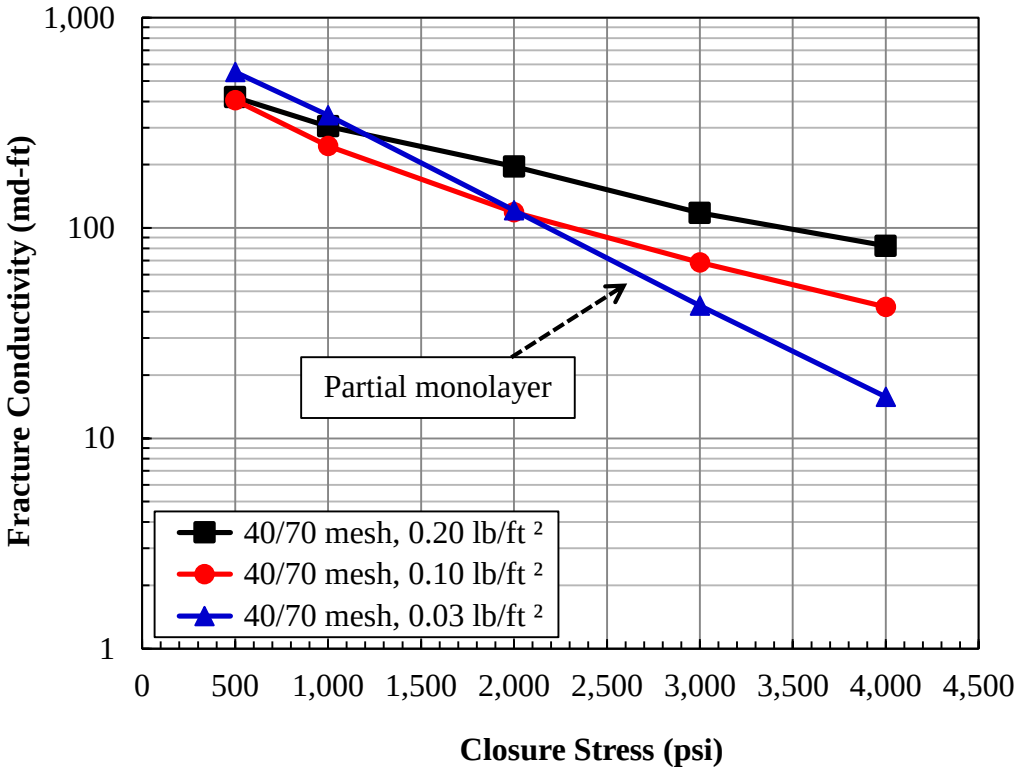

Fig. 4.8–Propped fracture conductivity with 40/70 mesh sand at 0.03, 0.10, and 0.20 lb/ft^2.

One critical parameter during particle crushing in granular packs is the interparticle coordination number. It is defined as the number of contacts with its

neighbors for a single grain. Palisch et al. (2009) found that in the proppant pack, exterior grains experience greater damage than interior grains because the latter are stressed uniformly (**Fig. 4.9**). For the same consideration, the protocols in ISO 13503-2 (2006) for proppant evaluation recommend 4 lb/ft^2 in the crush tests. However, in our experiment, the common proppant concentration is just 0.1 lb/ft^2. The sand layers in our experiments are much thinner than the width acquired from experiments in compliance with ISO 13503-5 (2006) where 2 lb/ft^2 proppant concentration is recommended for fracture conductivity tests. The low concentration sands have less coordination number and are more subject to being crushed due to uneven stress loading or point loading. Thus, excessive proppant crushing is expected to happen on rough fracture surfaces at experiments under low sand concentrations.

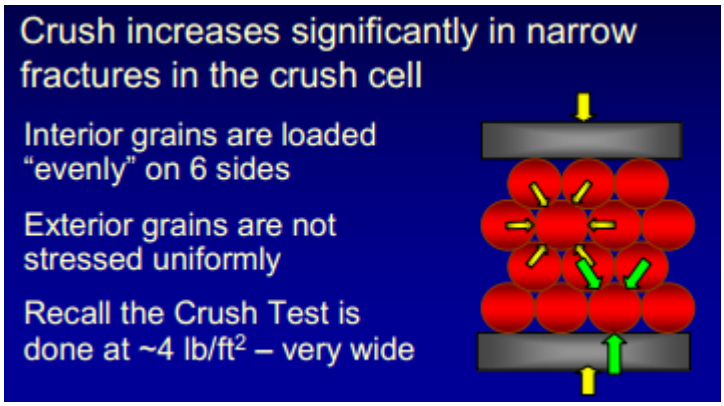

Fig. 4.9–Exterior grains have fewer contact points and have increased damage (Palisch et al. 2009).

There is very little publication about proppant crushing on rough surface in the area of petroleum engineering. The ISO recommended practices utilize flat sandstone sample, and the normal stress applied on the 2 lb/ft^2 sand pack can be considered as

uniaxial normal compressive stress. Proppant concentration at 2 lb/ft^2 is sufficient to create multiple layers. At closure stresses below the yield stress provided by the vendor for a specific type of proppant, its crushing tends to be overlooked. This might be reasonable for multiple sand layers placed on flat sandstone sample where normal compressive stress occurs. But for the shale sample preserving surface roughness, proppants at low concentrations experience different stress conditions and the crushing behavior is different. This stress status of proppants at particle level is illustrated in **Fig. 4.10**.

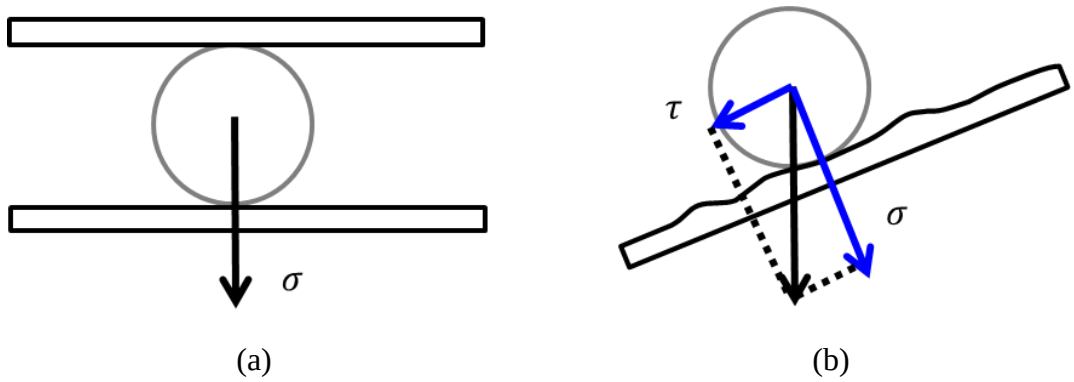

Fig. 4.10–Stress status of proppant at the particle level: (a) particle subject to vertical closure stress on flat fracture face; (b) particle subject to vertical closure stress on rough fracture face where the vertical stress is decomposed of the normal stress $\boldsymbol{\sigma}$ and shear stress $\boldsymbol{\tau}$.

The topic of particle crushing has been studied on both particle-level and cluster-level in the area of mineral processing such as aggregate production. Guimaraes et al. (2006) investigated the crushing of particles subject to normal stress and shear stress experimentally. In their experiments, Ottawa sands with diameter between 0.60 mm and 0.85 mm (mean diameter 0.73 mm, about 30 mesh) were used. They tested both loose

sands and dense sands (**Fig. 4.11**). The test apparatus and general procedure were reported by Guimaraes et al. (2006).

From these plots, we can see that loose packing consistently experiences more crushing than the dense packing because dense packing sands have more points of contact with their neighbors. The data also shows that the application of simple shear stress induces a significant increase in fines generation when the particles are simultaneously normally loaded to 2000 psi.

The message delivered by this study clearly indicates that the low concentration sands loaded on the rough fracture surface experience more damage than the flat fracture face when the closure stress is applied to 4,000 psi (≈ 28 MPa). Fredd et al. (2001) also found that there was a significant reduction of the conductivities measured on rough sandstone fracture face with 20/40 mesh sand at 0.10 lb/ft^2, compared with the conductivities measured on flat sandstone sample. This discrepancy can be partially attributed to the excessive proppant crushing on rough fracture faces due to the shear stress component acting on the proppants.

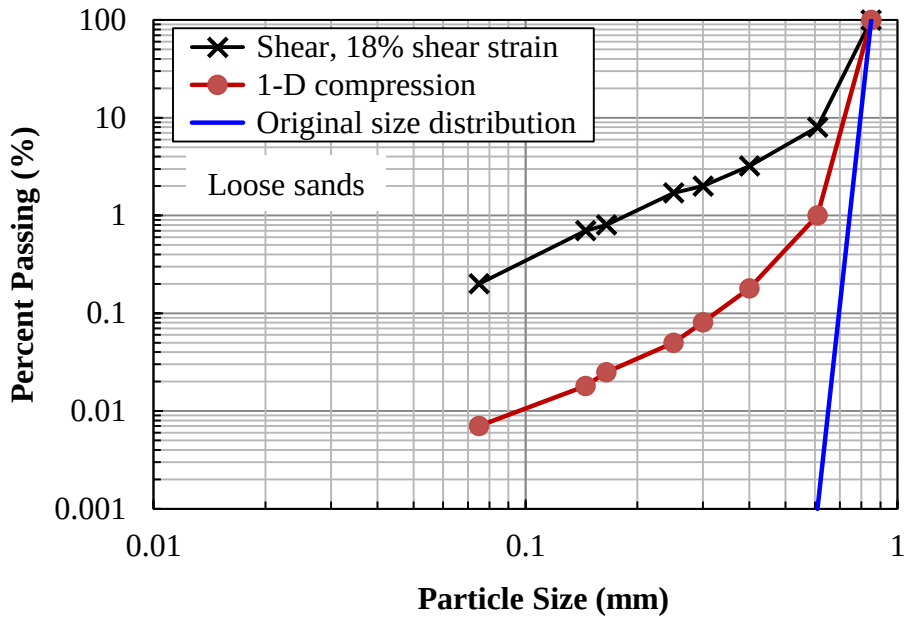

(a) Loose sands

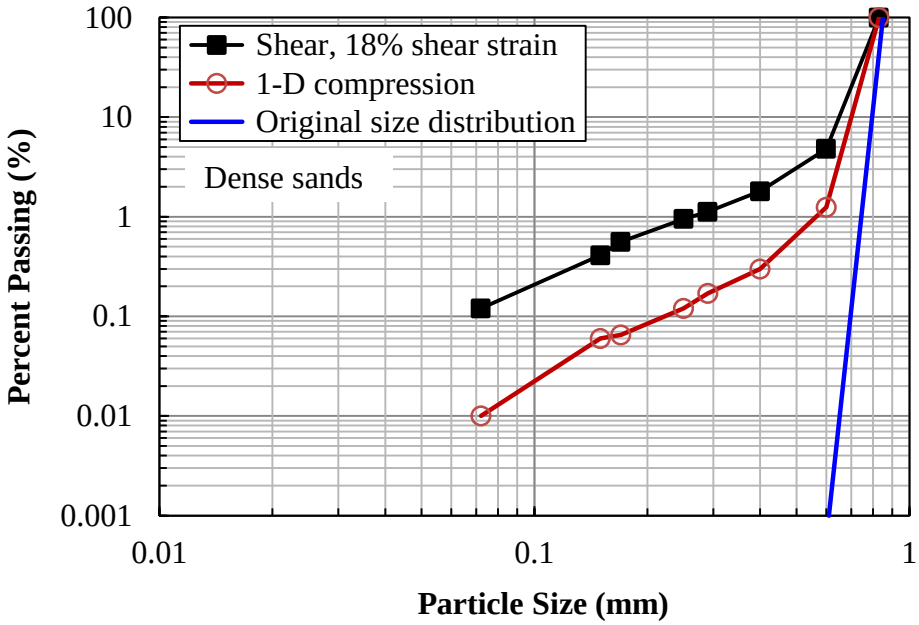

(b) Dense sands

Fig. 4.11–Post-crushing particle size distribution from 1-D compression tests to a maximum normal stress σ=2,000 psi and in simple shear tests loaded to σ=2,000 psi and subjected to a maximum shear strain γ =17.6% (i.e., 10°). Plots are modified from Guimaraes et al. (2006).

4.3 Fracture Permeability Calculation

It has been recognized that sand pack permeability is a strong function of sand grain size, packing, and sorting. Kozeny (1927) developed a capillary model that accounts for shape factor in actual rocks to calculate the permeability of porous media. Carman (1938) extended Kozeny's model by introducing a factor for grain surface area to represent the irregular surface of pores. One of the most popular and accurate correlations to calculate sand pack permeability was proposed by Berg (1970):

$$k = 5.1\times10^{-6}\phi^{5.1}d_{50}{}^{2}e^{-1.385\psi} \quad \text{..... (4-1)}$$

This model considers porosity of the porous media, grain particle size and sorting. However, one difficulty of applying this model to calculate propped fracture permeability is to determine the median grain size (d_{50}) and phi percentile deviation (ψ) of the crushed proppants, because proppant crushing is a dynamic process during the stress application. It is challenging to collect the low concentration proppants after experiment to do sieve analysis for particle size distribution. Even at higher concentration such as 0.20 lb/ft^2 where the total mass is 6.40 grams, post experiment sieve analysis brings too much error due to the loss of proppants during the experiment, because some proppants are embedded into the shale matrix and cannot be retrieved. The used proppants are always blended with shale flakes or particles and cannot be separated due to the similar size ranges. More importantly, we are interested in permeability at different stress levels. We cannot measure size distribution at each stress level without disturbing the proppant pack.

Therefore, a method to calculate particle size distribution at various stress levels is needed to determine fracture permeability.

4.4 Population Balance Equation to Predict Size Reduction

4.4.1 Introduction

A population balance equation describes the process of population changes of certain species as the net change of population is equal to the rate of concentration change. The net change of population is defined as the difference between species birth and death and they are usually functions of the entire population. So, population balance equations take the form of integro-differential equation. Depending on the form of the birth term and the death term, population balance equations can be solved analytically or numerically. The idea of population balance is widely applied in a variety of engineering areas, such as comminution of minerals, crystallization, polymerization in reactors and monodisperse colloidal suspensions (Ramkrishna 2000).

In petroleum engineering area, the idea of population balance was applied by Guin et al. (1971) and Hill (1978) to study the pore size evolution during matrix acid treatment. Sharma et al. (1986) also used this methodology to study formation permeability damage by fines migration and entrainment. Recently, Maqbool (2011) described the asphaltene precipitation process by applying population balance equations and solved the series of equations numerically. The population balance in size reduction can be illustrated by **Fig. 4.12.**

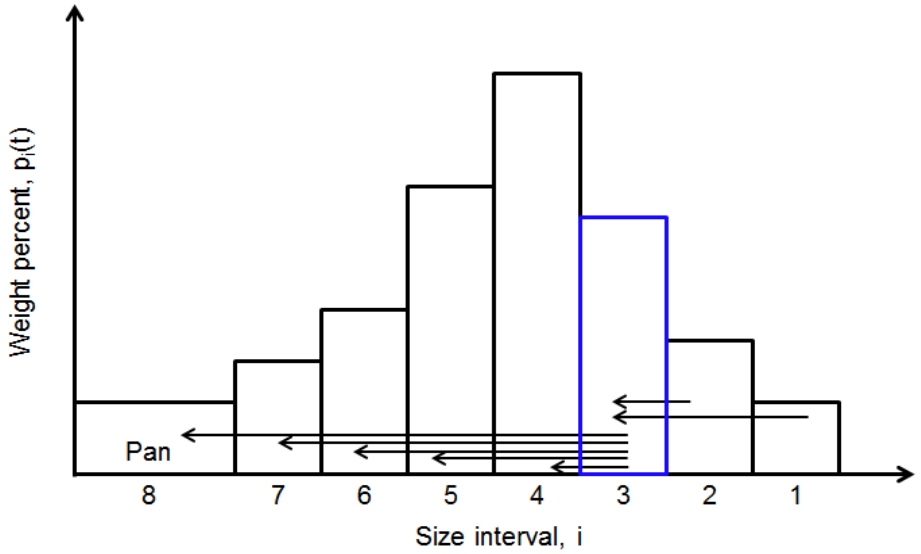

Fig. 4.12–Population balance for size reduction.

Take size interval 3 for instance. Particles of this size range are crushed into smaller sizes. Meanwhile, this interval also receives particles crushed from larger sizes. So, a population balance equation for size reduction can be described as,

Population density change per unit application of stress =

Amount of particles crushed from this size interval +

Amount of particles crushed from larger sizes that this size interval receives.

4.4.2 Selection Function

In crushing tests, particles usually have a size range and the stress status for the grains is different depending on size, location, number of contacts, and their mechanical properties. Therefore, the chance for each particle to be crushed is not equal. The function to describe the mass fraction of the particles of a specific size to be crushed per unit stress is called the selection function or specific rate of breakage.

For example, the 40/70 mesh sand at 0.1 lb/ft^2 contains 0.973 gram particles at 50-60 mesh size range at zero closure stress. We apply the closure stress and crush 0.001 gram particles of this size range. Then, the selection function would be $\frac{0.001\ \text{g}}{0.973\ \text{g}}$.

Assume $P(x,\sigma)$ is the cumulative mass fraction of the proppants smaller than size x at stress σ, the selection function, $S(x)$, can be mathematically expressed as (Gardner and Austin 1962),

$$S(x) = -\left[\frac{\frac{\partial}{\partial\sigma}\left[\frac{\partial P(x,\sigma)}{\partial x}\right]}{\frac{\partial P(x,\sigma)}{\partial x}}\right] \quad \text{..... (4-2)}$$

Gardner and Austin (1962) experimentally determined the selection function by radioactive tracer techniques. They irradiated the samples for one hour at the maximum thermal neutron flux of the Pennsylvania State University Reactor. The amount of radioactivity in each size fraction was determined by gross counting at every loading cycle with size distributions determined. From the experiments, they plotted the fractional weight of the broken particles versus particle size and determined the selection function (**Fig. 4.13**).

In our study, we follow the expression of the selection function suggested by Austin (1999),

$$S(x) = a_1 x^{a_2} \quad \text{..... (4-3)}$$

Where a_1 and a_2 are the empirical coefficients and can be determined by experiment. From Fig. 4.13, a_1 = 3E-4, a_2 =0.565.

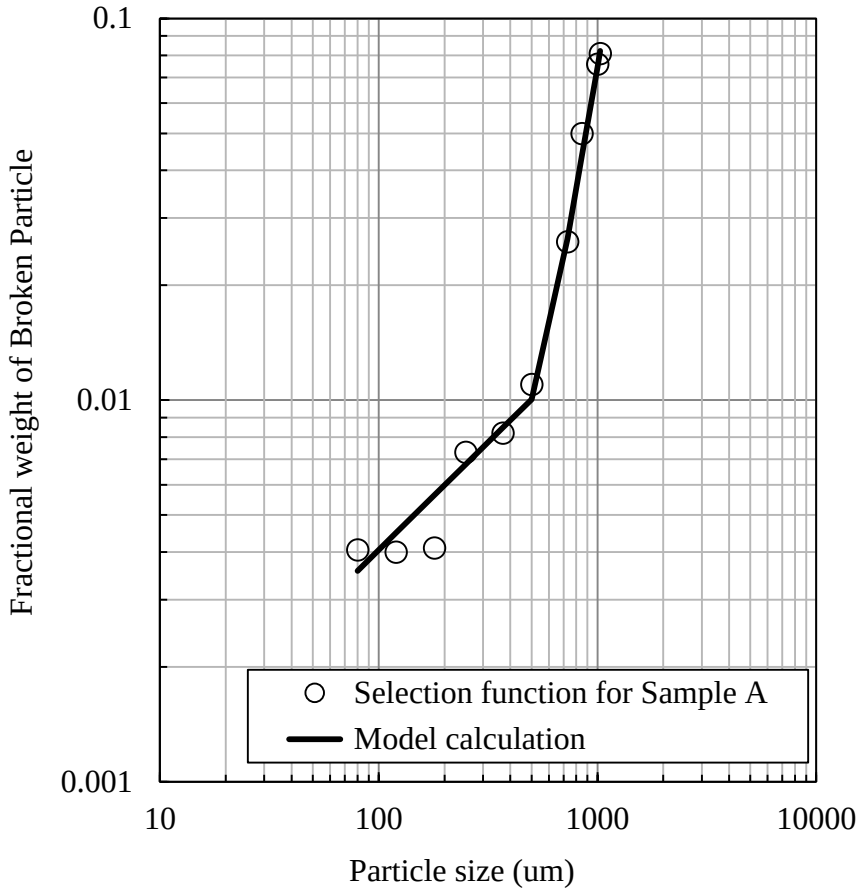

Fig. 4.13–Determination of the selection function by Gardner and Austin (1962).

4.4.3 Breakage Function

For particles that are crushed from interval i, some of them fall into the size range of i+1, while others might be in interval i+2 or i+5. So, another function is needed to characterize the amount of particles falling into interval j from a larger size interval i. This function is called the breakage function or distribution function.

Again, let us use 40/70 mesh sand data as an example. Within the 0.001 gram crushed particles, half of them fall into the range of 60-70 mesh. Then the breakage

function for this size interval should be 0.0005. The designation B is used for breakage function. Mathematically, B is defined as,

$$B(y,x) = -\frac{\dfrac{\partial P(x,\sigma)}{\partial \sigma}}{\dfrac{\partial}{\partial \sigma}\left[\dfrac{\partial P(y,\sigma)}{\partial y}\right]}, 0 \le x \le y \quad \text{..... (4-4)}$$

The breakage function was experimentally determined by Gardner and Austin (1962) using the same radioactive tracer technology as the selection function (**Fig. 4.14**). Various models have been proposed to express the breakage function, including the work by Broadbent et al. (1956), Reid (1965), Kapur (1972) and Austin (1999). Here we use the modified Austin model to match the experimental data to generate the breakage function. The model is expressed as,

$$B(y,x) = a_3\left(\frac{x}{y}\right)^{a_4} + (1-a_3)\left(\frac{x}{y}\right)^{a_5}, 0 \le x \le y \quad \text{..... (4-5)}$$

Where a_3 , a_4 and a_5 are the empirical coefficients and are determined by experiment. From Fig. 4.14, a_3 = 0.65, a_4 =1.25, a_5 =4.5.

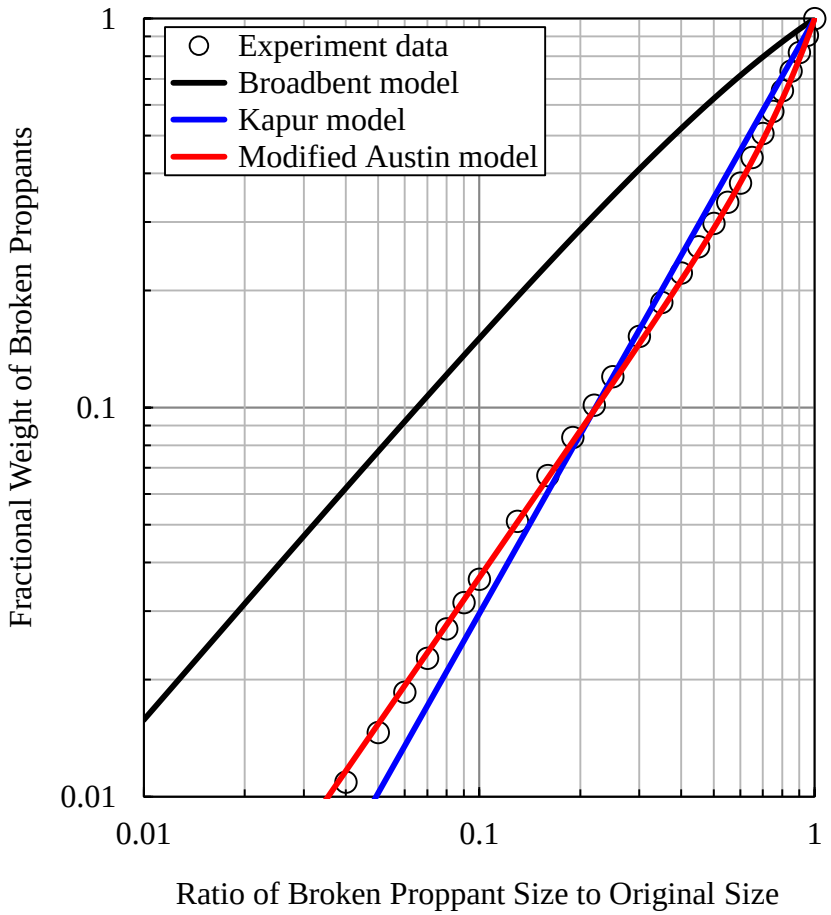

Fig. 4.14–Determination of the breakage function. Experiment data are from Gardner and Austin (1962).

4.4.4 Mathematical Model for the Process of Size Reduction

The first rigorous mathematical model for size reduction based on population balance was derived by Bass (1954). But more popular are the mathematical expressions proposed by Gardner and Austin (1962) and Reid (1965). In this study, we follow the procedures recommended by Gardner and Austin (1962) to derive the mathematical model.

It is assumed that: (1) during the stress application, proppants can only be crushed into smaller sizes and there is no feed of particles into the proppant pack; (2) the selection

function and the breakage function as stated in the previous sections are valid in the primary breakage of particles at size y to a differential size y+dy. The weight percent of proppants smaller than size x at closure stress σ, $P(x,\sigma)$, is equal to the sum of the weight percent of proppants at size x originally and the weight percent of proppants crushed to size x from larger sizes due to the stress increment $d\sigma$.

For a differential size increment from y to y+dy, the weight percent of the amount of crushed proppants is,

$$m_p = \left[\frac{\partial P(y,\sigma)}{\partial y}\right] dy, x \le y \le x_{\max} \quad \text{..... (4-6)}$$

According to the definition of the selection function, it can be expressed as,

$$S(y) = \frac{\left[\frac{dm_p}{d\sigma}\right]}{m_p} = \frac{\frac{dm_p}{d\sigma}}{\frac{\partial P(y,\sigma)}{\partial y} dy} \quad \text{..... (4-7)}$$

Rearrange Eq. 4-7, we can get,

$$dm_p = S(y)\frac{\partial P(y,\sigma)}{\partial y} dy d\sigma \quad \text{..... (4-8)}$$

We use the consistent nomenclature for breakage function as $B(y,x)$. The amount of proppants crushed from dm_p into size x can be defined as,

$$m_{p,x} = B(y,x)S(y)\frac{\partial P(y,\sigma)}{\partial y} dy d\sigma \quad \text{..... (4-9)}$$

Assume the stress interval $[0,\sigma_{\max}]$ is equally spaced. The weight percent of proppants at size x in stress interval n can be derived as,

$$P(x,\sigma_n) = P(x,\sigma_{n-1}) + B(y,x)S(y)\frac{\partial P(y,\sigma)}{\partial y}dyd\sigma \quad \text{..... (4-10)}$$

Eq. 4-10 can be mathematically mutated as,

$$P(x,\sigma) = P(x,\sigma_0) + \int_0^{\sigma_n}\int_x^{x_{\max}} B(y,x)S(y)\frac{\partial P(y,\sigma)}{\partial y}dyd\sigma \quad \text{..... (4-11)}$$

Rearrange Eq. 4-11 and partially differentiate it with respect to σ,

$$\frac{\partial[P(x,\sigma)]}{\partial\sigma} = \int_x^{x_{\max}} B(y,x)S(y)\frac{\partial P(y,\sigma)}{\partial y}dy \quad \text{..... (4-12)}$$

Differentiate Eq. 4-12 with respect to size x,

$$\frac{\partial}{\partial x}\left[\frac{\partial P(x,\sigma)}{\partial\sigma}\right] = -S(x)\frac{\partial P(x,\sigma)}{\partial x} + \int_{y=x}^{x_{\max}} \frac{\partial B(y,x)}{\partial x}\frac{\partial P(y,\sigma)}{\partial y}S(y)dy \quad \text{..... (4-13)}$$

Eq. 4-13 is the integro-differential population balance equation for size reduction. The population balance equation for proppant crushing satisfies the initial and the boundary conditions below.

$$P(x,\sigma)\big|_{\sigma=0} = P(x,0) \quad \text{..... (4-14)}$$

$$P(x,\sigma)\big|_{x=x_{\max}} = 1 \quad \text{..... (4-15)}$$

Where $P(x,0)$ is the initial proppant size distribution which can be acquired from sieve analysis. The boundary condition Eq. 4-15 means that the cumulative weight fraction of proppant smaller than the maximum size is equal to 1.

4.4.5 Solution of the Population Balance Equation

Solution of the integro-differential population balance equation has been well presented by Ramkrishna (2000). Generally, it can be solved analytically by assuming simple linear

selection and breakage functions (Reid 1965; King 1972; Peterson 1986; Campbell et al. 1994). A numerical solution scheme was proposed by Gardner and Austin (1962) and improved by Lucas and Luke (1983) as well as Maqbool (2011). Mishra (1999) solved the equation using the Monte-Carlo method.

This study solves the population balance equation numerically using a finite difference method. The discretized equation is included in **Appendix C**. The algorithm is illustrated by the flow chart in **Fig. 4.15**.

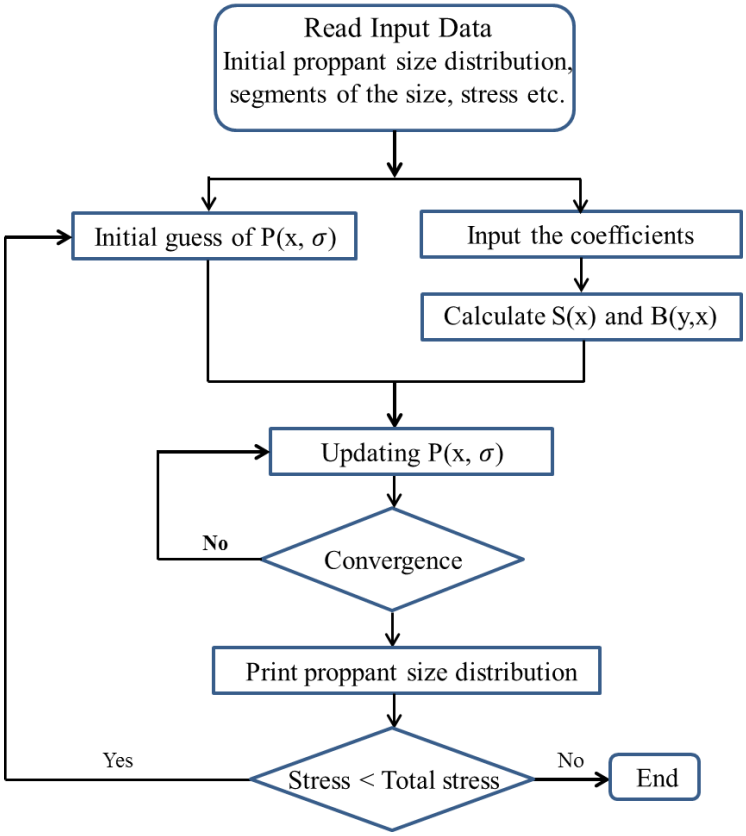

Fig. 4.15–Algorithm to solve the population balance equation.

4.4.6 Validation of the Solution

Solution to the integro-differential equation is validated by matching the computed proppant size distribution with the measured data. Two sets of sieve analysis data are provided to match the solutions.

The first set of data comes from over 10 experiments with 0.06 lb/ft^2 and 0.10 lb/ft^2 concentration. The sieve analysis requires at least 30 grams of sands to account for the mass loss during shaking. We divided the 30 grams of sands into various portions for different experiments. Proppants were collected after all the experiment and were used for the post experiment sieve analysis. The measured size distribution and modeled size distribution at various closure stresses are plotted in **Fig. 4.16**.

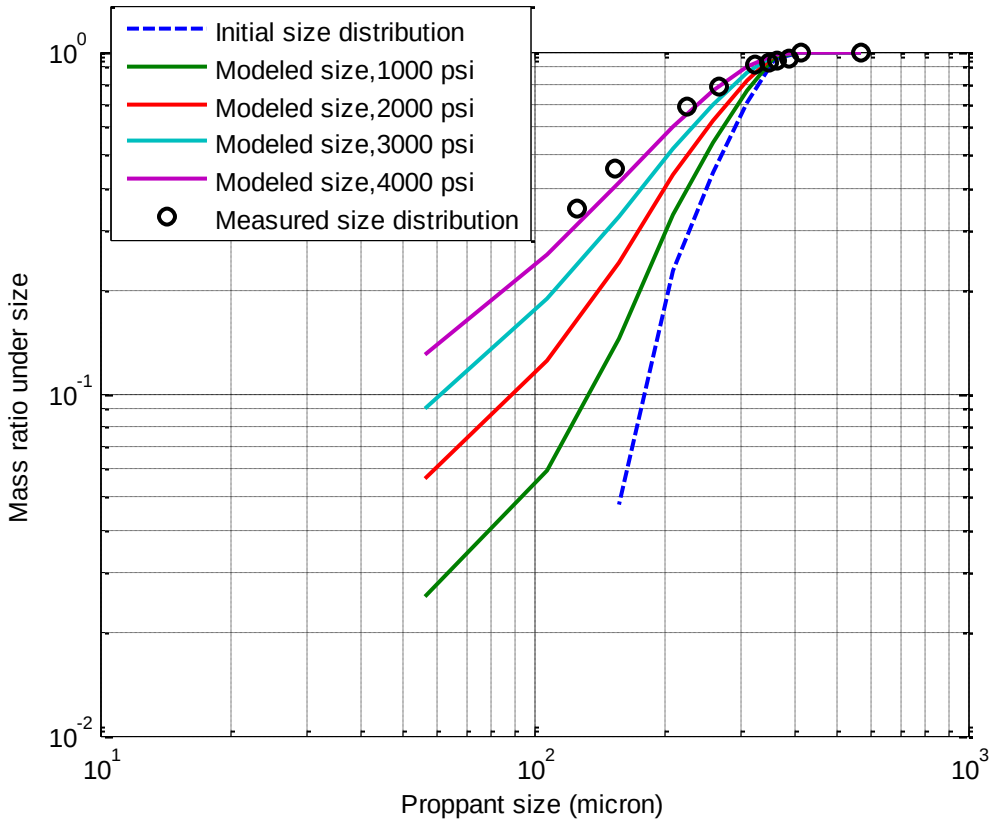

Fig. 4.16–Measured and modeled proppant size distribution (Dataset 1).

We can see that at the smaller size range, the model shows an underpredicted size distribution compared with the measured values. This is probably caused by the shale particles mixed with the proppants after the experiments. The shale particles collected from the fracture surface has similar sizes as the crushed sand grains and cannot be separated. Other than that, the model predicts a reasonable proppant size distribution.

The second dataset is collected from the published literature by Fredd et al. (2001). In their work, they measured the proppant size distribution after the conductivity experiment at 7,000 psi closure stress. The measured data and the modeled results are in **Fig. 4.17**.

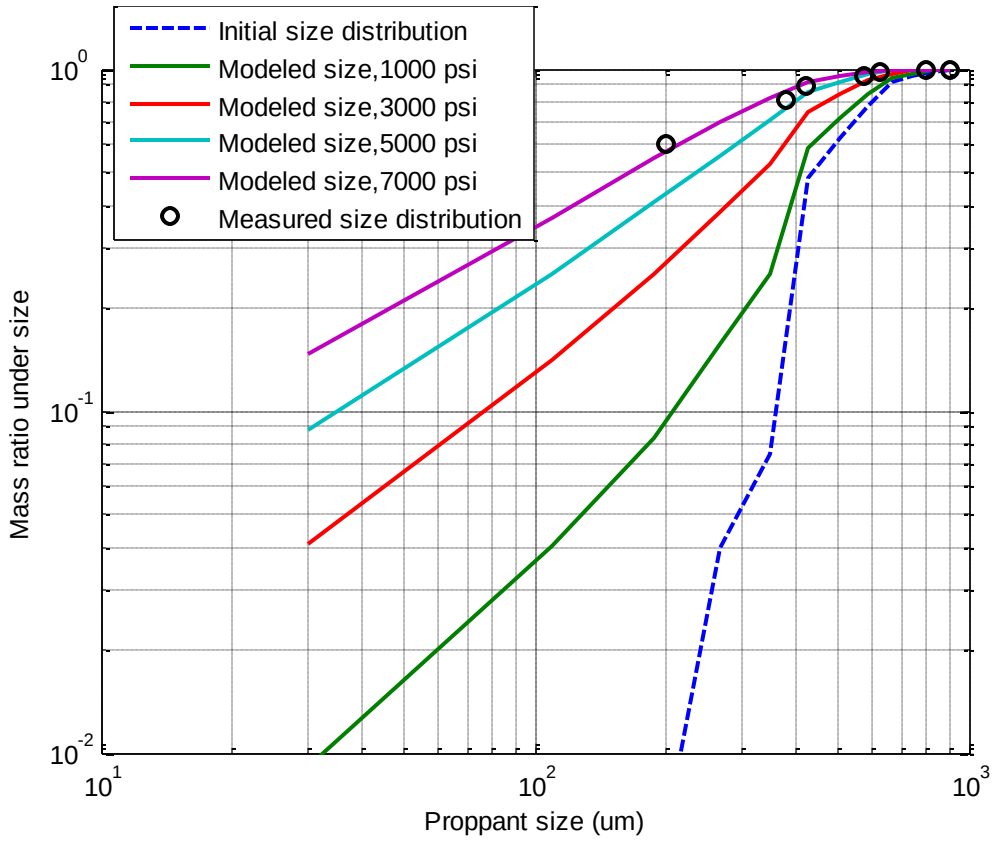

Fig. 4.17–Measured and modeled proppant size distribution (Dataset 2, Fredd et al. 2001).

The linear size distribution at higher closure stresses on the log-log plot indicates the fractal distribution of grain sizes (McDowell and Bolton 1998; Lobo-Guerrero and Vallejo 2005). It also honors the assumption of one dimensional loading pattern with no lateral strain (Guimaraes et al. 2007).

4.5 Fracture Width Calculation

Width reduction happens due to proppant rearrangement, proppant embedment, proppant crushing, gel filter cake, and so on (Palisch et al. 2007). In this study, proppants are manually placed, so there is no gel damage. We mainly discuss the width reductions caused by proppant grain rearrangement and embedment.

4.5.1 Proppant Rearrangement

Loose proppant grains with a wide size range are loaded on the fracture surface. After the stress is applied, grain rearrangement occurs due to the inter-granular frictional slippage and pore collapse, as illustrated in **Fig. 4.18**.

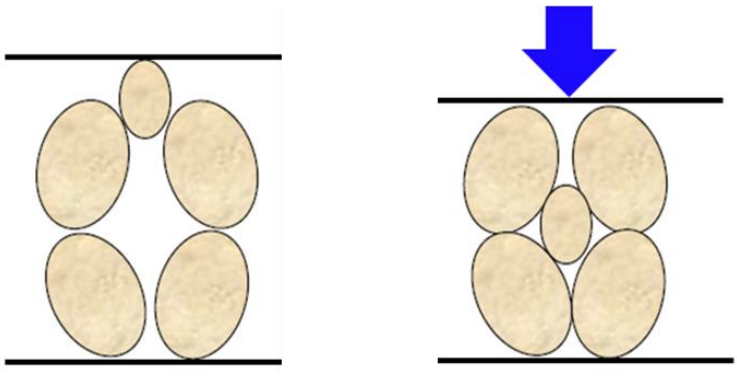

Fig. 4.18–Width reduction by proppant grain rearrangement caused by inter-granular frictional slippage and pore collapse.

Define the initial proppant pack void ratio e_0 as the ratio of the pore volume to proppant grain volume at zero closure stress. The fraction of void ratio change is equal to the fraction of width change (**Fig. 4.19**) assuming:

(1) The solid particles are incompressible and embedment is negligible during this phase, so that the change in total volume is only related to the change in pore volume.

(2) The consolidation is one dimensional in the width direction and the strain in the flow direction is negligible, or simply assuming the cross sectional area of the proppant pack in the width direction is constant.

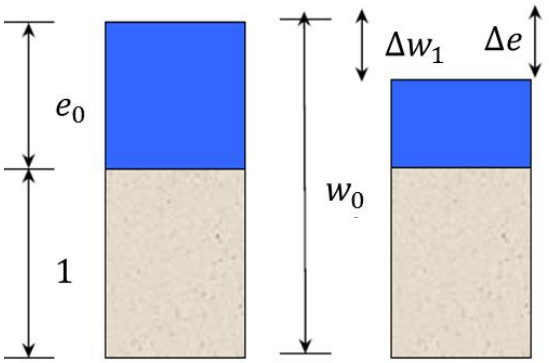

Fig. 4.19–Void volume reduction due to the grain rearrangement.

Assume an initial proppant pack width w_0 **,** width reduction by the grain rearrangement Δw_1, initial proppant pack void ratio e_0, void ratio reduction Δe. Then,

$$\frac{\Delta w_1}{w_0} = \frac{\Delta e}{1+e_0} \quad \text{..... (4-16)}$$

Initial porosity is,

$$\phi_0 = \frac{e_0}{1+e_0} \quad \text{..... (4-17)}$$

So,

$$\Delta w_1 = w_0(\phi_0 - \phi_1)(1-\phi_0) \quad \text{..... (4-18)}$$

Assume that the initial porosity is 35%. At 4,000 psi closure stress, porosity decreases to 25%. Then,

$$\Delta w_1 = w_0(35\% - 25\%)(1-35\%) = 0.065 w_0 \quad \text{..... (4-19)}$$

4.5.2 Proppant Embedment

Proppant embedment depth is determined by laboratory measurements and the width loss due to embedment is shown in **Eq. 4-20** (Palisch et al. 2010). This relation has been used for a variety of sandstone fracture width calculations.

$$\Delta w_E = \frac{2.5 d_p}{(1+\frac{4000 \times E}{\sigma})^{1.5}} \quad \text{..... (4-20)}$$

Fig. 4.20 shows the embedment depth Δw_E as functions of the grain diameter d_p, Young's modulus E (MMpsi)) and the closure stress σ (psi). The embedment depth has the consistent unit as the proppant grain diameter. At 4,000 psi, the ratio of the embedment depth to the grain diameter is about 0.20 assuming the Young's modulus is 4 MMpsi.

4.6 New Method to Predict Propped Fracture Conductivity

In this section, we propose a new method to predict propped fracture conductivity by modifying the Berg correlation (1970) for calculating permeability integrated with the

population balance equation for size reduction. In this method, the proppant size, packing, sorting, crushing, grain rearrangement and grain embedment are taken into account.

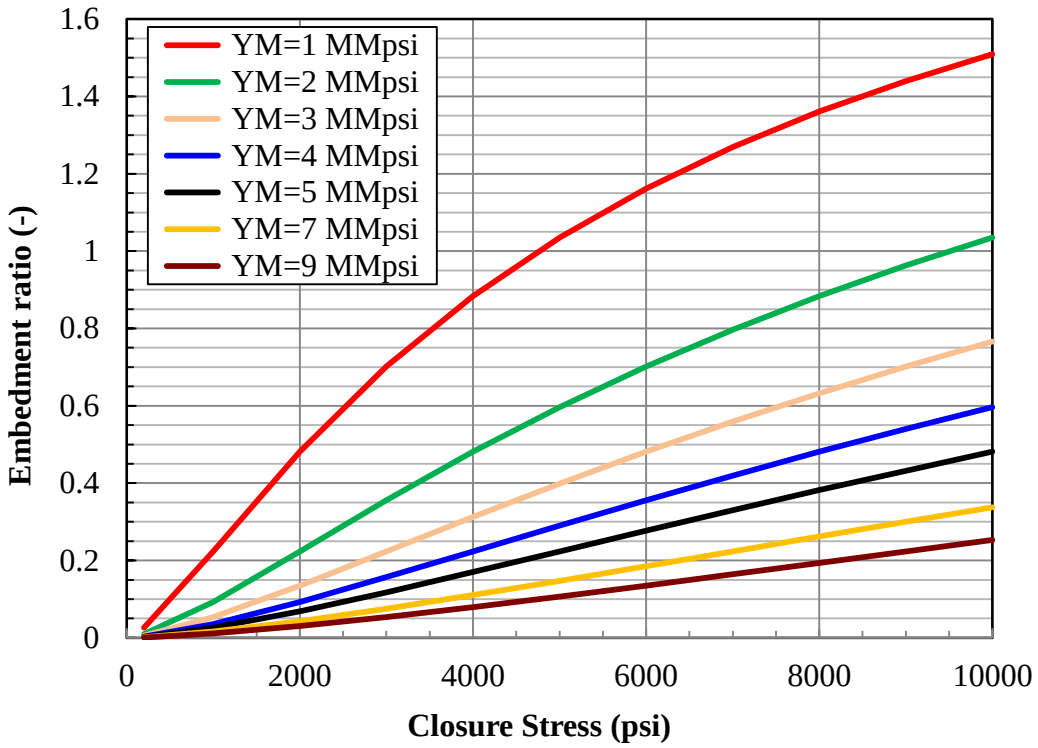

Fig. 4.20–The ratio of the proppant embedment depth to grain diameter correlated with closure stress and Young's modulus.

We first solve the population balance equation for the proppant size distribution at various stresses. The parameters for the Berg's correlation (1970) to calculate the fracture permeability can be read from the proppant size distribution (**Fig. 4.21**). The initial porosity and porosity change for clean sands studied by Karner et al. (2004) indicate that, in the Barnett Shale reservoir conditions, the porosity variation in propped fracture is within 3% (**Fig. 4.22**). So the average porosity is used in the Berg correlation.

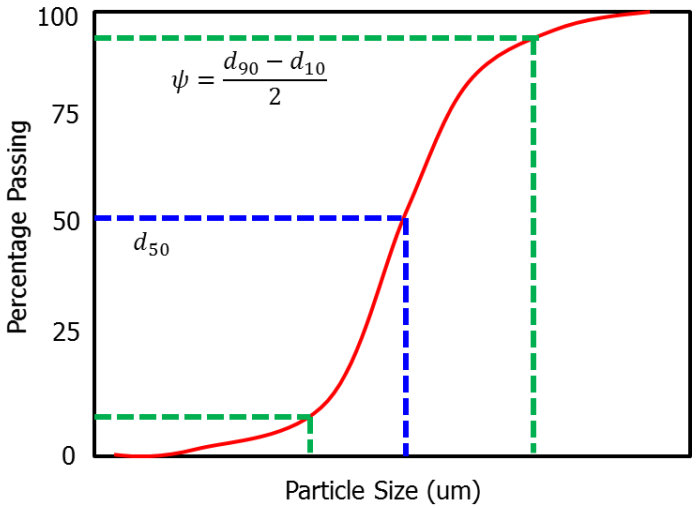

Fig. 4.21–Median size and phi percentile deviation of proppant grain from the proppant size distribution.

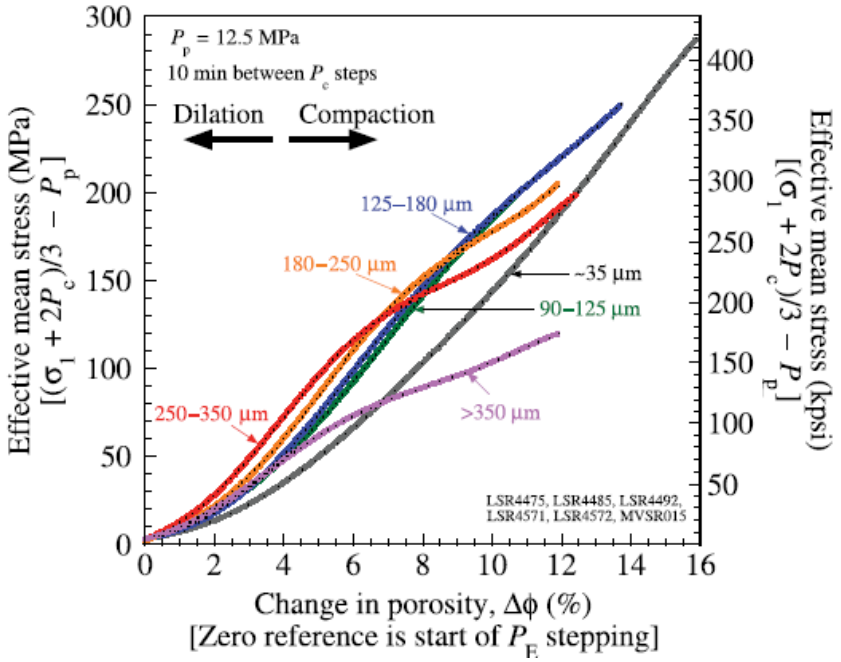

Fig. 4.22–Porosity of sand packs at various stresses (Karner et al., 2004).

The initial fracture widths for various concentrations were measured in lab. We particularly measured the proppant pack thickness at multiple surface valleys indicated

by the surface profilometry, because fractures tend to close on the thicker sand packs at the surface valleys. The initial fracture widths are summarized in **Table 4.2**.

Table 4.2–Measured fracture widths at the fracture surface valleys of 40/70 mesh and 30/50 mesh sands at various concentrations.

Proppant mesh size	Proppant concentration (lb/ft^2)	Initial width (inch)	Initial width (mm)
40/70	0.06	0.024	0.610
40/70	0.10	0.037	0.940
40/70	0.20	0.066	1.676
30/50	0.10	0.035	0.889

As Kamenov (2013) has pointed out that due to the surface asperity, proppants tend to collect at the valleys of the fracture surface. At the same concentration, the initial propped width of the rough fracture is larger than the fracture width where proppants are evenly distributed due to the thicker sand collections at the surface valleys (**Fig. 4.23**). The conductivity of the rough fracture would also be higher than tightly packed fracture because of the void spaces above the proppant pack. At lower closure stress, the proppant grains rearrange and accommodate themselves to overcome the stress. During this phase, fracture width decreases and the fracture still closes on the thick sand pack at the surface valleys. At higher closure stress where proppant embedment happens and point loading effect starts to occur, the sand pack at the valleys experiences severe width reduction. Meanwhile, the rock creeps in response to the higher stress causing the void space above the proppants to close. During this phase, the pressure drop across the fracture at certain flow rate is close to the pressure drop across the fracture where proppants are evenly placed initially.

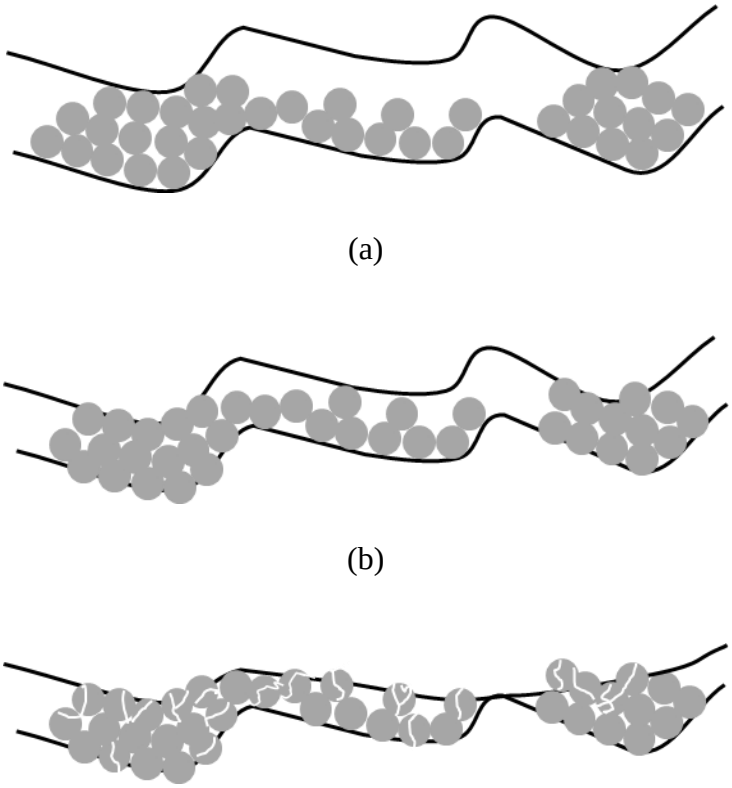

Fig. 4.23–Proppant distribution on rough shale fracture surface: (a) initial proppant pack with large void space above the proppants; (b) proppant grain rearrangement during the application of closure stress; (c) at high closure stress, proppants are crushed and the rock creeps.

To account for the extra flow path caused by the open spaces above the sand pack, the Berg model is modified to better predict proppant pack permeability as,

$$k = 283.13 d_{50}^{\ 2} e^{-1.385\psi} \sigma^{-0.541} \quad \text{..... (4-21)}$$

Where,

$$\psi = \frac{d_{90} - d_{10}}{2} \quad \text{..... (4-22)}$$

The unit of the closure stress σ is psi. With this modified model, proppant pack permeability at low concentrations can be predicted considering the uneven proppant distribution. The flowchart to calculate the propped fracture conductivity is shown in Fig. 1.5.

Fig. 4.24 and Fig. 4.25 show the predicted fracture conductivities matching with the measured conductivities of 40/70 mesh and 30/50 mesh sands. In the calculations, the initial porosity is 0.35. Young's Modulus for the Barnett Shale outcrop sample is 1.6 $\times 10^6$ psi. Initial fracture widths can be found in Table 4.2.

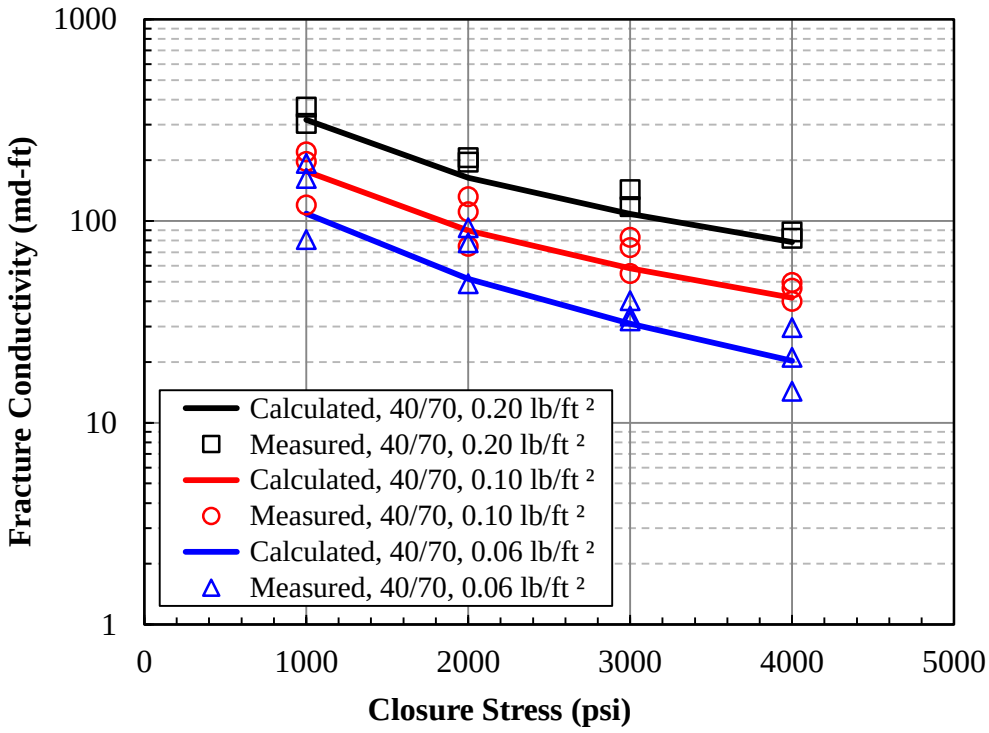

Fig. 4.24–Calculated and measured fracture conductivity of 40/70 mesh sands at various concentrations.

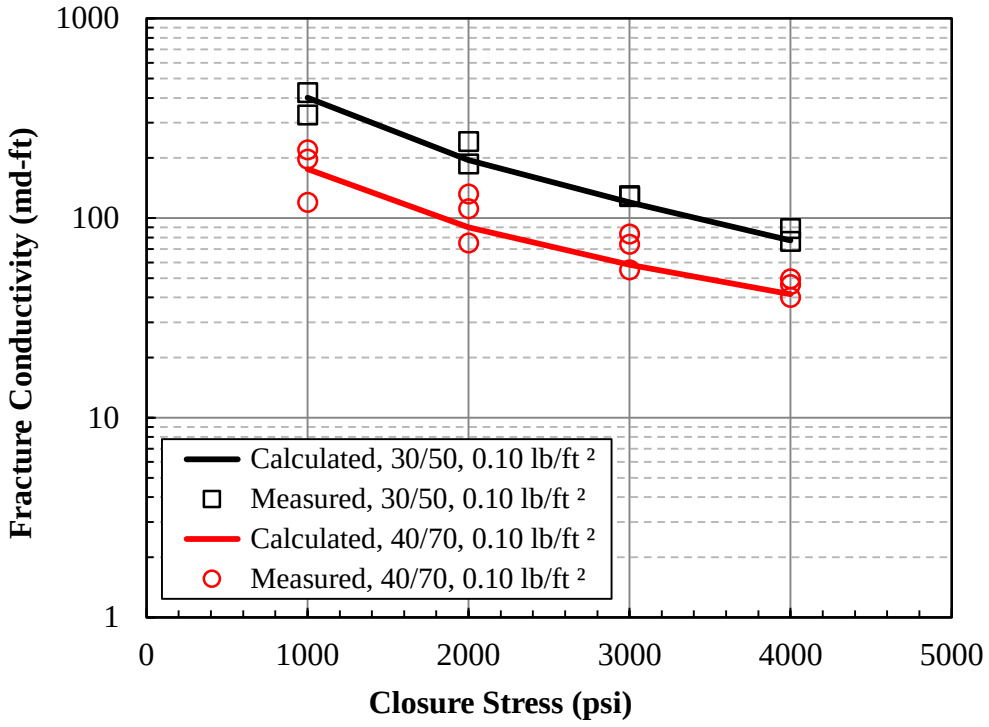

Fig. 4.25–Calculated and measured fracture conductivity of 40/70 mesh sands and 30/50 mesh sands at 0.10 lb/ft ².

4.7 Chapter Summary

In this chapter, we first discussed the uncertainties of propped fracture conductivity measurement and methods for improvement. Then we presented the measured propped fracture conductivity of 100 mesh, 40/70 mesh, and 30/50 mesh sands at low concentrations on different types of fractures. The crushing of partial monolayer sands at ultra-low concentration (0.03 lb/ft ²) and its effect on conductivity were discussed and supported by the sand grain shear experiments. Finally we proposed a new method to predict propped fracture conductivity based on the population balance equation. Results predicted by the new method can reasonably match with the laboratory data.

5 FRACTURE CONDUCTIVITY DAMAGE BY WATER IN SHALE FORMATIONS

This chapter investigates the conductivity damage by water and its mechanisms. Conductivities are measured by both dry nitrogen and water (fresh water, brine, flowback water). Then imaging techniques are utilized to analyze the fracture surface features after water flow. The damage mechanisms and each of the factors are investigated by comparing with the control experiments. Finally, the fracture conductivity correlation considering water damage is proposed.

5.1 Introduction

The interaction between shale and water has been studied in the areas of drilling engineering, formation damage, water flooding and enhanced oil recovery. Clay mineral damages formation flow capacities by two ways: clay swelling and fines migration. To study how water sensitivity of shale impacts fracture conductivity, we need to understand the structure of clay minerals in shale.

Two structural units form the atomic lattices for most clay minerals (Grim 1968). In the first unit, aluminum, iron or magnesium atoms are embedded in the octahedral coordination and they are equidistant from six oxygens or hydroxyls (**Fig. 5.1**). The second unit consists of silica tetrahedrons (**Fig. 5.2**). In this structure, the silicon atom is equidistant from four oxygens, or hydroxyls. Illite, for example, has a basic structure consisting of two silica tetrahedral sheets bounding a gibbsite or brucite sheet (**Fig. 5.3**).

The sensitivity of clay to water depends on the type and amount of exchangeable cations and the layered structure. Illite has the interlayered sheet structure and combines the worst features of the dispersible and the swellable clays (Mungan 1989).

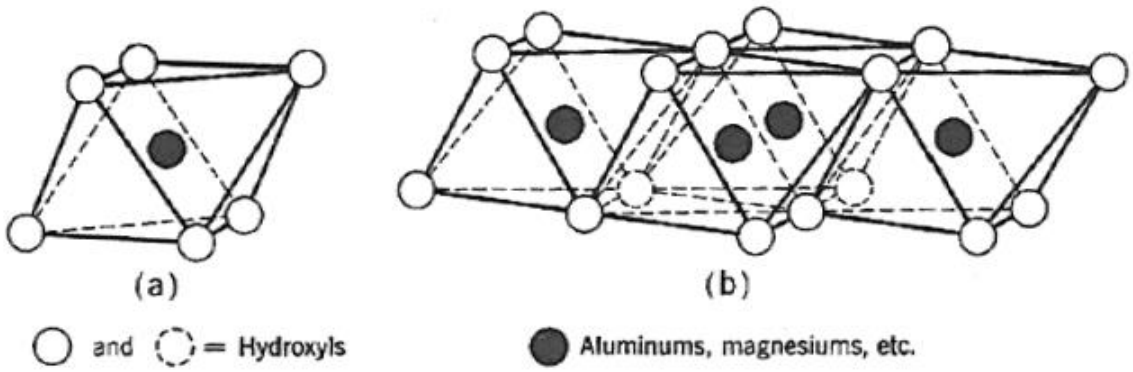

Fig. 5.1–Diagram of the first clay structural unit: (a) a single octahedral unit; (b) the sheet structure of the octahedral units (Grim 1968).

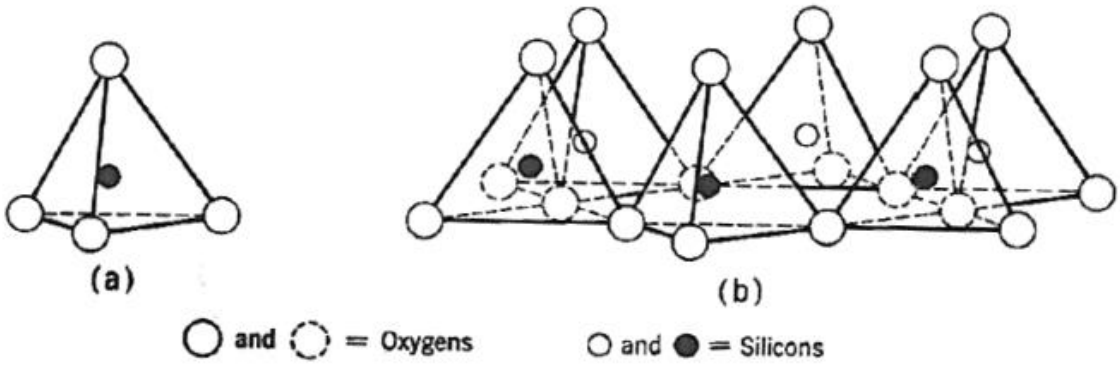

Fig. 5.2–Diagram of the second clay structural unit: (a) a single silica tetrahedron; (b) the sheet structure of the silica tetrahedrons arranged in a hexagonal network (Grim 1968).

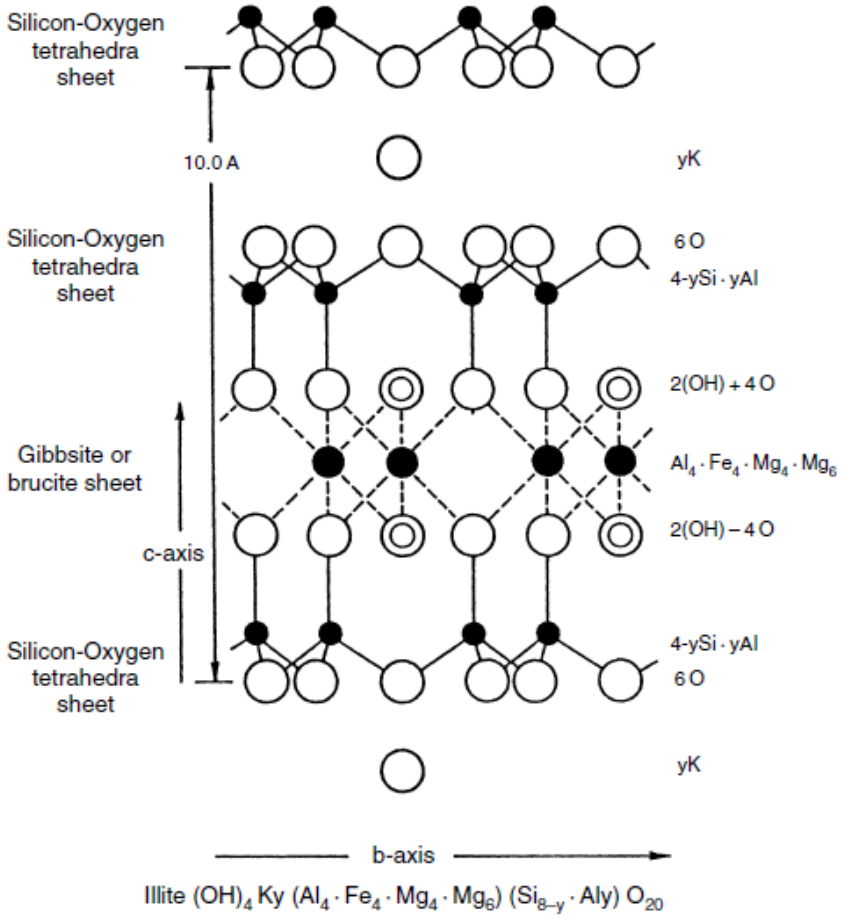

Fig. 5.3–Basic structure of illite (Civan 2007).

5.2 Physical Processes During the Experiments

The water experiment starts from single phase gas flow, followed by the displacement of gas by water. Finally, water is removed by flowing gas. The goal of the liquid flow and the second gas flow is to reach steady state to calculate the fracture conductivity.

5.2.1 Displacement of Gas by Water in the Fracture

The mechanics of two phase displacement can be interpreted by the concept of mobility, which is defined as,

$$\lambda = \frac{k_m k_r}{\mu} \quad \text{..... (5-1)}$$

Where λ is the mobility; k_m is the matrix permeability; k_r is the relative permeability; and μ is the viscosity.

The mobility ratio M is defined as,

$$M = \frac{\lambda_{displacing}}{\lambda_{displaced}} = \frac{k_{r\alpha}/\mu_\alpha}{k_{r\beta}/\mu_\beta} \quad \text{..... (5-2)}$$

In the favorable case where $M \leq 1$, one phase displaces the other phase in a "piston" manner (**Fig. 5.4)**.

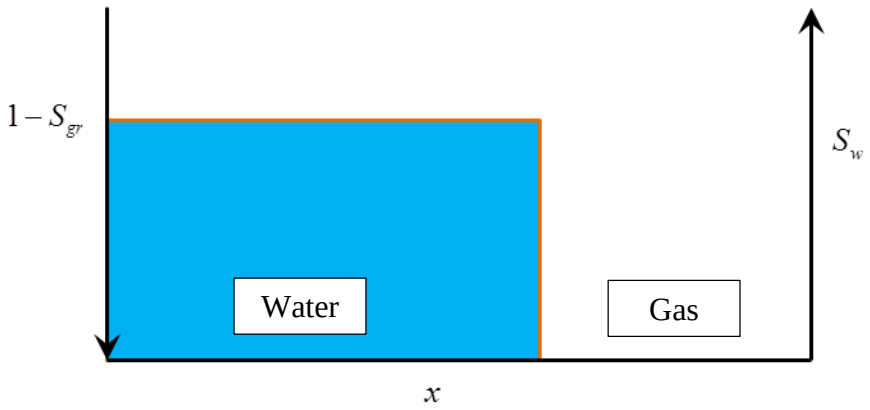

Fig. 5.4–Ideal "piston-like" displacement of gas by water.

In water-nitrogen two phase flow system with water as the displacing phase, the mobility ratio is much smaller than 1 because the viscosity of water is about 50 times larger than the viscosity of nitrogen. However, due to the random distribution of fracture surface asperities, the fracture does not have a uniform width across the sample. The thicker proppant pack has higher flow capacity while the unpropped faces tend to close under elevated stresses. **Fig. 5.5** shows the void spaces before fracture closure. The red

and yellow regions indicate the high conductivity channels favorable to fluid flow. This means water sweeps the fracture face non-uniformly and the actual saturation profile would look like **Fig. 5.6**.

The non-ideal displacement explains the pressure response in the fracture under constant flow rate, as shown in **Fig. 5.7**. In this experiment, the differential pressure keeps dropping after the water breaks through because the average water saturation inside the fracture increases, resulting in larger water phase permeability. Steady state flow is reached when the pressure stabilizes at the constant flow rate.

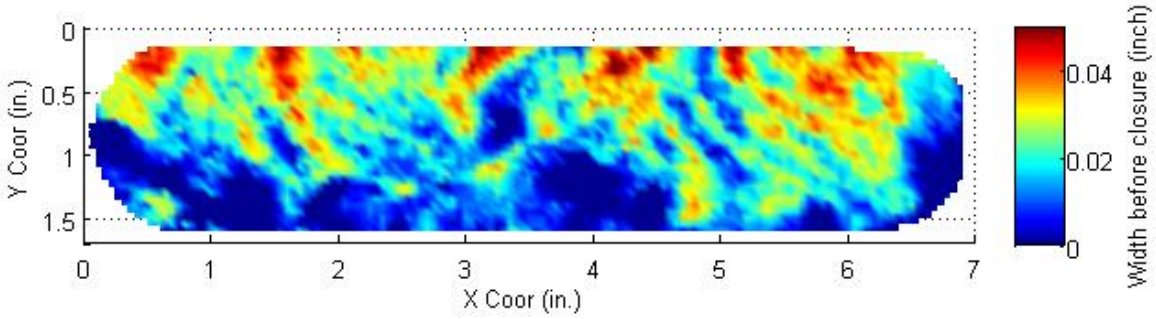

Fig. 5.5–Initial fracture width before fracture closure.

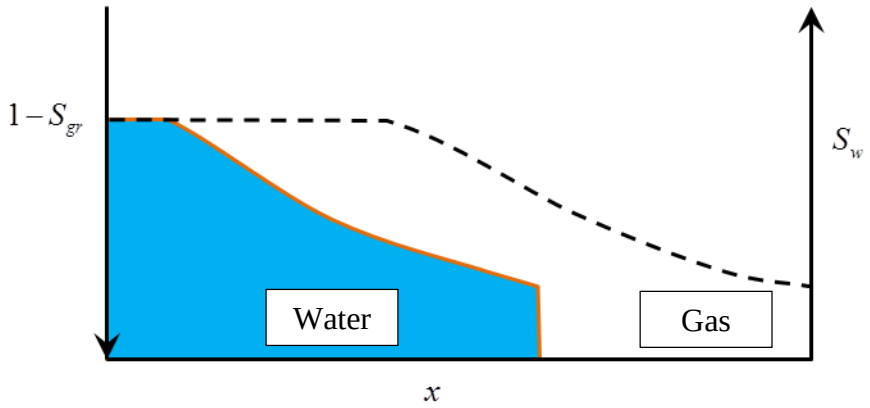

Fig. 5.6–Non-ideal displacement in the fracture due to non-uniform flow capacity across the sample.

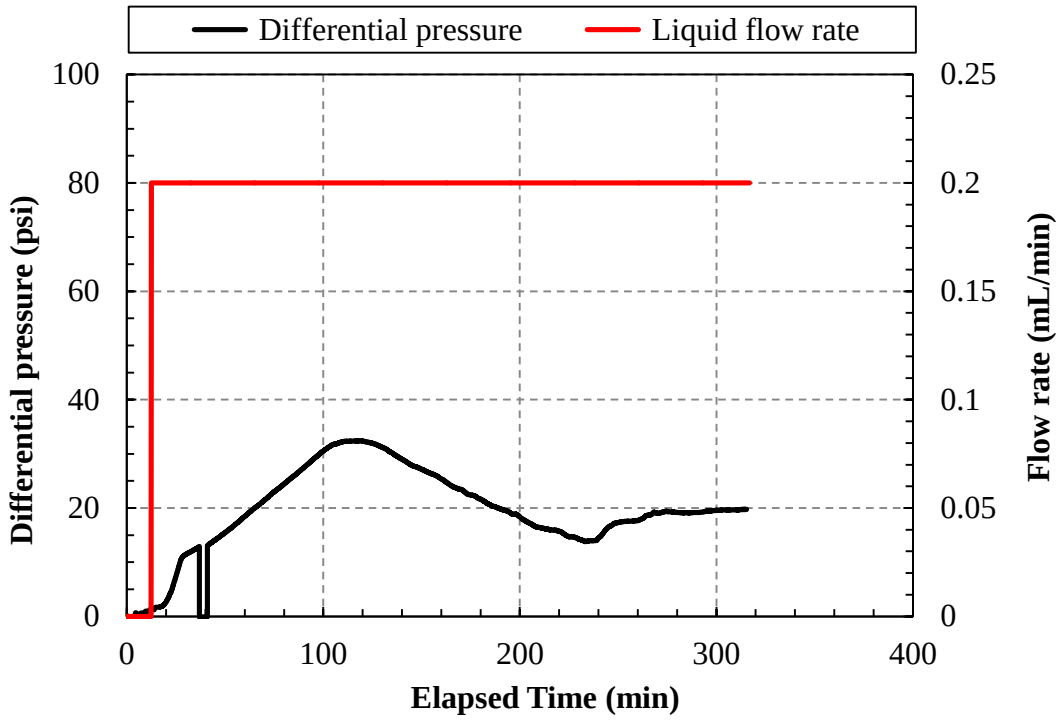

Fig. 5.7–Differential pressure under the constant flow rate of 0.2 mL/min during the displacement of gas by water. 40/70 mesh sands at 0.10 lb/ft ²were placed.

5.2.2 Removal of Water by Gas in the Fracture

Displacement of water by gas is considered as an unfavorable process because the mobility ratio is larger than 1. As stated in the previous section, gas prefers to flow through the high conductivity paths and to bypass the low conductivity regions that are still saturated by water. Previous studies (Mahadevan and Sharma 2003; Zhang et al. 2013b) show that the displacement dominated regime and the evaporation dominated regime occur during the removal of water from porous media. They also believed that evaporative cleaning of waterblocks is the dominant mechanism of water removal in gas wells.

Fig. 5.8 shows an example of the recorded pressure and flow rate during an experiment. It can be seen that significant pressure drop at 40 minutes indicates that gas

breaks through the water phase and reaches the outlet. The following two pressure spikes suggest the removal of water slugs during the displacement process. After gas flows for 50 minutes, evaporation acts as the dominant role in water removal because no effluent water was observed from then on. During this phase, the differential pressure keeps dropping from 7 psi until it stabilizes at 2 psi. Meanwhile, the gas flow rate reaches a plateau of 0.032 L/min. The second phase of the water removal is usually referred to as the flow-through drying (Mahadevan and Sharma 2003).

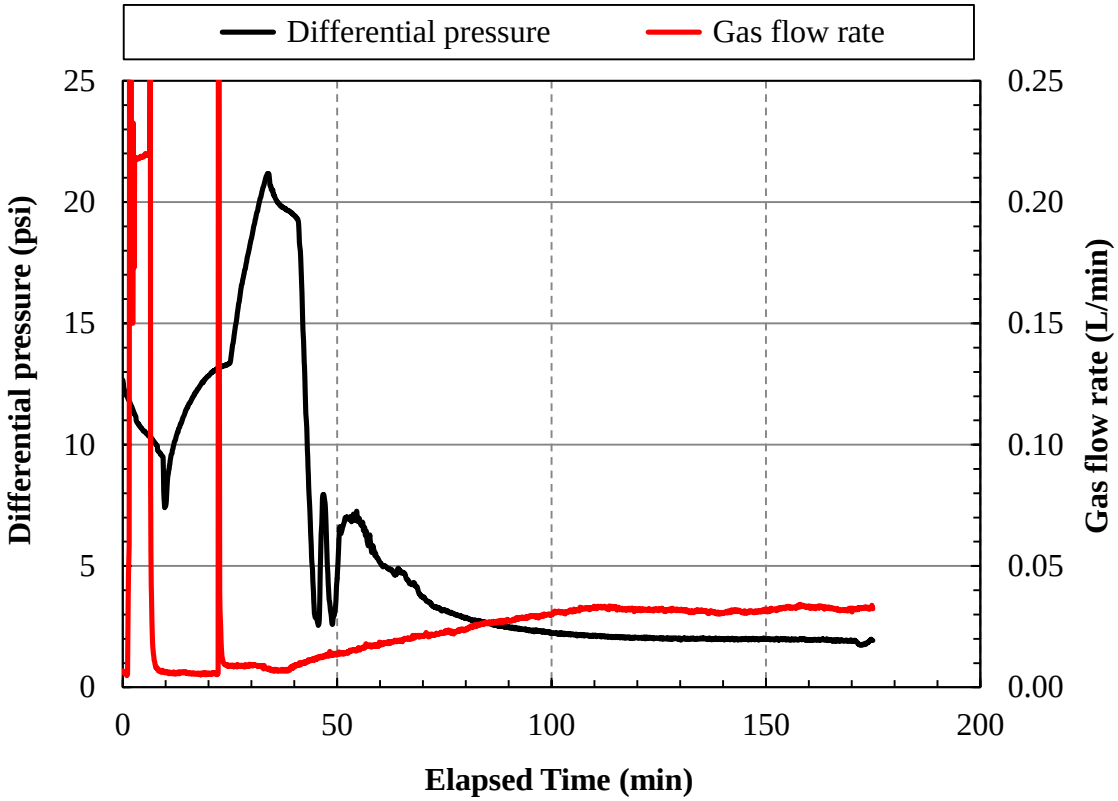

Fig. 5.8–Differential pressure and gas flow rate during the removal of water by flowing dry gas. 40/70 mesh sands at 0.10 lb/ft ²were placed.

5.3 General Observations

This section presents the observations that are universal to the experiments. It includes the unrecoverable conductivity loss after water flow, the axial displacement increase when water flows through the fracture, and the residual water held in the fracture.

5.3.1 Unrecoverable Conductivity Loss after Water Flow

One key observation during the experiment is the significant variation of fracture conductivity measured by different fluids (**Fig. 5.9**). This figure shows the fracture conductivity measured by nitrogen and water. It is obvious that after the water flow, the gas measured conductivity drops by about a log cycle.

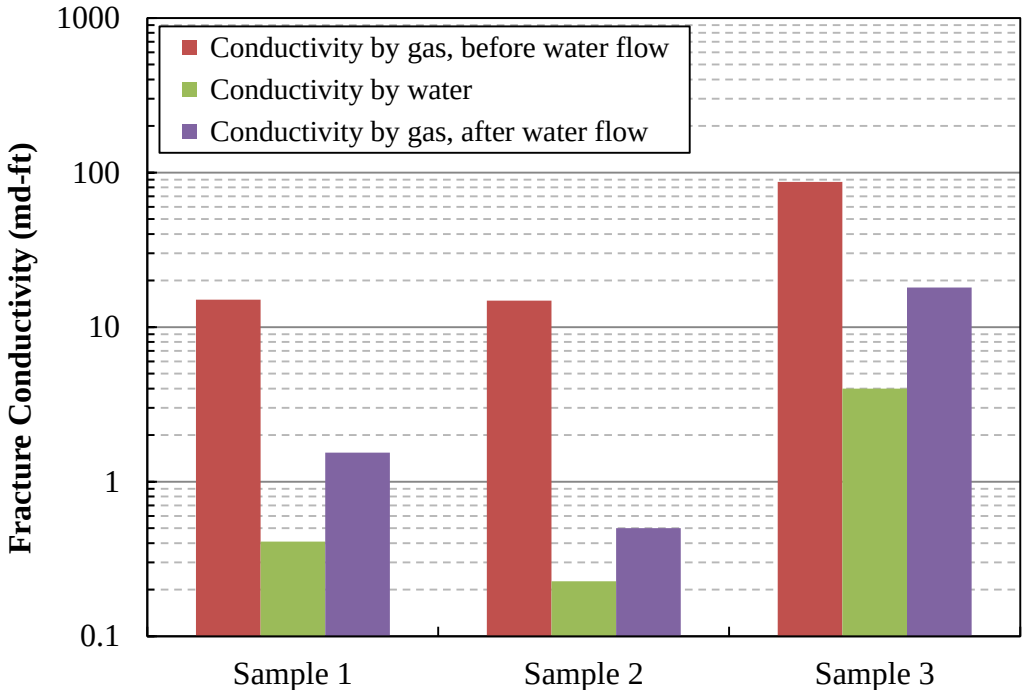

Fig. 5.9–Fracture conductivity measured by gas and water. All samples were measured at 4,000 psi closure stress.

One possibility for the higher gas measured conductivity might arise from the Klinkenberg effect that the permeability of core samples measured by air is always greater than the permeability measured by liquid (Klinkenberg 1941). Klinkenberg postulated that gases exhibit the finite velocity at the porous media surfaces while the liquids have zero velocity at the sand grain surface. The gas slippage at the sand grain surface contributes to the greater permeability. Fancher (1941) showed that, there is no significant Klinkenberg effect when permeability is higher than 25 md. With the fracture conductivity of 0.30 md-ft, assuming a fracture width of 0.02 inch (40/70 mesh sand, 0.10 lb/ft^2), the permeability is 180 md. Obviously, the Klinkenberg effect does not lead to the significantly higher gas measured conductivity.

Therefore, it is needed to investigate other factors that fundamentally cause the conductivity reduction after water flow.

5.3.2 Abrupt Axial Displacement Increase During Water Flow

Axial displacement is measured by the displacement sensor on the hydraulic load frame. It records the axial movement of the hydraulic piston due to the increment of closure stress in the direction normal to the fracture faces. **Fig. 5.10** illustrates the measurement of axial displacement of the hydraulic piston. a_1 and a_2 are measured at 2,000 psi and 4,000 psi closure stress respectively. The difference between a_2 and a_1 is caused by the compaction of rock samples and fracture closure.

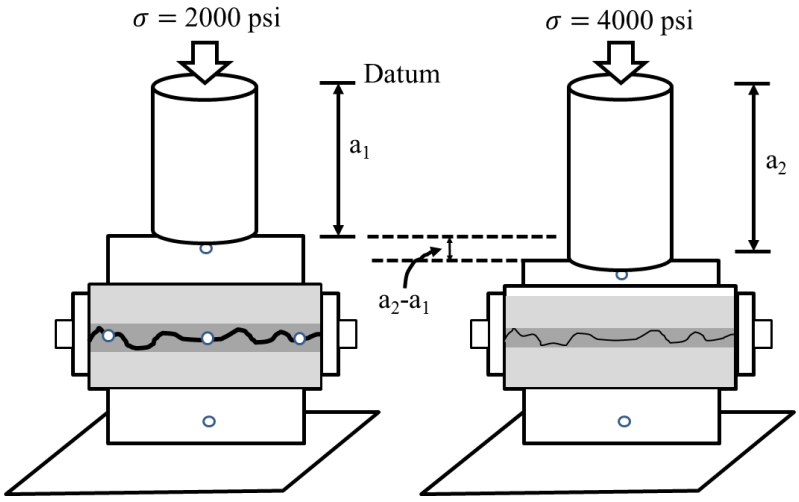

Fig. 5.10–The measurement of the hydraulic piston axial displacement.

A universal observation from the water experiments is the abrupt increase in axial displacement from the moment of water injection to the water breakthrough from the outlet, as shown in **Fig. 5.11**. In this experiment, the Barnett Shale sample with rough fracture face is propped by 40/70 mesh sands at 0.20 lb/ft². Due to the high proppant concentration, it only takes 7 minutes for water to flow through the fracture. During the 7 minutes, the axial displacement increases from 13.312 mm to 13.358 mm with an increment of 0.046 mm. The following 6 hours experiment only gives an increment of 0.022 mm including rock creep.

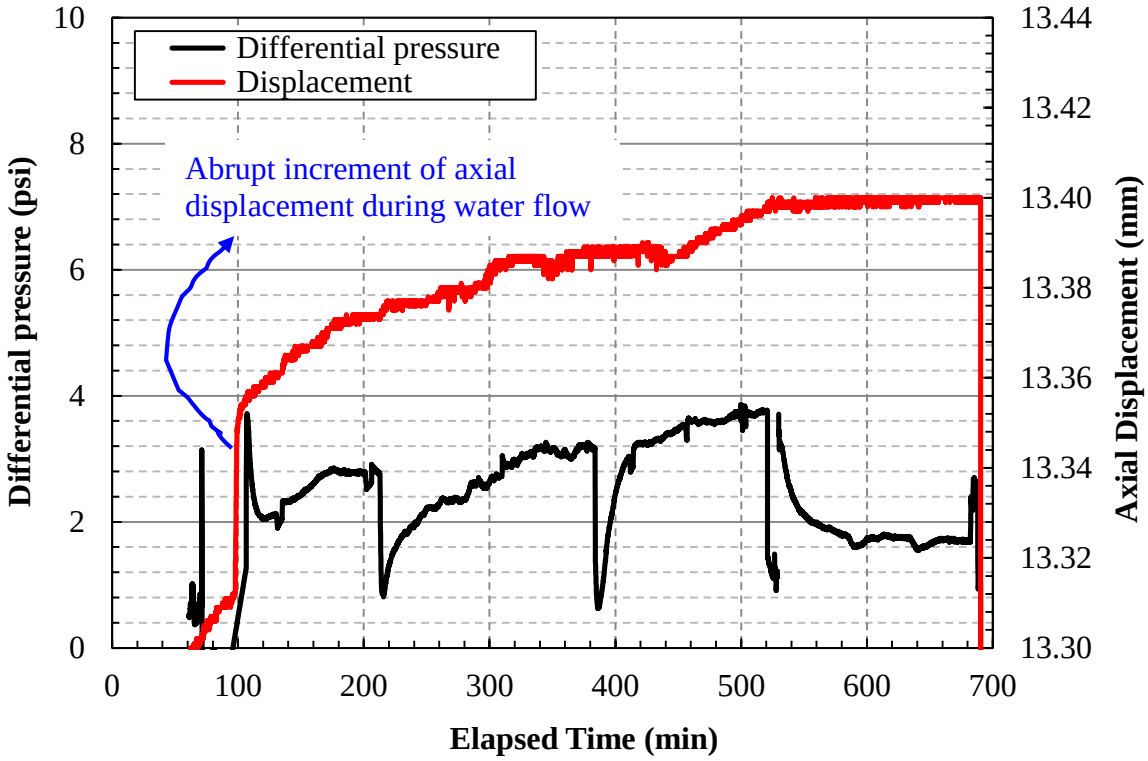

Fig. 5.11–Abrupt increment of axial displacement during water flow.

There are five possible causes for the abrupt increment of axial displacement: (1) embedment of proppant grains, (2) slope shear failure of the rough fracture surface, (3) slippage of proppant grains due to water lubrication, (4) capillary pressure effect in the proppants, and (5) over compaction of the shale matrix due to water. Except for the compaction of the matrix, the other four possibilities lead to the reduction of fracture width and fracture conductivity.

Due to the short time span and low differential pressure, it is physically unrealistic for water to flow or diffuse deep into the shale matrix at room temperature and cause the over compaction of the matrix.

In granular material packing, the resistance among particles arises from the cohesion, grain interlocking and bonding effects (Sanchez 2013). As shown in **Fig. 5.12**, the frictional resistance is dependent on the friction coefficient μ. Wetting the grain surface may reduce friction coefficient by lubrication leading to grain collapse.

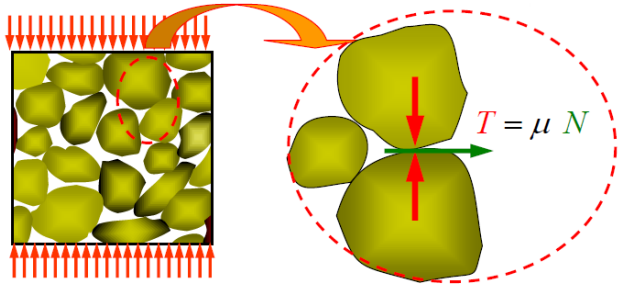

Fig. 5.12–Frictional resistance from the inter-granular stress among particles.

Another mechanism to cause the sand pack contraction is the capillary pressure effect (**Fig. 5.13**). The suction by capillary pressure increases at lower water saturation with smaller meniscus radii. The resultant force increases due to the suction pressure.

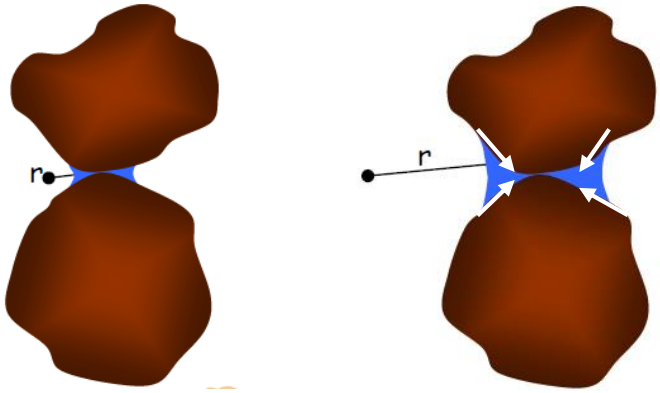

(a) (b)

Fig. 5.13–Capillary pressure effect on proppant pack collapse: (a) high capillary pressure at low water saturation due to smaller meniscus radii; (b) low capillary pressure at high water saturation with larger meniscus radii.

Geo-technical scale slope stability is concerned with the potential of landslides to cause natural disasters. The same mechanics applies to the micro-scale analysis on the stability of the fracture surface slopes and the generation of shale flakes during compaction and proppant embedment. The closure stress applying to the proppant has a shear component acting against the rough slope on the fracture surface (**Fig. 5.14**). Gravitational force and the matrix pore pressure are neglected. Shear stress acts down the shear plane and is resisted by the shear strength. Once the shear stress exceeds shear strength, shear failure happens along the failure surface and the shale flake is generated. Water accelerates the shear failure process by infiltrating into the cracks that are induced by proppant embedment. During this process, the axial displacement also increases.

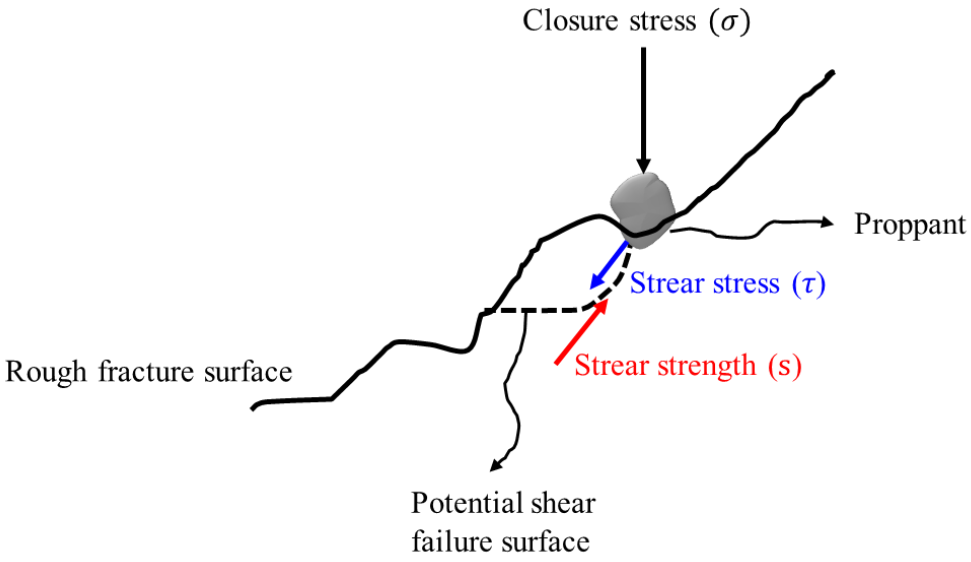

Fig. 5.14–Slope stability analysis for the rough fracture surface.

To evaluate the effects of proppant pack collapse due to water lubrication and capillary pressure as well as the slope failure, axial increments of the rough Barnett Shale

fracture, the smooth Barnett Shale fracture, and the smooth Berea sandstone fracture were measured. Results are reported in **Fig. 5.15**.

If the axial displacement increase is caused by water lubrication effect and capillary pressure, the same increment should occur to all samples regardless of lithology or surface topography as long as the proppant pack is present. However, the axial displacement increment for Berea sandstone fracture at 0.10 lb/ft^2 is only 0.01 mm in contrast to 0.05 mm in the shale fractures. What's more, if the inter-granular slippage and capillary effect were the dominant causes, the increment of axial displacement would have been proportional to the proppant pack thickness (proppant concentration). However, the thick sand packs by 0.20 lb/ft^2 and 0.30 lb/ft^2 do not have larger increments in axial displacement. Therefore, fracture width reduction due to water lubrication and capillary effect is not significant. This is because the experiments were all run at elevated closure stress of 4,000 psi which exceeds the stress range where water lubrication and capillary pressure effects occur.

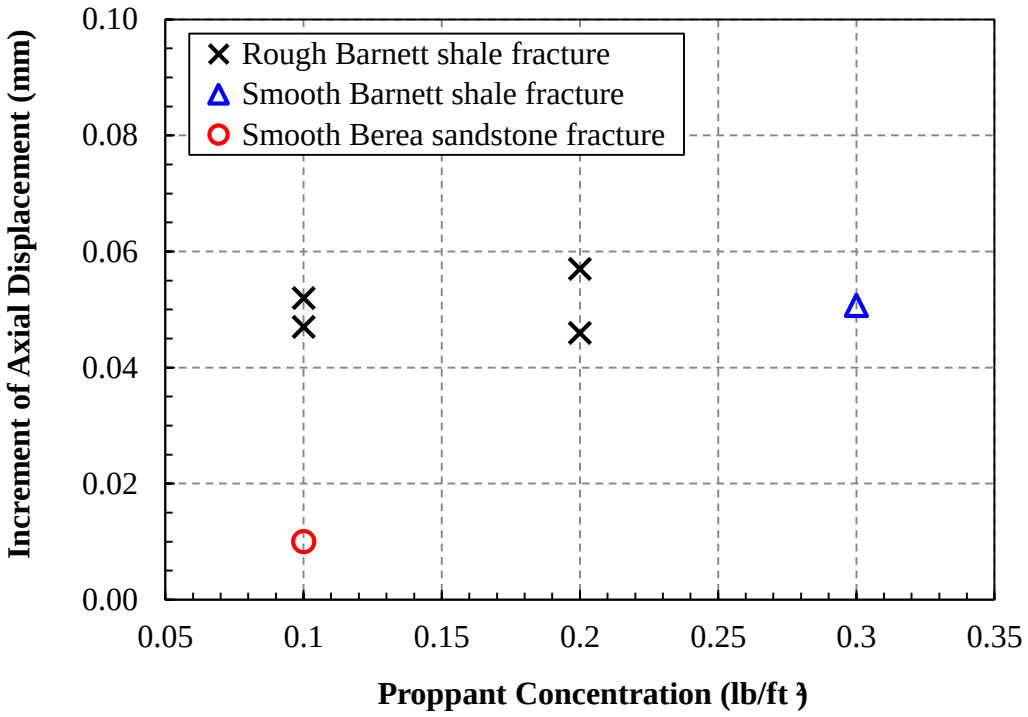

Fig. 5.15–Increments of axial displacement for the Barnett Shale fractures and the Berea sandstone fracture.

The impact of slope failure can be evaluated by comparing the increments of the rough shale fracture with the smooth shale fracture. If slope shear failure substantially contributes to the increment, the value for smooth sample would be much smaller than rough fracture. However, the rough shale fracture and the smooth shale fracture have similar increments of axial displacement, indicating the negligible contribution from the slope instability.

All of the analyses point out the fact that there is excessive proppant embedment when water wets the shale fracture surface. Proppant embedment will be quantitatively assessed in the later section.

5.3.3 Residual Water in the Fracture

From the engineering point of view, three main groups of water can exist in the shale fracture: pore water, adsorbed water, and structural water. Pore water consists of free water and capillary water. Due to the ultra-low permeability in the Barnett Shale matrix (10-100 nano-Darcy), the short time span for the experiment (less than 50 hours), and the low differential pressure between the fracture and matrix (less than 50 psi), the dominant water activity on the fracture surface under room temperature is the formation and removal of adsorbed water and capillary water.

At room temperature, the shale fracture surface is usually wet even after flowing dry nitrogen for hours after the water flow. **Fig. 5.16** shows the exposed dark wet shale fracture face after removing the thick sand layers which are mostly dried during the nitrogen flow. Clearly, the water on the fracture face is the bound water or adsorbed water.

The surfaces of the clay mineral particles carry residual negative charges as the result of the isomorphous substitution and the broken bonds occurring at the edges of the particles (Sanchez 2013). Layers of water molecules are held around the clay mineral particle by hydrogen bonding and by the dipole character of the water molecules (Terzaghi 1928). Besides the adsorption of water molecules, cations are also attracted to the clay mineral particle. The net effect is that cations form a disperse layer adjacent to the clay particle but the cation concentration decreases with increasing distance from the clay surface, as illustrated in **Fig. 5.17**.

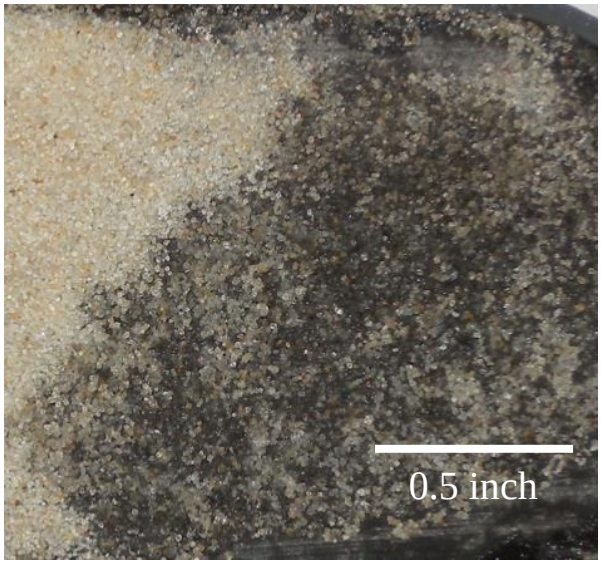

Fig. 5.16–Wet shale fracture surface from the water experiment after 10 hours of gas flow.

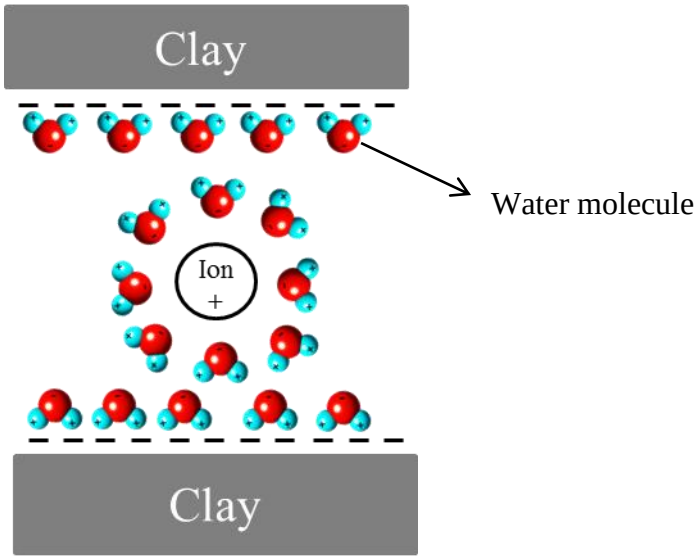

Fig. 5.17–Water molecules held on the shale surface due to the negatively charged clay.

The adsorbed water on clay surface is hard to be displaced at room temperature because the water molecules are more densely packed and are more viscous than free

water (Low 1960). The nearest layer to the particle is strongly held like a “skin”. Tscapek (1934) reported the specific gravity of the bound water layer as 1.7.

In order to study the effect of adsorbed water on fracture conductivity, dry nitrogen is flowed at 220°F to evaporate the water molecules from the shale fracture face. Details will be provided in the next section.

5.4 Results and Discussions

The previous section discussed the fracture conductivity reduction after water flow and proved that this reduction is not caused by the Klinkenberg effect. In this section, we will focus on discussing the damage mechanisms that fundamentally cause the conductivity reduction after water flow. In order to conduct a single parameter study, other experimental conditions are kept the same except the parameter that is under investigation.

5.4.1 Effect of Rock Type

Berea sandstone is chosen in the control experiment to study the effect of rock type on the conductivity damage. The mineralogical compositions of the Berea sandstone and the Barnett Shale are summarized in **Fig. 5.18**. The Berea sandstone is a quartz rich rock that contains 87% quartz with only 6% clay, while the Barnett Shale contains 55% clay and 33% quartz. Other minerals include feldspar, gypsum and traces of other minerals.

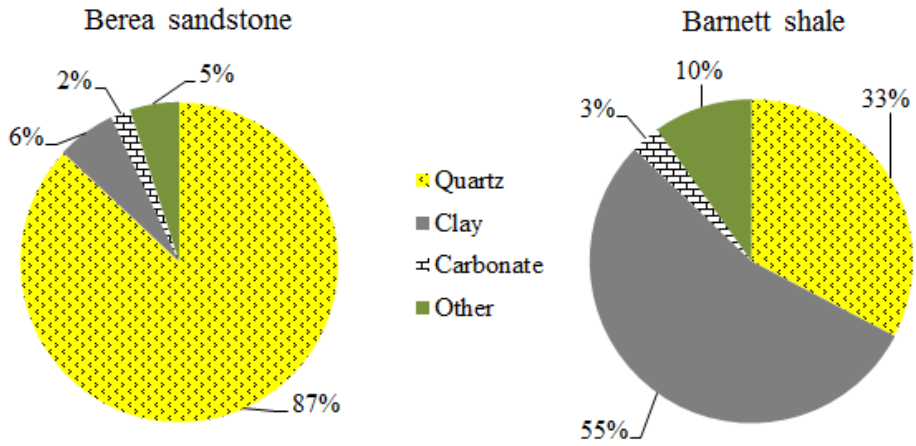

Fig. 5.18–Mineralogical compositions of the Berea sandstone (Churcher et al. 1991) and the Barnett Shale.

Fig. 5.19 compares the conductivity changes due to water flow in both the Barnett Shale and the Berea sandstone fractures. Both experiments were run with 40/70 mesh sand at 0.10 lb/ft ². The closure stress is constant at 4,000 psi. In sequence, fracture conductivity was measured by nitrogen, flowback water, and nitrogen. The initial undamaged conductivity for the Berea sandstone fracture with 40/70 mesh sand at 0.10 lb/ft ² is 65 md-ft. After water flow, the second gas measured conductivity is 61 md-ft. The 94% conductivity recovery indicates that there is negligible damage to conductivity by water in the Berea sandstone fracture. However, in the Barnett Shale fracture, the initial undamaged conductivity of 15 md-ft is significantly reduced to 0.41 md-ft after the water flow. The gas flow can only recover the fracture conductivity to 1.7 md-ft. There is 88% unrecoverable conductivity loss at the end of the experiment because of the water flow.

With all other conditions the same, the comparison on fracture conductivity of the Barnett Shale with Berea sandstone clearly suggests that the rock lithology has significant

impact on the recovered conductivity. The clay-water interaction results in severe damage to fracture conductivity in shale.

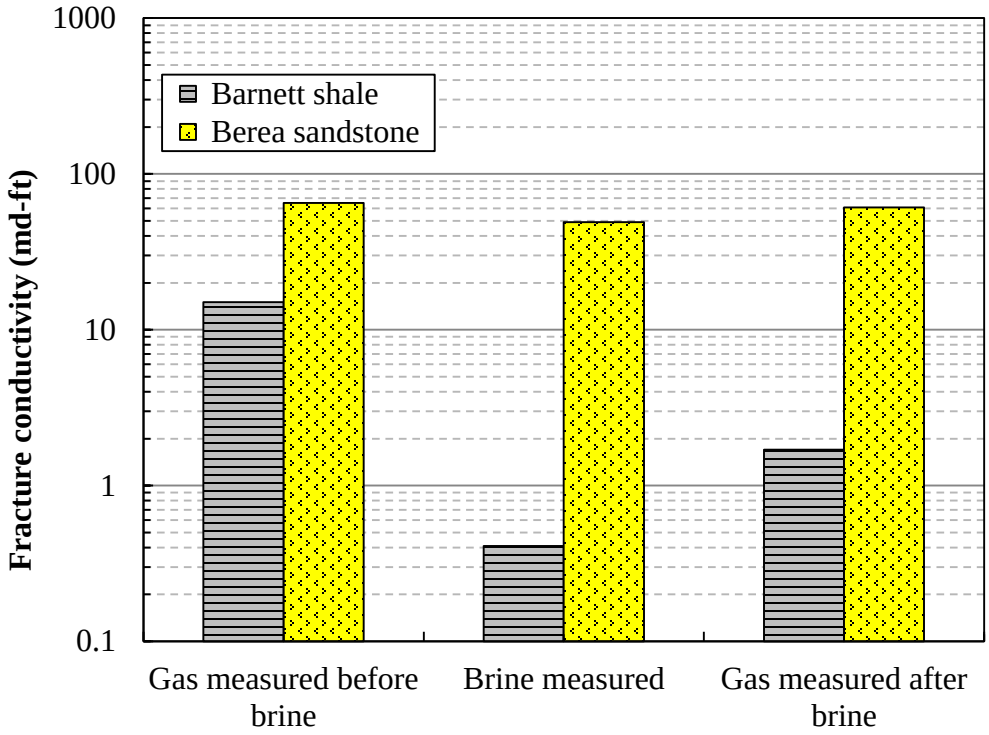

Fig. 5.19–Comparison of the fracture conductivity of the Barnett Shale and the Berea sandstone in the water experiment.

5.4.2 Effect of Shale Fines Migration

Factors that cause shale fines migration in a fracture include clay dispersion, rock face spalling induced by proppant embedment, and rough surface slope failure. Flakes and particles from shale are more round and spherical, while crushed sands are usually angular and sometimes elongated (**Fig. 5.20**). So, the shale flakes and particles are easier to be mobilized by water flow.

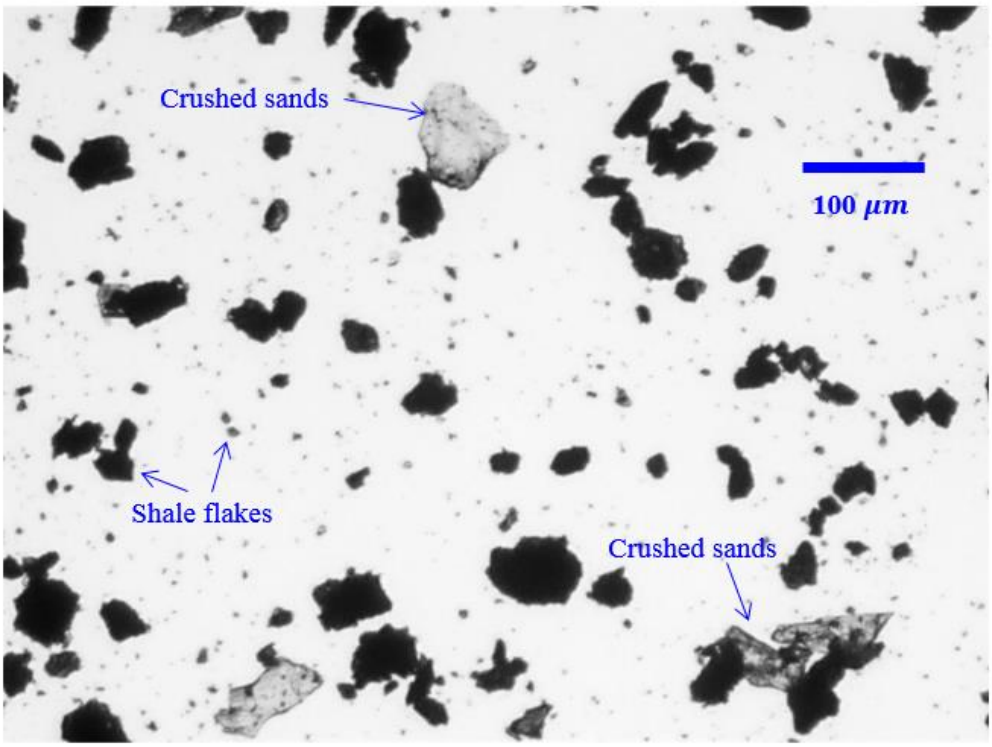

Fig. 5.20–Shale flakes and particles mixed with crushed proppants.

Statistically, fines generated from shale are much smaller than the crushed proppant fragments. The imaging processing and analysis program ImageJ was utilized to measure the size of fines. In this program, each particle is converted to a shadowed area and the total pixels are counted. The diameter of the equivalent circle that has the same area is then calculated. In this study, a total of 10,620 samples are randomly chosen with their diameters calculated. The size distribution is shown in **Fig. 5.21**. Obviously, 70% of the shale flakes have diameters smaller than 15 μm, and there is only 1% of the fines that are larger than 100 micron. The rest of the fines are well graded from 15 to 100 μm.

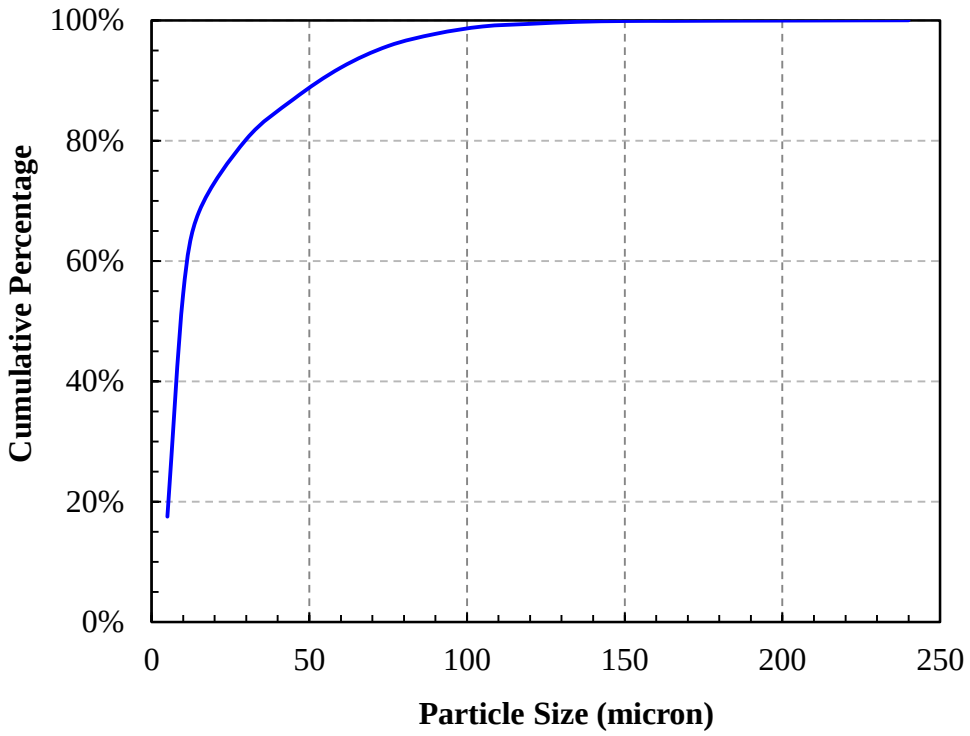

Fig. 5.21–Size distribution of shale flakes and particles.

Pore dimensions in the unit cells of systematic packing are illustrated in **Fig. 5.22**. The 40/70 mesh sand has nominal pore diameters of 12.6~165 μm in the packing. In consideration of the fine size distribution, the particles can be mobilized and pass the large pores, but will bridge or be entrapped at the pore throats. The lodged particles block the flow pathways and reduce the fracture conductivity.

To detect fines migration in the sand pack, flow directions are switched after the fracture is fully saturated with single phase water. The idea is to release the fines lodged at the pore throats in one flow direction. Khilar and Fogler (1983) reported that by switching the flow direction in Berea sandstone core flooding, 80% of the permeability can be temporarily restored. In this study, the flow direction of flowback water was switched after the steady state flow was reached. The results are shown in **Fig. 5.23**.

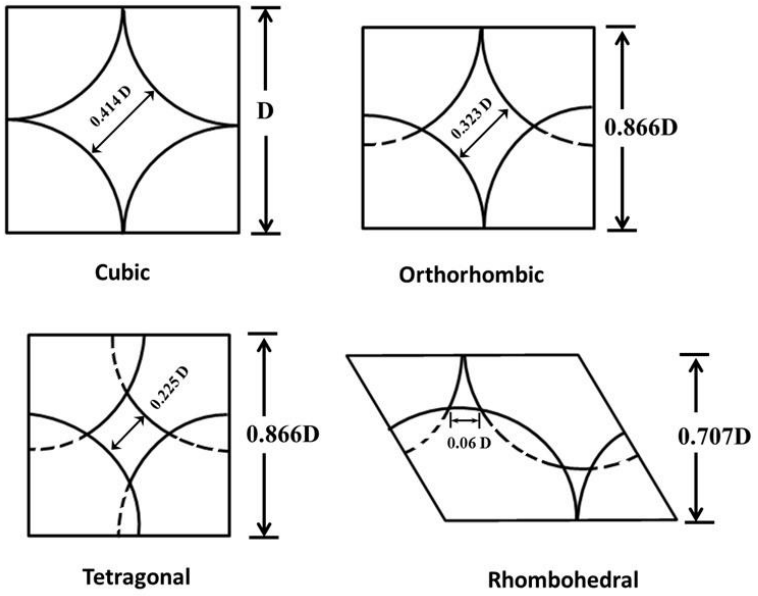

Fig. 5.22–Pore size of unit cells in the systematic packing of sand grains (Berg 1970).

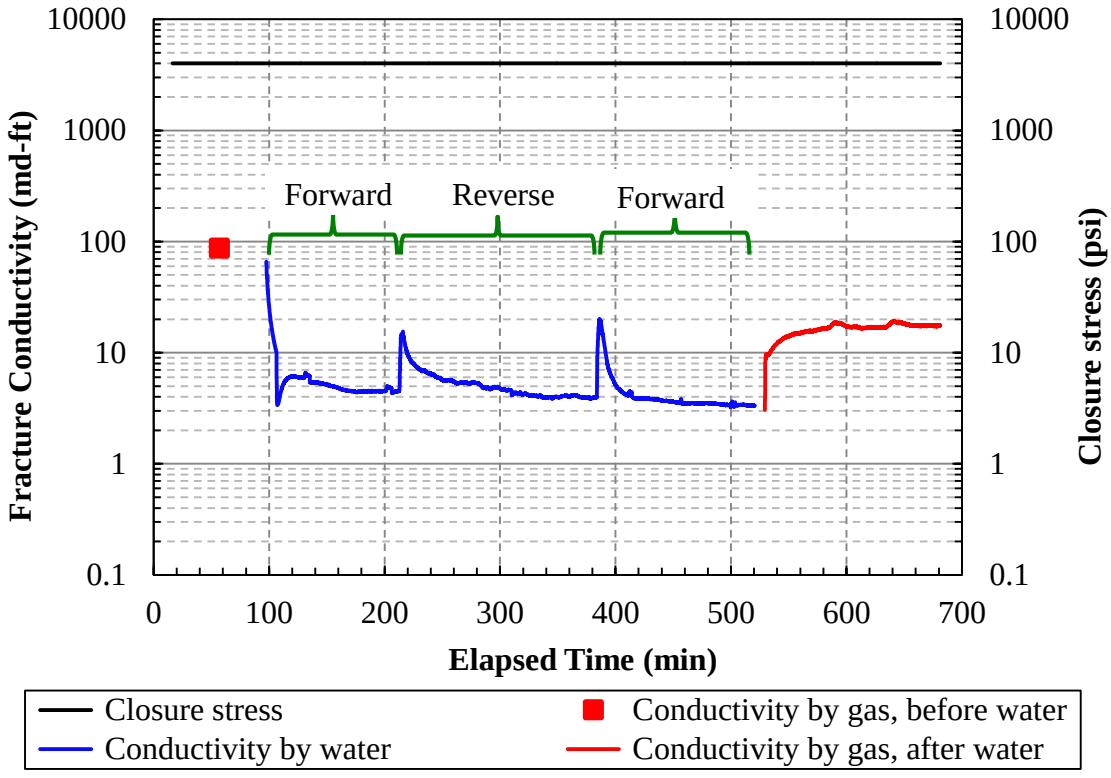

Fig. 5.23–Conductivity restoration by switching flow direction of flowback water. 40/70 mesh sands at 0.20 lb/ft ²were placed.

The undamaged fracture conductivity is 87 md-ft at 4,000 psi closure stress. The flowback water brings the conductivity down to 4.5 md-ft. When the direction of the flowback water is switched abruptly, conductivity is temporarily restored, but only back to 15 md-ft. It took two hours (about 50 pore volumes) before the fines were recaptured and the reversed flow stabilized. This is an indication of the release and re-capturing of the fines due to the flow direction reversal. The reversed flow cycles show that the fines migration is responsible for about 15 md-ft conductivity loss, approximately 20% of the total conductivity reduction. At the end of the experiment, the recovered fracture conductivity is 18 md-ft with a total loss of 69 md-ft which is 80% loss out of the initial fracture conductivity.

Scanning Electron Microscopic images were taken to study the texture of the fines generated from the shale fracture face. **Fig. 5.24(a**) shows that shale particles are attached to the sand grain surface and a collection of the particles clog the flow channel between the sands. **Fig. 5.24(b)** shows a crushed half sand particle which is fully covered by the fines. Scanning Electron Microscope-Energy Dispersive X-Ray tests verify that the particles adsorbed to the sand surface are clay (**Fig. 5.25)**.

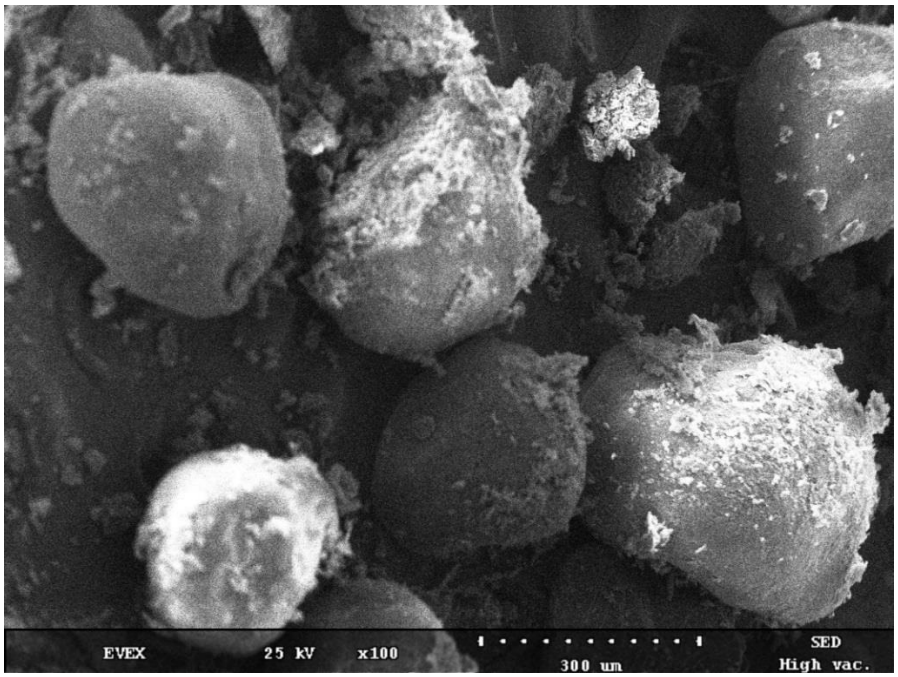

(a)

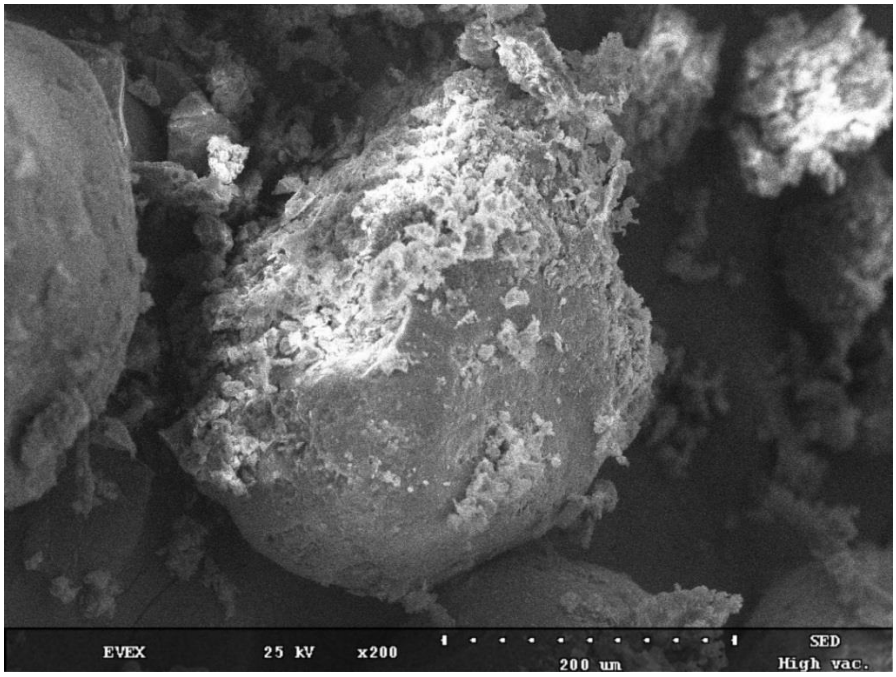

(b)

Fig. 5.24–Scanning Electron Microscopic images of the clay particles attached to the sand grains at the downstream end of the sand pack after water flow.

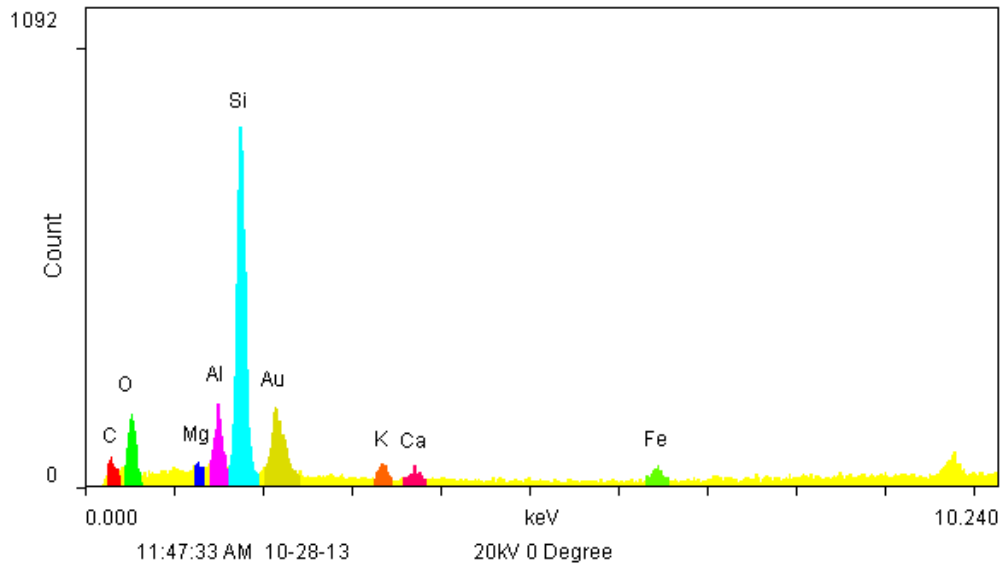

Fig. 5.25–Element intensity of the clay particles attached to the sand grain.

5.4.3 Effect of Proppant Fines Migration

Proppants can be crushed at elevated stress and fines are generated. Fines are mobile and can migrate inside the proppant pack reducing the fracture conductivity. Gidley et al. (1995) found that the upstream half of the proppant pack has the largest permeability, followed by the total pack permeability, and the downstream half has the smallest permeability. Sieve analysis proved their finding that the downstream half contained more fines than the upstream half. They concluded that fines from the crushed 20/40 Jordan sands flow together with water and gas inside the fracture. Prior to the work by Gidley et al., Muecke (1979) noticed the same issue in his study.

It is difficult to follow the method by Gidley et al. (1995) to study the proppant fines migration in the shale fracture, because of (1) uncertainty in sand placement might cause the variation of conductivity between the two halves of the sand pack, (2) the rough

surface might bring in more variables concerned with the distribution of proppants, and (3) the mixture of sands and shale flakes cannot be separated for sieve analysis. Instead, in this study, 30/50 mesh white sands and 30/50 mesh green resin-coated sands were placed on each half of the fracture with a total concentration of 0.20 lb/ft^2 (**Fig. 5.26**). Crushed sands can be visually detected by a microscope. Gas and water flowed from the white sand to the green sand because the crushed angular white sands are easy to be detected by the microscope with the oblique light. Results are shown in **Fig. 5.27**.

Fig. 5.26–Placement of 30/50 mesh white sand and green resin-coated sands to study proppant fines migration.

Flowback water and gas were injected at 0.5 mL/min and 0.25 L/min, respectively. Both flow rates are at the high end among the water experiments. Conductivity by water quickly stabilizes after 1.5 hours injection. Gas was flowed right after for about 12 hours.

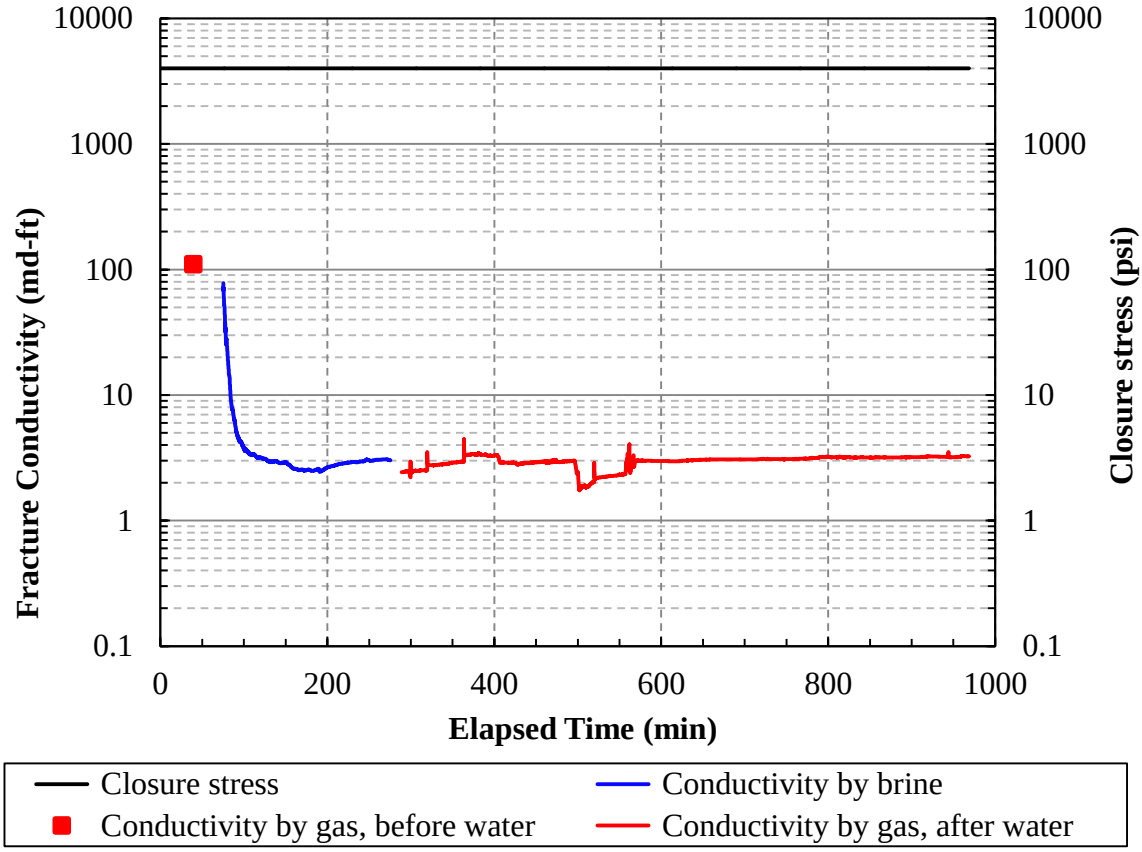

Fig. 5.27–Conductivity by two colors of proppants to study proppant fines migration.

Microscopic images were taken as shown in **Fig. 5.28**. Little crushed angular white sands are not found in the green resin-coated sands at the downstream half of the sand pack. The results indicate that (1) the flow rates in this study are not high enough to mobilize the crushed sands, and (2) the 40/70 sands do not provide a pore network that is large enough for the crushed sands to flow through. The proppant fines migration that Gidley et al. reported happened at flow rate of 34 mL/min. Also it shows that fines migration is more severe in larger sands (**Fig. 5.29**).

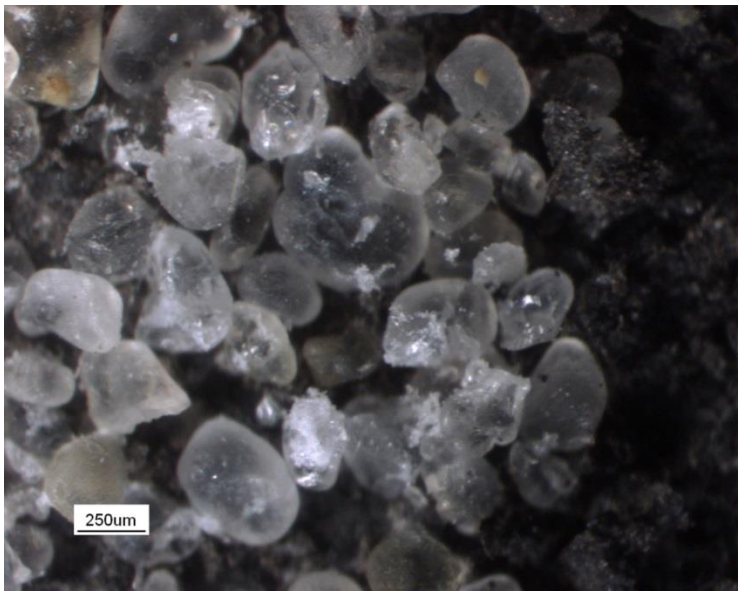

(a)

(b)

Fig. 5.28–Microscopic images of sands after the water: (a) crushed 30/50 mesh white sand in the upstream half of the pack; (b) crushed 30/50 mesh resin-coated sand in the downstream half of the pack.

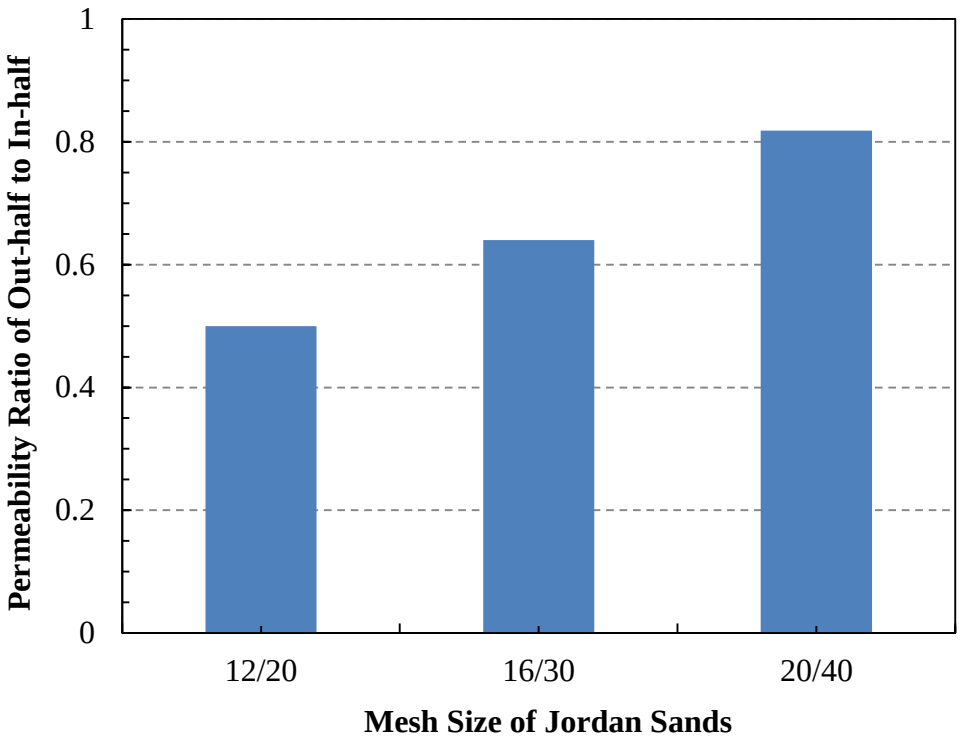

Fig. 5.29–Permeability ratio of the downstream half fracture to the upstream half fracture by different sizes of Jordan sands (The ratios are calculated based on the data reported by Gidley et al. 1995).

5.4.4 Effect of Longer Term Rock Creep

Longer term fracture conductivity was measured with 100 mesh and 40/70 mesh sands at 0.10 lb/ft^2 to study the effect of long term rock creep and proppant failure on fracture conductivity. According to the recommended practices in ISO 13503-5, long term conductivity tests should last 50 hours ± 2 hours. Since the objective of this research is not to study proppant crushing, tests were only run up to 6,000 psi closure stress. The first test was done with a saw-cut smooth fracture as compared to the second test with a rough aligned fracture. Both tests were run at the same experimental conditions as the short term measurements introduced above. Results are shown in **Fig. 5.30**.

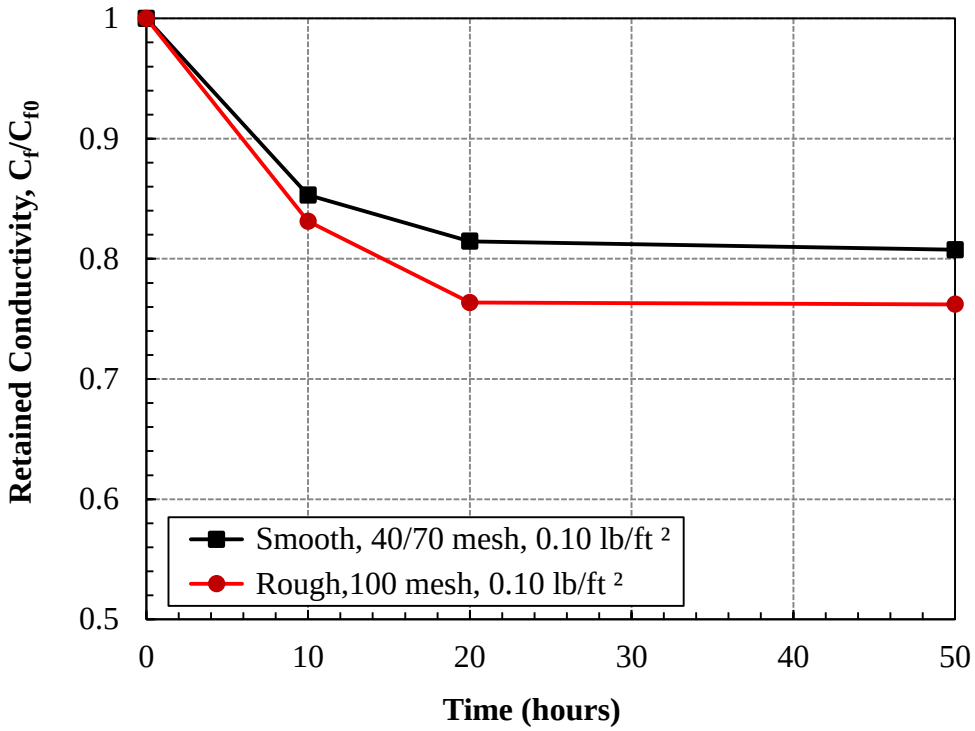

Fig. 5.30–Retained fracture conductivity over longer period of measurement time.

For the smooth sample with 40/70 mesh sand, conductivity decreases by 15% in the first 10 hours and continues dropping by another 4% in the second 10 hours. The conductivity reductions for the rough fracture with 100 mesh sand at the same concentration are 17% and 7% for the first and second 10 hours respectively. For both tests, conductivities stabilize after 20 hours with total reductions of 19% and 24%.

5.4.5 Effect of Brine Concentration

The effect of brine concentration on clay stability is usually demonstrated by water shock experiments where the flow through the sample is switched from brine to fresh water abruptly. In sandstone cores, water shock experiments show that the damaged permeability can be only 1% of the original permeability (Khilar and Fogler 1983). The

significant damage to formation flow capacity can be attributed to the dispersion and plugging by clay flakes in sandstone cores.

To investigate the impact of brine concentration on shale fracture conductivity, 2% KCl was injected followed by fresh water. This flow sequence is inverse to what happens during the fracturing job where the fracture is exposed to fresher fracturing fluid first and then to the saltier flowback water. The reason for the inverse flow sequence is to demonstrate the water shock phenomenon. **Fig. 5.31** shows the fracture conductivity by 2% KCl and fresh water. Conductivity measured by dry gas decreases from 120 md-ft to 15 md-ft in response to the closure stress ramping up from 1,000 psi to 4,000 psi. Closure stress was kept at 4,000 psi after the first nitrogen flow. After about 3 hours of transient flow, fracture conductivity by water stabilizes at 0.23 md-ft. The second nitrogen flow recovers the fracture conductivity to 0.49 md-ft, which is just 3% of the original undamaged conductivity. Right after the removal of 2% KCl by gas, fresh water was injected and the conductivity by fresh water is only 0.037 md-ft, 16% of the conductivity measured by 2% KCl.

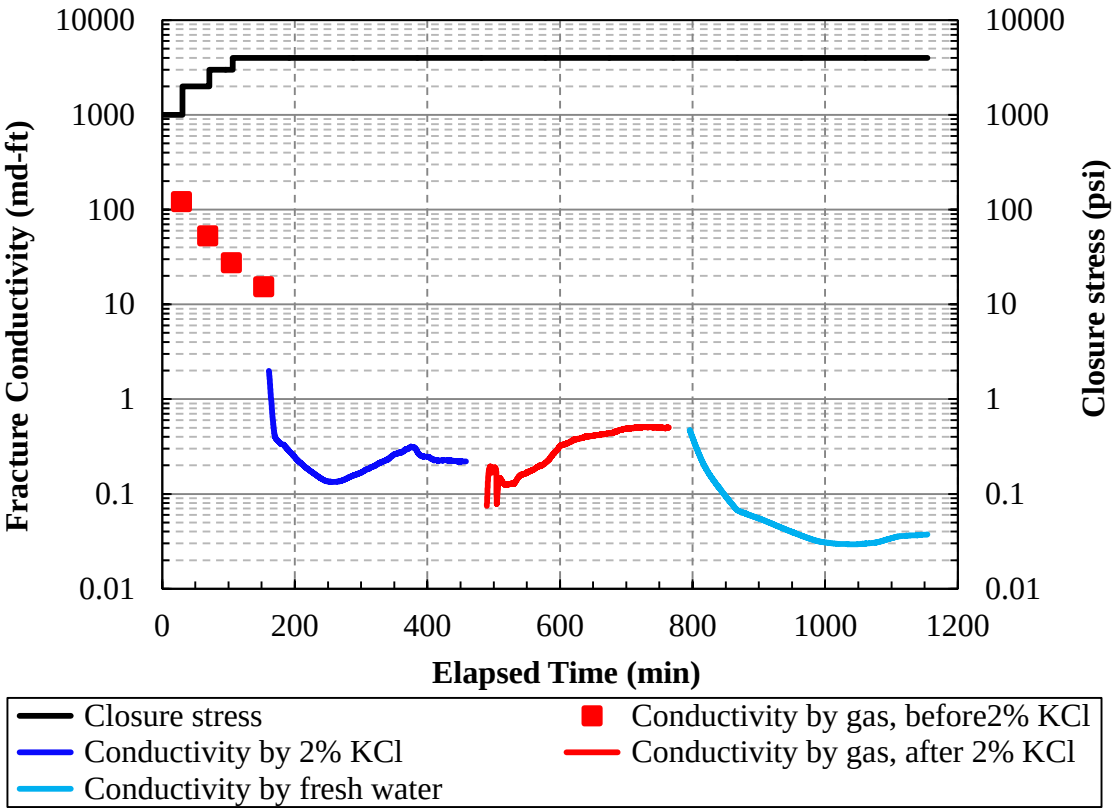

Fig. 5.31–Fracture conductivity measured by 2% KCl and fresh water. This Barnett Shale fracture was placed with 40/70 mesh sands at 0.10 lb/ft^2.

However, the water shock effect was not successfully reproduced in other experiments where the conductivities measured by brine and fresh water are not much different. **Table 5.1** summarizes the results of all water shock experiments. The experiments used the Barnett Shale samples and were run at 4,000 psi closure stress. It can be seen that except for experiment No.1, the other two experiments do not show the water shock phenomenon. The inconsistency of water shock results is caused by the different initial fracture conductivities. Experimental data show that the fracture with higher initial conductivity can overcome the damage. The shale flakes and particles released from the fracture wall tend to settle down to the bottom close to the fracture face

due to gravity, leaving the internal pack intact from the impairment (**Fig. 5.32**). With a thicker proppant pack where the flow capability relies on the internal intact proppant grains, the damage is much smaller compared with the thin proppant pack where the flow area close to the fracture face dominates the flow capability.

Table 5.1–Conductivities measured by brine and fresh water in water shock experiments.

No.	Sand mesh size	Sand concentration (lb/ft^2)	Initial conductivity (md-ft)	Conductivity by brine (md-ft)	Conductivity by fresh water (md-ft)
1	40/70	0.10	15	0.23	0.037
2	40/70	0.20	65	3.46	3.24
3	30/50	0.20	110	3.19	2.79

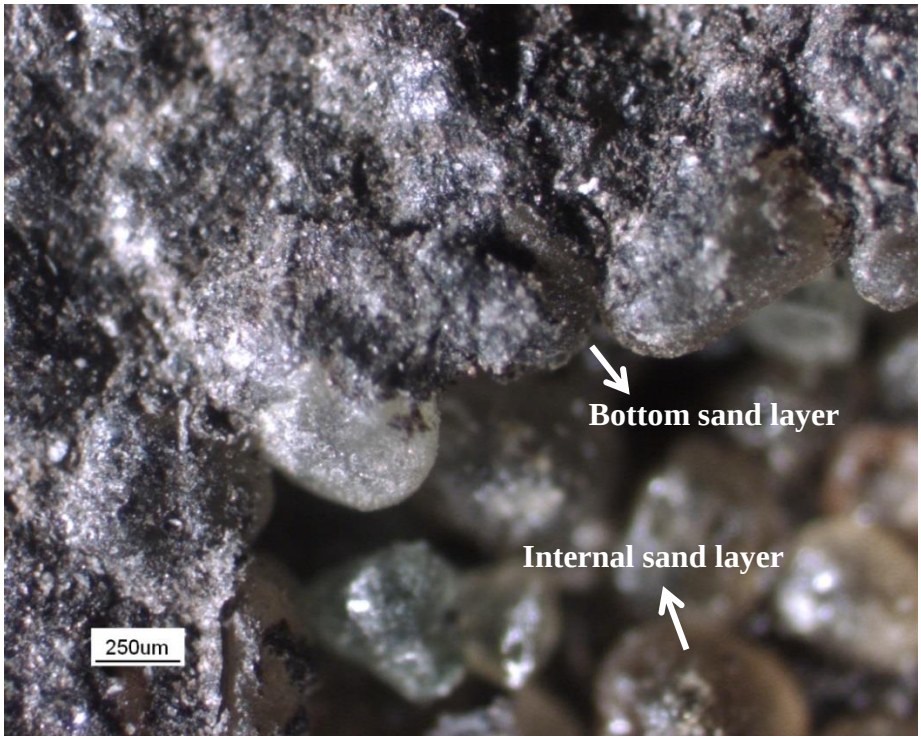

Fig. 5.32–Flakes and particles attached to the bottom layer of sands. The internal sand layers are clean and mostly intact.

5.4.6 Effect of Residual Water in the Fracture

Residual water inside the fracture reduces fracture conductivity by blocking the effective flow path. The removal of the residual water from the fracture depends on the pressure drop, temperature, and the volatility of the liquid (Mahadevan and Sharma 2003). Experiments under 70 °F and 220 °F were run to look into conductivity recovery during the removal of residual water. Results are shown in **Fig. 5.33**.

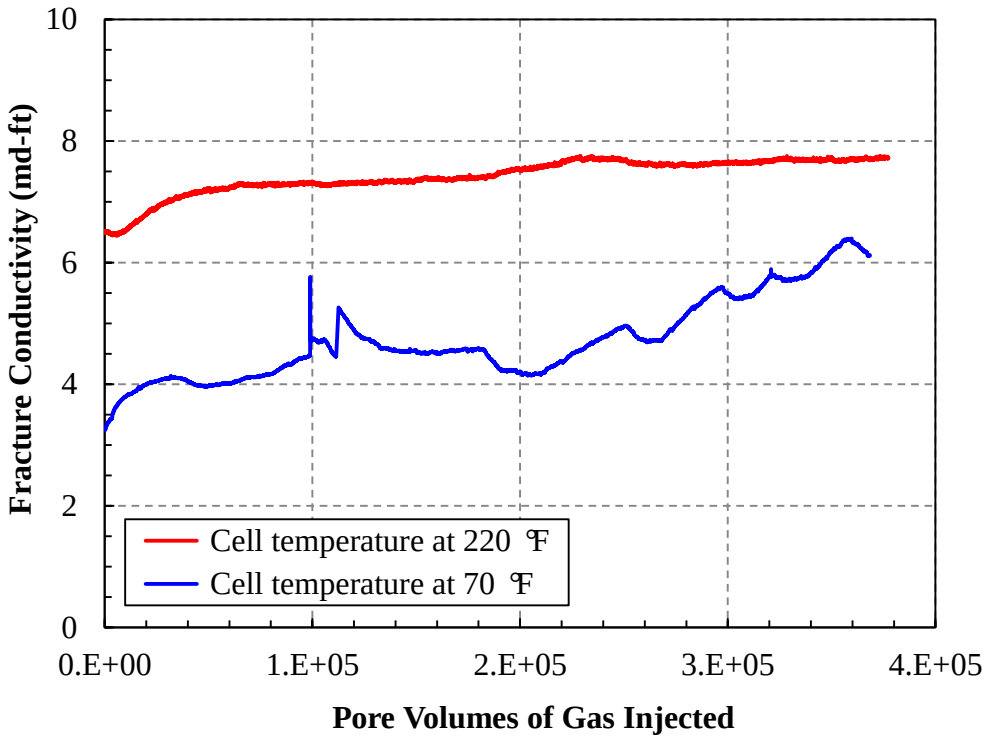

Fig. 5.33–Fracture conductivity recovery with increasing injected gas volume at 220 °F and 70 °F, assuming ϕ= 0.35.

Both experiments lasted for about 20 hours. Assuming the porosity is 0.35, the total pore volume of gas injected is about 370,000. The initial conductivities for the experiments are 84 md-ft and 110 md-ft, respectively. For the experiment at 70 °F,

conductivity keeps increasing as more dry gas flows through the wet fracture surface. Towards the end of the experiment, the proppant pack is dry but the fracture walls are still wet. As a comparison, when the fracture is heated up to 220 ℉, conductivity increases in a more stable manner. After 10 minutes of gas flow (3,500 pore volume), no visual water droplets flowed out. At this point, the fracture conductivity is 6.5 md-ft. The final conductivity is 7.7 md-ft after the sample is fully dry (**Fig. 5.34**).

Fig. 5.34–Fracture surface is fully dry after 20 hours of gas flow at 220 ℉.

5.4.7 Section Summary

Findings from the parametric study are summarized below:

(1) Rock lithology determines the fracture conductivity damage by water. High clay content in the Barnett Shale is responsible for the significant conductivity reduction compared with the Berea sandstone where there is little reduction in fracture conductivity after water flow.

(2) Fines generated from the shale fracture due to fracture face spalling, slope instability, and clay dispersion can migrate inside the proppant. Median diameter

of the shale fines is 10 μm. Fines attached to the sand surface clogging the pore throats are identified to be clay-rich. They are responsible for approximately 20% of the conductivity reduction.

(3) There is no evidence of crushed proppants migration in this study, probably due to the lower flow rates and smaller size of proppants.

(4) Longer term rock creep and proppant failure account for a 20% reduction of the fracture conductivity.

(5) Fresh water reduces the fracture conductivity by one order of magnitude at initial fracture conductivity of 15 md-ft. With initial fracture conductivity of 65 md-ft and above, fresh water does not damage fracture conductivity significantly.

(6) Removal of the residual water by evaporation slightly helps recover the fracture conductivity from 6.5 md-ft to 7.7 md-ft and from 4.1 md-ft to 6.1 md-ft out of initial conductivities to gas flow of 84 md-ft and 110 md-ft, respectively.

5.5 Shale Fracture Surface Softening

We have demonstrated that long term rock creep and shale fines migration account for approximately 40% of the conductivity reduction after water flow. The remaining 40% ~ 57% of the conductivity reduction is attributed to the excessive proppant embedment due to the shale fracture surface softening.

Microscopic images of proppant embedment were taken for both experiments with and without water flow. **Fig. 5.35(a)** shows the "moon-surface-like" image of a fracture face under oblique light after a water experiment. The embedment craters congregate on the fracture surface next to each other. In **Fig. 35(b)**, some proppants are

completely buried into the fracture face. **Fig. 5.36** shows the Barnett Shale fracture that is only exposed gas. Obviously, the embedment is much less and shallower than the fracture exposed to water.

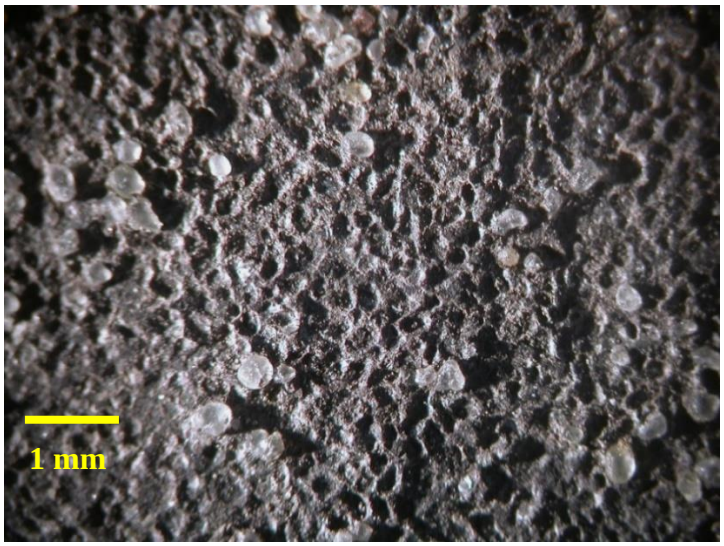

(a)

(b)

Fig. 5.35–Microscopic images of 40/70 mesh sand embedment on the Barnett Shale fracture after conductivity measurement with water. 4,000 psi closure stress was applied.

Fig. 5.36–Microscopic image of 40/70 mesh sand on the Barnett Shale fracture surface after conductivity measurement with gas only. 4,000 psi closure stress was applied.

Proppant embedment depth was then measured by a microscope at five locations spaced by one inch (**Fig. 5.37**). This image also highlights the fracture surface roughness. The red and blue regions represent the surface hills and valleys respectively. During the measurement, the focus of the microscope was adjusted from the bottom of the embedment crater to the surrounding by an increment of 10 μm. The embedment depth was also measured in a control experiment where only gas was flowed. The comparison is shown in **Fig. 5.38**.

For the fracture surface after water flow, the average embedment depth is about 140 μm while the average depth for the sample only exposed to gas is just 40 μm. The median diameter of the 40/70 mesh sand is 300 μm. This means, on average, half of the sand grain is buried on a single fracture face after it is exposed to water due to the shale surface softening.

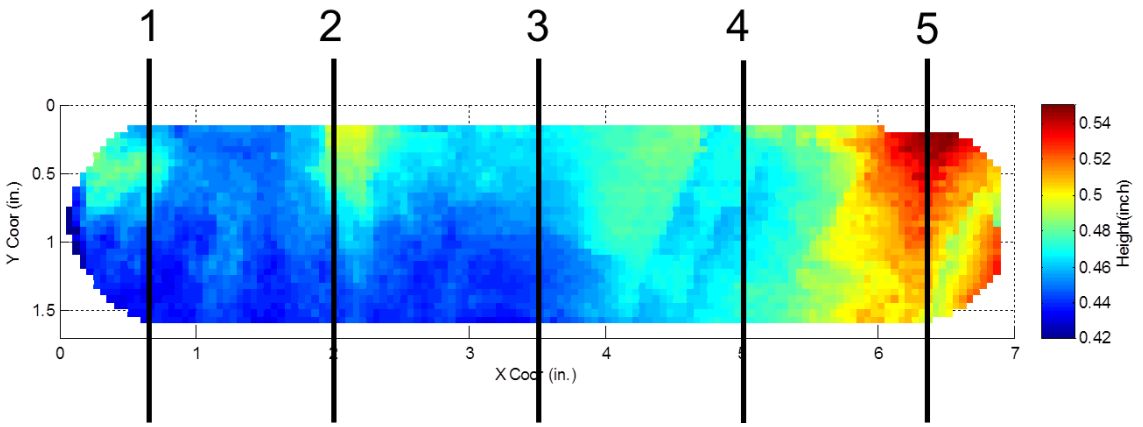

Fig. 5.37–Measurement locations on the shale fracture surface.

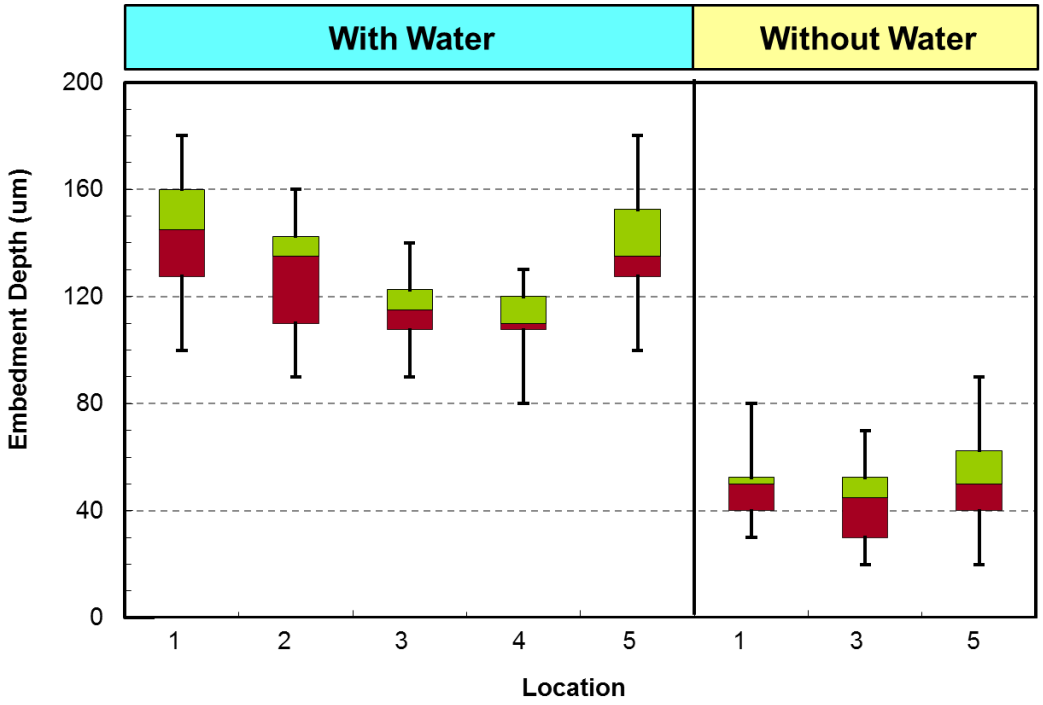

Fig. 5.38–Comparison of the embedment depth after water test with that of a dry gas test. 40/70 mesh sands were placed on both fractures. The boxplot shows the maximum, 75%, median, 25% and the minimum embedment depths. Proppants were subject to 4,000 psi closure stress.

Direct measurements of rock mechanical properties prove the shale surface softening as a function of water content (Lin and Lai 2013). It was reported that Young's modulus and uniaxial compressive strength of Barnett Shale are strongly correlated to the sample water saturation (**Fig. 5.39** and **Fig. 5.40**). Comparing with the dry shale sample, a sample with 35% water saturation has a Young's modulus that is 22% less and the uniaxial compressive strength (UCS) is reduced by 35%.

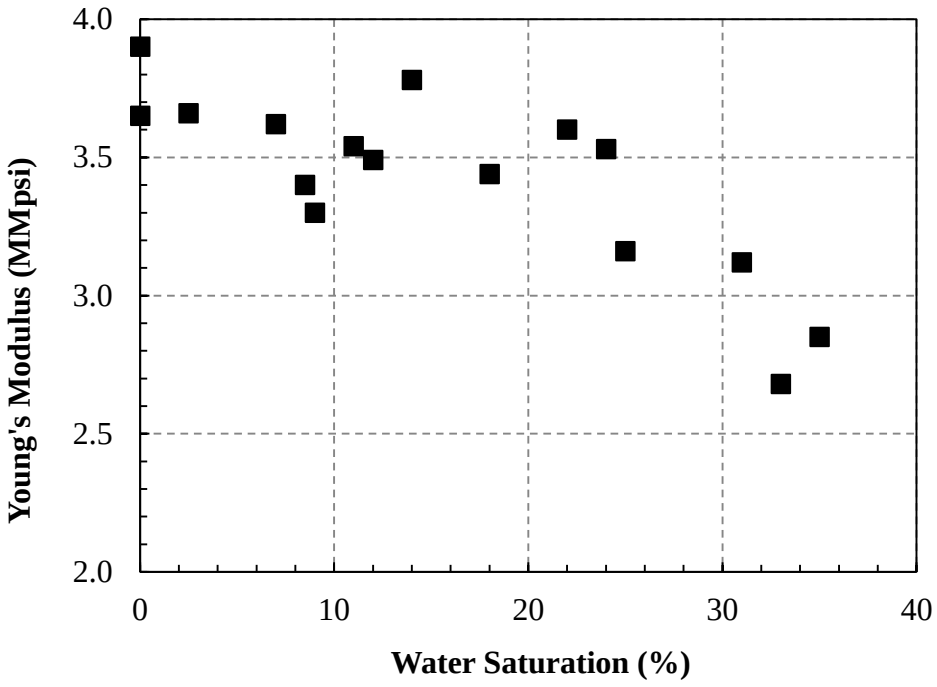

Fig. 5.39–Reduction of Young's modulus of the Barnett Shale with increasing water saturation (Lin and Lai 2013).

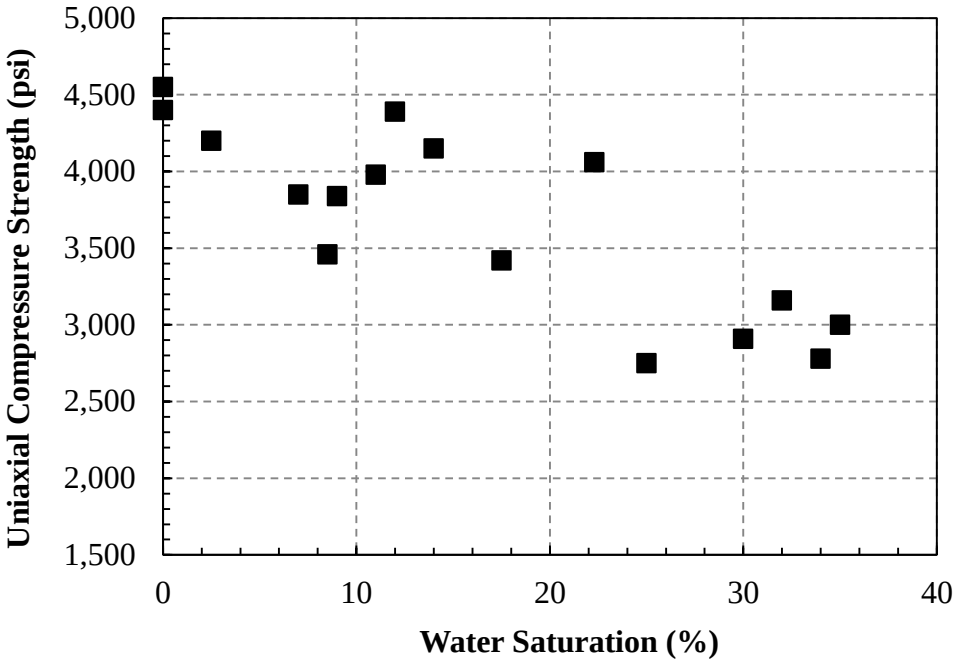

Fig. 5.40–Reduction of uniaxial compressive strength of the Barnett Shale with increasing water saturation (Lin and Lai 2013).

5.6 Recovered Fracture Conductivity by Gas

It is found out that high initial undamaged fracture conductivity helps restore the conductivity after water damage. This section focuses on describing the relationship between initial fracture conductivity and the recovered conductivity. The mechanism underneath the empirical correlation is also explained.

Initial fracture conductivities and their corresponding recovered fracture conductivities are plotted in **Fig. 5.41**. The data points are collected from experiments at the same conditions. In the testing range, there is a power-law trend between the initial and recovered fracture conductivities. The data are more scattered at lower initial fracture conductivity where 40/70 mesh sands at 0.06 lb/ft^2 and 0.10 lb/ft^2 are placed. This is related to the existence of unpropped fracture and proppant monolayers at the fracture

surface hills and slopes, because these areas are more susceptible to water damage. At elevated stresses, these regions tend to close up easier after water flow than the heavily propped areas. Water damage to shale fracture conductivity mainly happens to the flow areas close to the fracture walls. With the same proppant size, fracture with higher conductivity has more proppant layers and the dominant flow channels are created by the inner pack which is usually much cleaner and more conductive.

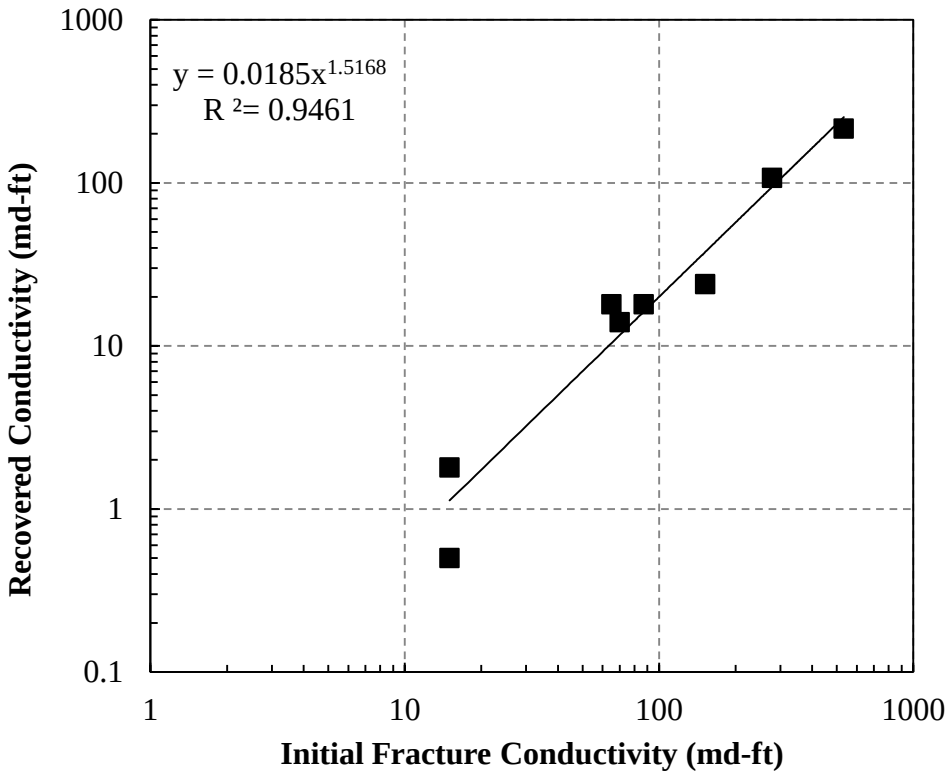

Fig. 5.41–The relationship between initial and recovered fracture conductivities in the Barnett Shale.

The idea that fewer layers of proppants are more prone to water damage has also been demonstrated by the methodology proposed by Ouyang (2013). In this model, fluid flow is simulated through the fracture containing finite number of proppant particles as

Fig. 5.42(a) shows. After the fracture surface is exposed to fresher water during fracturing and flowback, the fracture surface is softened and excessive proppant embedment occurs. The effective flow area in the proppant pack is only the shadowed portion in **Fig. 5.42(b)**. Pressure drop is calculated across the proppant packs containing one layer, two layers and three layers. The ratio of the residual fracture conductivity to the initial conductivity without embedment is plotted versus the ratio of the embedment volume to the volume of a half proppant grain (**Fig. 5.43**).

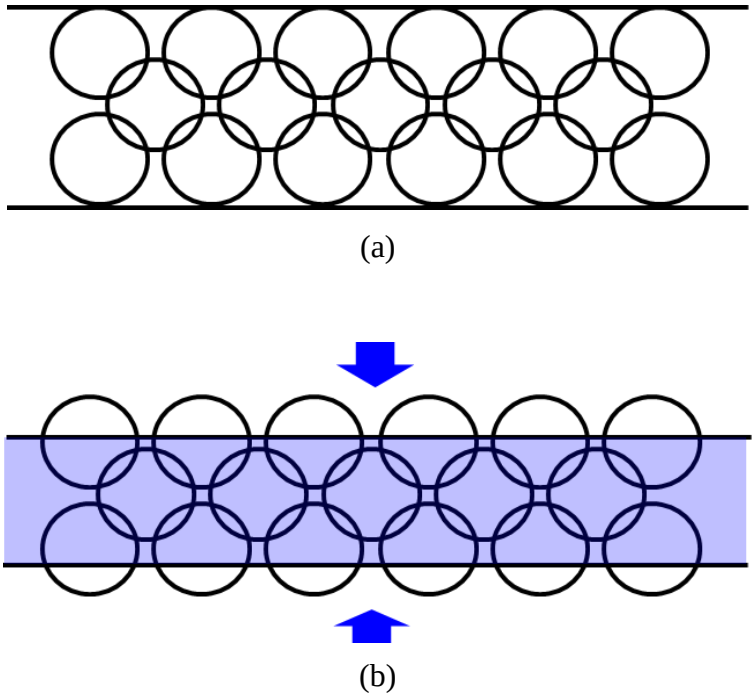

(a)

(b)

Fig. 5.42–Top view of the propped fracture: (a) before closure; (b) after closure.

Results show that the first 10% of embedded volume has a significant impact on conductivity reduction. For a single layer proppant, the 10% volume embedment is responsible for over 80% of the reduction in fracture conductivity. By adding another proppant layer, the conductivity reduction due to embedment decreases to 50% with the

same grain volume loss. This is because for a single layer of proppants, conductivity is provided by the "trumpet-shaped" area (**Fig. 5.44**), while with increasing sand layers, fracture conductivity depends less and less on the flow area close to the fracture walls where the damage occurs.

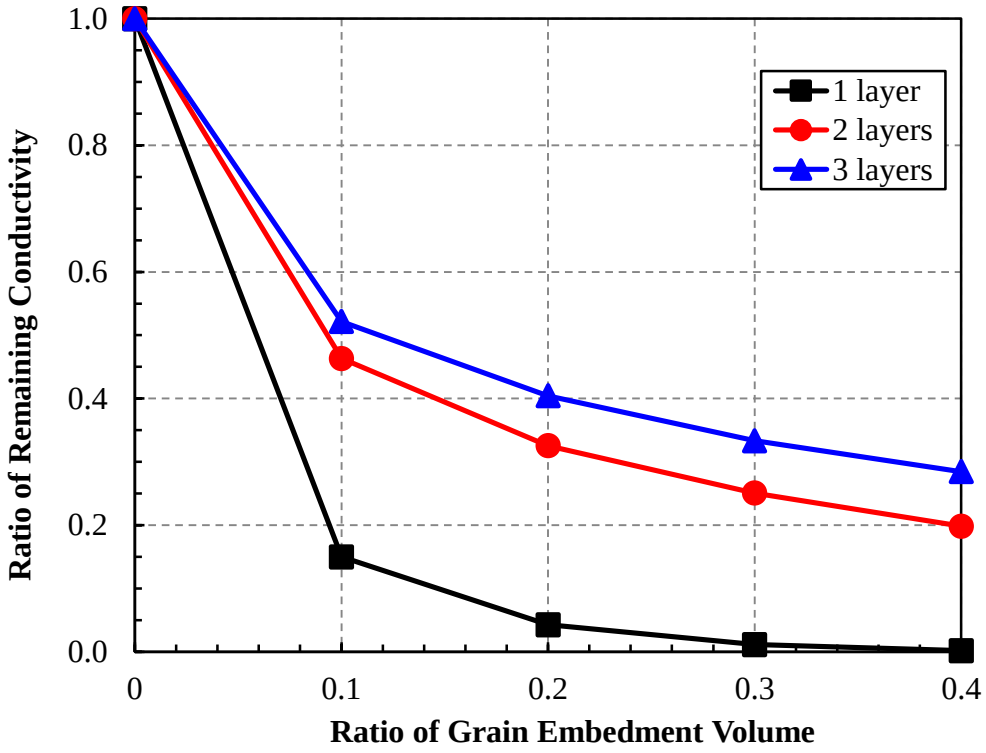

Fig. 5.43–Ratio of the residual conductivity to initial conductivity without embedment versus ratio of the embedded volume to half of the grain volume.

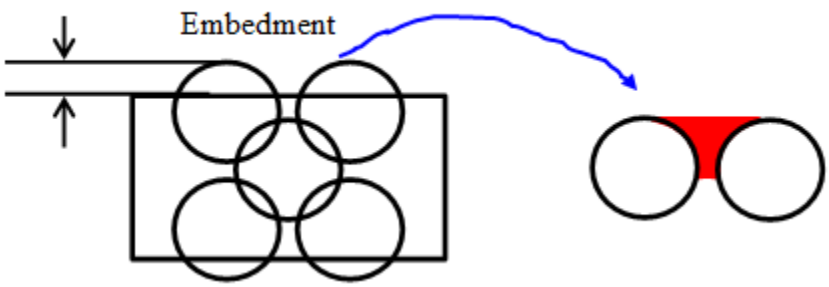

Fig. 5.44–Flow area of the proppant layer close to fracture wall.

5.7 Fracture Conductivity Correlation Considering Water Damage

In Section 4.6, a method to calculate the undamaged fracture conductivity in shale was proposed. The correlation to calculate the final conductivity considering the water damage can be written as,

$$C_f = 0.0185 \times \left(k_f w_f\right)^{1.5168} \quad \text{..... (5-1)}$$

Where,

$$k_f = 283.13 d_{50}{}^2 e^{-1.385\psi} \sigma^{-0.541} \quad \text{..... (5-2)}$$

$$\psi = \frac{d_{90} - d_{10}}{2} \quad \text{..... (5-3)}$$

$$w_f = w_0\left[1 - \left(\phi_0 - \phi_1\right)\left(1 - \phi_0\right)\right] - \frac{2.5 d_p}{\left(1 + \frac{4000E}{\sigma}\right)^{1.5}} \quad \text{..... (5-4)}$$

This correlation considers the proppant size, packing, sorting, crushing, grain rearrangement, proppant embedment as a function of rock mechanical property, and conductivity damage by water in shale fractures. The procedures to use this correlation are shown below:

(1) Acquire proppant size distribution by sieve analysis.

(2) Solve the population balance equation for proppant size distribution at each closure stress level, and read the median and phi-percentile deviation values.

(3) Calculate the undamaged fracture permeability using Eq. 5-2.

(4) Measure the initial fracture width or calculate the width with proppant porosity, specific gravity and areal concentration.

(5) Calculate fracture width under each closure stress using Eq. 5-4.

(6) Calculate the conductivity considering water damage using Eq. 5-1.

There are two limitations in using this correlation. First, the population balance equation needs to be solved at each stress level. So far, the population balance model only considers the crushing of natural sands. To account for the crushing behavior of ceramic or other artificial proppants, coefficients for the selection function and breakage function should be updated. Second, when considering the damage of water to conductivity, factors such as mineralogical components and mechanical parameters are all lumped into the empirical coefficients. This limits the application of this model only to the shale formations that have similar mineralogical and mechanical properties as the Barnett Shale with which the correlations are developed.

5.8 Chapter Summary

In this chapter, we first discussed the physical processes during the conductivity measurement by water. Understanding of the processes improves the experiment design such as water removal method. Then, some universal observations from the water experiments are presented providing direct evidence of conductivity impairment by water. The impact of rock type, shale fines migration, proppant fines migration, longer term rock creep, brine concentration, and residual water is analyzed individually. By the imaging techniques, evidence of shale fracture surface softening effect is provided. Based on the relationship between initial fracture conductivity and the recovered fracture conductivity, a new correlation to calculate shale fracture conductivity considering water damage is proposed.

6 CONCLUSIONS AND RECOMMENDATIONS

6.1 Conclusions

This dissertation presents a comprehensive study on hydraulic fracture conductivity in shale. We first discussed the conductivity of unpropped shale fractures, including natural fractures and artificially induced fractures. Then, propped fracture conductivity was investigated and a theoretical approach was proposed to calculate propped fracture conductivity. Finally, shale fracture conductivity damage by water was studied in great detail. The conclusions are summarized below:

(1) The laboratory procedures developed in this study can be utilized to reproducibly measure shale fracture conductivity by both gas and liquid. The conductivity measurement of unpropped fractures and propped fractures by small size proppants under ultra-low concentration requires strict control on gas flow bypassing the fracture both parallel and perpendicular to the fracture length direction. It proves to be effective by applying the pressure testing procedures recommended in this study and by matching the dimensions of the conductivity cell slot with the dimensions of the silicone rubber coating mold.

(2) Closure of the unpropped shale fractures includes the plastic mechanical compaction of the shale matrix laminations, the plastic deformation of the fracture surface asperity, and the linear compression of the shale matrix. The calcite-rich Eagle Ford Shale is the stiffest rock with the minimum strain comparing with the Barnett Shale, FL2 in the Fayetteville Shale, and FL3 in the Fayetteville Shale.

The mechanical behavior of the clay-rich Barnett Shale and the silica-rich Fayetteville Shale is dictated by the laminations and the rock sample structure.

(3) Unpropped natural fractures have conductivities of 0.10~2.50 md-ft at 4,000 psi closure stress. Its conductivity is either created by the fracture infill which is mainly anhydrite or by the unmatched fracture surfaces if the infill is not present. Unpropped aligned fractures are conductive only if the shale flakes and debris generated when inducing fractures are removed before the experiment. In this situation, unpropped aligned fracture conductivity is 0.15~0.30 md-ft at 3,000 psi. Unpropped displaced fractures create conductivities because the misalignment leaves residual fracture width. But due to the shale ductility, unpropped displaced fractures close up quickly. At 4,000 psi, the conductivity is 0.15~2.60 md-ft.

(4) Unpropped fracture conductivity is well correlated with shale rock brittleness. The most brittle FL2 in the Fayetteville Shale has the greatest unpropped conductivity while the ductile Barnett Shale and Eagle Ford Shale have unpropped conductivities that are 1~2 orders of magnitude smaller.

(5) Partial monolayer sand exists at the concentration of 0.03 lb/ft^2. The monolayer sand provides higher conductivity than multiple sand layers when stress is less than 2,000 psi. Elevated closure stress reduces the monolayer sand conductivity significantly due to the sand shear failure on the rough surface slopes. For multiple sand layers, larger sands always give higher conductivity at the same concentration; likewise the higher concentration with the same size sands.

(6) The Population-Balance-Equation based approach to calculate propped fracture conductivity considers the proppant properties, fracture design variables, and

formation properties. The predicted results give a reasonable match with the lab data.

(7) Clay content in shale rocks are the fundamental cause for the significant reduction of fracture conductivity after water flow. For the Barnett Shale, only 3%~20% of the original fracture conductivity can be recovered after the water damage. Shale fines migration and longer term rock creep each takes up about 20% of the reduction. Excessive proppant embedment due to shale fracture face softening is responsible for about 40% of the reduction. Other factors such as brine concentration and residual water content have limited impact on the conductivity damage. Proppant fines migration was not observed in this study.

(8) This study also shows that a fracture with higher initial conductivity can better overcome the conductivity damage by water than a fracture with low initial conductivity, because the damage by water occurs in the vicinity of the fracture walls. With a thick proppant pack, the internal proppant layers are the dominant flow area, and stay intact in the presence of water damage.

(9) A correlation to calculate fracture conductivity considering water damage is developed. This correlation expresses the power law relationship between the initial fracture conductivity and the recovered fracture conductivity after water damage.

6.2 Limitations and Recommendations

Further studies are needed to extend the scope of this work. Limitations of this study are summarized and recommendations for future study are also made:

(1) All the experiments were run at room temperature. The effect of formation temperature on the water damage process needs to be investigated in the future study.

(2) For water experiments, samples are only exposed to water for a short term. In the field, fractured shale wells might be soaked in fracturing fluid for a few months before the wells are flowed back and brought into production. So studies can also be performed to measure the long term fracture conductivity after the samples are exposed to water for months.

(3) In this study, experiments were run with water or brine. In shale fracturing design, linear gel or cross-linked gel can be pumped. It would be interesting to study the impact of the unbroken or partially broken gel.

REFERENCES

Andreev, G.E. 1995. Brittle Failure of Rock Materials: Test Results and Constitutive Models. Rotterdam, Netherlands: A.A. Bakema Publishers.

Ahmadi, M., Sharma, M. M., Pope, G.A., Torres, D.E., McCulley, C.A., and Linnemeyer, H. 2011. Chemical Treatment to Mitigate Condensate and Water Blocking in Gas Wells in Carbonate Reservoirs. *SPE Production & Operations*, 26(1): 67-74.

Austin, L.G. 1999. A Discussion of Equations for the Analysis of Batch Grinding Data. *Power Technology*, vol. 106: 71-77.

Awoleke, O., Romero, J., Zhu, D., and Hill, A.D. 2012. Experimental Investigation of Propped Fracture Conductivity in Tight Gas Reservoirs Using Factorial Design. Paper SPE 151963 presented at the SPE Hydraulic Fracturing Technology Conference, the Woodlands, Texas, U.S.A., 6-8 February.

Awoleke, O. 2013. Dynamic Fracture Conductivity: An Experimental Investigation Based on Factorial Analysis. PhD dissertation, Texas A&M University, College Station, Texas (May 2013).

Barree, R.D. and Conway, M.W. 2009. Multiphase Non-Darcy Flow in Proppant Packs. *SPE Production & Operations*, 24(2): 257-268.

Bass, V.L. 1954. Zur Theorie Der Mahlvorgange. *Zeitschrift für angewandte Mathematik und Physik*, 5(4): 283-292.

Berg. R.R. 1970. Method for Determining Permeability from Resrvoir Rock Properties. *Gulf Coast Association of Geological Societies Transactions*, Vol. 20: 303-317.

Blat, H., Tracy, R., and Owens, B. 2006. Petrology: Igneous, Sedimentary, and Metamorphic. New York: W.H.Freeman.

Branagan, P.T., Warpinski, N.R., Engler, B., and Wilmer, R. 1996. Measuring the Hydraulic Fracture-Induced Deformation of Reservoirs and Adjacent Rocks Employing a Deeply Buried Inclinometer Array: GRI/DOE Multi-Site Project. Paper SPE 36451 presented at the SPE Annual Technical Conference and Exhibition, Denver, Colorado, U.S.A., 6-9 October.

Brannon, H.D., Malone, M.R., Rickards, A.R., Wood, W.D., Edgeman, J.R., and Bryant, J.L. 2004. Maximizing Fracture Conductivity with Proppant Partial Monolayers: Theoretical Curiosity or Highly Productive Reality? Paper SPE 90698 presented at the SPE Annual Technical Conference and Exhibition, Houston, Texas, U.S.A., 26-29 September.

Broadbent, A.R. and Callcott T.G. 1956. A Matrix Analysis of Processes Involving Particle Assemblies. *Philosophical Transactions of the Royal Society A: Mathematical, Physical & Engineering Sciences*, vol. 149: 99-123.

Campbell, Q.P., Everson, R.C., Eyer, D., and Spamer, H.J. 1994. Spline Solution of the Continuous Batch Grinding Equation. *Minerals Engineering*, 8(4/5): 377-387.

Carman P.C. 1937. Fluid Flow Through Granular Beds. *Chemical Engineering Research and Design*, vol 75: S32-S48.

Chen, G. and Ewy, R.T. 2002. Investigation of the Undrained Loading Effect and Chemical Effect on Shale Stability. Paper SPE 78164 presented at the SPE/ISRM Rock Mechanics Conference, Irving, Texas, U.S.A., 20-23 October.

Chenevert M.E. and Sharma A.K. 1993. Permeability and Effective Pore Pressure of Shales. *SPE Drilling & Completion*, 8(1): 28-34.

Chester, J.S., Lenz, S.C., Chester, F.M., and Lang, R.A. 2004. Mechanisms of Compaction of Quartz Sand at Diagenetic Conditions. *Earth and Planetary Science Letters*, 220(3-4): 435-451.

Churcher, P.L., French, R.R., Shaw, J.C., and Schramm, L.L. 1991. Rock Properties of Berea Sandstone, Baker Dolomite, and Indiana Limestone. Paper SPE 21044 presented at the SPE International Symposium on Oilfield Chemistry, Anaheim, California, U.S.A., 20-22, February.

Cinco-Ley, H. and Samaniego-V, F. 1981. Transient Pressure Analysis for Fractured Wells. *Journal of Petroleum Technology*, 33(9): 1749-1766.

Cipolla, C.L., Lolon, E., Mayerhofer, M.J., and Warpinski, N.R. 2009. The Effect of Proppant Distribution and Un-Propped Fracture Conductivity on Well Performance in Uncenventional Gas Reservoirs. Paper SPE 119368 presented at the SPE Hydraulic Fracturing Technology Conference, the Woodlands, Texas, U.S.A., 19-21 January.

Civan, F. 2007. Reservoir Formation Damage. Houston, Texas: Gulf Publishing Company.

Committee on Fracture Characterization and Fluid Flow, National Research Council, 1996. Rock Fracture and Fluid Flow: Comtemporary Understanding and Applications. Washington, D.C: National Academy Press.

Conway M., Venditto J., Reilly P., and Smith K. 2011. An Examination of Clay Stabilization and Flow Stability in Various North American Gas Shales. Paper SPE 147266 presented at the SPE Annual Technical Conference and Exhibition, Denver, Colorado, U.S.A., 30 October-2 November.

Cooke Jr. C.E. 1973. Conductivity of Fracture Proppants in Multiple Layers. *Journal of Petroleum Technology*, 25(9): 1101-1107.

Cooke Jr. C.E. 1975. Effect of Fracturing Fluids on Fracture Conductivity. *Journal of Petroleum Technology*, 27(10): 1273-1282.

Coulter, G.R., Benton, E.G., and Thomson, C.L. 2004. Water Fracs and Sand Quantity: A Barnett Shale Example. Paper SPE 90891 presented at the SPE Annual Technical Conference and Exhibition, Houston, Texas, U.S.A., 26-29 September.

Cramer, D.D. 2008. Stimulating Unconventional Reservoirs: Lessons Learned, Successful Practices, Areas for Improvement. Paper SPE 114172 presented at the SPE Unconventional Reservoirs Conference, Keystone, Colorado, U.S.A., 10-12 February.

Daniels, J., Waters, G., Le Calvez, J.H., Bentley, D., and Lassek, J.T. 2007. Contacting More of the Barnett Shale Through an Integration of Real-Time Microseismic Monitoring, Petrophysics and Hydraulic Fracture Design. Paper SPE 110562 presented at the Annual Technical Conference and Exhibition held in Anaheim, California, U.S.A., 12-14 October 2007.

Darin, S.R. and Huitt, J.L. 1959. Effect of a Partial Monolayer of Proppant Agent on Fracture Flow Capacity. Paper SPE 1291 presented at the Annual Fall Meeting, Dallas, Texas, U.S.A., 4-7 October.

Deng, J., Mou, J., Hill, A.D., and Zhu, D. 2012. A New Correlation of Acid-Fracture Conductivity Subject to Closure Stress. *SPE Production & Operations*, 27(2): 158-169.

Detournay, E. and Cheng, A.H-D. 1988. Poroelastic Response of a Borehole in a Non-Hydrostatic Stress field. *International Journal of Rock Mechanics and Mining Sciences*, 25(3): 171-182.

Deville, J., Fritz, B., and Jarrett, M. 2011. Development of Water-Based Drilling Fluids Customized for Shale Reservoirs. *SPE Drilling & Completions*, 26(4): 484-491.

Ezzat, A.M. 1990. Completion Fluids Design Criteria and Current Technology Weakness. Paper SPE 19434 presented at the SPE Formation Damage Control Symposium, Lafayette, Louisiana, U.S.A., 22-23 February.

Fencher, G.H. 1941. Discussions on "The Permeability of Porous Media to Liquids and Gases". *Drilling and Production Practice*, 1 January, New York, New York.

Fredd, C.N., McConnell, S.B., Boney, C.L., and England, K.W. 2001. Experimental Study of Fracture Conductivity for Water-Fracturing and Conventional Fracturing Applications. *SPE Journal*, 6(3): 288-298.

Fritz, S.J. and Marine, I.W. 1983. Experimental Support for a Predictive Osmotic Model of Clay Membranes. *Geochemistry Cosmochim, ACTA*, 47(8): 1515-1522.

Gale, J.F., Reed, R.M., and Holder, J. 2007. Natural Fractures in the Barnett Shale and their Importance for Hydraulic Fracture Treatments. *AAPG Bulletin* 91(4): 603-622.

Gao, Y., Lv, Y., Wang, M., and Li, K. 2012. New Mathematical Models for Calculating the Proppant Embedment and Fracture Conductivity. Paper SPE 155954 presented at the SPE Annual Technical Conference and Exhibition, San Antonio, Texas, U.S.A., 8-10 October.

Gardner R.P. and Austin L.G. 1962. A Chemical Engineering Treatment of Batch Grinding. *Symposium on Size Reduction*, April 1962: 217-248.

Gidley, J.L., Penney, G.S., and McDaniel, R.R. 1995. Effect of Proppant Failure and Fines Migration on Conductivity of Propped Fractures. *SPE Production & Facilities*, 10(1): 20-25.

Gong, M., Lacote, S., and Hill, A.D. 1999. New Model of Acid-Fracture Conductivity Based on Deformation of Surface Asperities. *SPE Journal*, 4(3): 206-214.

Grieser, B., Hobbs, J., Hunter, J., and Ables, J. 2003. The Rocket Science Behind Water Frac Design. Paper SPE 80933 presented at the SPE Production and Operations Symposium, Oklahoma City, Oklahoma, U.S.A., 22-25 March.

Grim, R.E. 1968. Clay Mineralogy. New York: McGraw-Hill.

Gruesbeck, C. and Collins, R.E. 1982. Entrainment and Deposition of Fine Particles in Porous Media. *SPE Journal*, 22(6): 847-856.

Guimaraes, M. 2002. Crushed Stone Fines and Ion Removal From Clay Slurries-Fundamental Studies. PhD dissertation, Georgia Institute of Technology, Atlanta, Georgia (May 2002).

Guimaraes, M.S., Valdes, J.R., Palomino, A.M., and Santamarina, J.C. 2006. Aggregate Production: Fines Generation During Rock Crushing. *International Journal of Mineral Processing*, 81(4): 237-247.

Guin, J.A., Schechter, R.S., and Silbergerg, I.H. 1971. Chemically Induced Changes in Porous Media. *Industrial & Engineering Chemistry Fundamentals*, 10(1): 50-54.

Guo, Z., Chapman, M., and Li, X. 2012. Exploring the Effect of Fractures and Microstructure on Brittleness Index in the Barnett Shale. Paper SEG 2012-0771 presented at the 2012 SEG Annual Meeting in Las Vegas, Nevada, U.S.A., 4-9 November.

Hajiabdolmajid, V. and Kaiser, P. 2003. Brittleness of Rock and Stability Assessment in Hard Rock Tunneling. *Tunnelling and Underground Space Technology*, 18(1): 35-48.

Harpel, J., Barker, L., Frontenot, J., Carroll., C.L., Thomsan, S.L., and Olson, K.E. 2012. Case History of the Fayetteville Shale Completions. Paper SPE 152621 presented at the SPE Hydraulic Fracturing Technology Conference, the Woodlands, Texas, U.S.A., 6-8 February.

Hill, A.D. 1978. Flow with Simultaneous Heterogeneous Reactions in Porous Media. PhD dissertation, The University of Texas at Austin, Austin, Texas (May 1978).

Horner, P., Halldorson, B., and Slutz, J.A. 2011. Shale Gas Water Treatment Value Chain-A Review of Technologies, including Case Studies. Paper SPE 147264 presented at the SPE Annual Technical Conference and Exhibition, Denver, Colorada, U.S.A., 30 October-2 November.

Huang, H. and Ayoub, J. 2008. Applicability of the Forchheimer Equation for Non-Darcy Flow in Porous Media. *SPE Journal*, 13(1): 112-122.

Hughes, R.V. 1951. The Application of Modern Clay Concepts to Oil Field Development. *Drilling and Production Practice*, 1950: 151-167.

Huitt, J.L. and Mcglothlin Jr., B.B. 1958. The Propping of Fractures in Formations Susceptible to Propping-sand Embedment. *Drilling and Production Practice*: 115-123.

Jarvie, D., Hill, R.J., Ruble, T.E., and Pollastro, R.M. 2007. Unconventional Shale Gas Systems: the Mississippian Barnett Shale of North-Central Texas as One Model for Thermogenic Shale Gas Assessment. *AAPG Bulletin*, 91(4): 475-499.

Jones Jr., F.O. 1964. Influence of Chemical Composition of Water on Clay Blocking of Permeability. *Journal of Petroleum Technology*, 16(4): 441-446.

ISO 13503-2. 2006. *Petroleum and Natural Gas Industries-Completion Fluids and Materials-Part 2: Measurement of Properties of Proppants Used in Hydraulic Fracturing and Gravel-Packing Operations*. First Edition, 12 December.

ISO 13503-5. 2006. *Petroleum and Natural Gas Industries-Completion Fluids and Materials-Part 5: Procedures for Measuring the Long-Term Conductivity of Proppants*. First Edition, 1 July.

Kamenov, A. N. 2013. The Effect of Proppant Size and Concentration on Hydraulic Fracture Conductivity in Shale Reservoirs. MS thesis, Texas A&M University, College Station, Texas (May 2013).

Kapur, P.C. 1972. Kinetics of Granulation by Non-Random Coalesence Mehanism. *Chemical Enigneering Science*, 27(10): 1863-1869.

Karner, S.L., Chester, F.M., Kronenberg, A.K., and Chester, J.S. 2003. Subcritical Compaction and Yielding of Granular Quartz Sand. *Tectonophysics*, 277(2003): 357-381.

Karner, S., Chester, J.S., Chester, F.M., Kronenberg, A.K., and Hajash Jr., A. 2005. Laboratory Deformation of Granular Quartz Sand: Implication for the Burial of Clastic Rocks. *AAPG Bulletin*, 89(5): 603-625.

Kassis, S. and Sondergeld, C. 2010. Fracture Permeability of Gas Shale: Effects of Roughness, Fracture offset, Proppant, and Effective Stress. Paper SPE 131376 presented at the CPS/SPE International Oil & Gas Conference and Exhibition, Beijing, China, 8-10 June.

Khilar, C.K. and Fogler, H.S. 1983. Water Sensitivity of Sandstones. *SPE Journal*, 23(1): 55-64.

King, G.E. 2010. Thirty Years of Gas Shale Fracturing: What Have We Learned? Paper SPE 133456 presented at the SPE Annual Technical Conference and Exhibition, Florence, Italy, 19-22 September.

King, G.E., Haile, L., Shuss, J., and Dobkins, T.A. 2008. Increasing Fracture Path Complexity and Controlling Downward Fracture Growth in the Barnett Shale. Paper SPE 119896 presented at the SPE Shale Gas Production Conference, Fort Worth, Texas, U.S.A., 16-18 November.

King, R.P. 1972. An Analytical Solution to the Batch Comminution Equation. *Journal of the South African Institute of Mining and Metallurgy*, vol. 73: 127-131.

Klinkenberg, A.J. 1941. The Permeability of Porous Media to Liquids and Gases. *Drilling and Production Practice*, 1 January, New York, New York.

Kozeny, J. 1927. Ueber Kapillare Leitung Des Wassers Im Boden. *Sitzungsberichte Wiener Akademie*, 136(2a): 271-306.

Lin, S. and Lai, B. 2013. Experimental Investigation of Water Saturation Effects on Barnett Shale's Geomechanical Behaviors. Paper SPE 166234 presented at the SPE Annual Technical Conference and Exhibition, New Orleans, Louisiana, U.S.A., 30 September-2 October.

Lobo-Guerrero, S. and Vallejo, L.E. 2005. Discrete Element Method Evauation of Granular Crushing under Direct Shear Test Conditions. *Jornal of Geotechnical and Geoenvironmental Engineering*, 131(10):1295-1300.

Low, P.F. 1961. Physical Chemistry of Clay-Water Interaction. *Advances in Agronomy*, vol. 13: 269-327.

Low, P.F. and Anderson, D.M. 1958. Osmotic Pressure Equation for Determining Thermodynamic Properties of Soil Water. *Soil Science*, 86(5): 251-253.

Lucas, P.W. and Luke, D.A. 1983. Methods for Analysing the Breakdown of Food in Human Mastication. *Archives of Oral Biology*, 28(9): 813-819.

Mahadevan, J. and Sharma, M.M. 2003. Clean-up of Water Blocks in Low Permeability Formations. Paper SPE 84216 presented at the SPE Annual Technical Conference and Exhibition, Denver, Colorado, U.S.A., 5-8 October.

Maqbool, T. 2011. Understanding the Kinetics of Asphaltene Precipitation from Crude Oils. PhD dissertation, The University of Michigan, Ann Arbor, Michigan (2011).

Marpaung, F., Chen, F., Pongthunya, P., Zhu, D., and Hill, A.D. 2008. Measurement of Gel Cleanup in a Propped Fracture with Dynamic Fracture Conductivity Experiments. Paper SPE 115653 presented at the SPE Annual Technical Conference and Exhibition, Denver, Colorado, U.S.A., 21-24 September.

Mayerhofer, M.J., Richardson, M.F., Walker Jr., R.N., Meehan, D.N., Oehler, M.W., and Browning Jr., R.R. 1997. Proppants? We Don't Need No Proppants. Paper SPE 38611 presented at the SPE Annual Technical Conference and Exhibition, San Antonio, Texas, U.S.A., 5-8 October.

Mayerhofer, M.J., Lolon, E.P., Youngblood, J.E., and Heinze, J.R. 2006. Integration of Microseismic-Fracture-Mapping Results With Numerical Fracture Network Production Modeling in the Barnett Shale. Paper SPE 102103 presented at the SPE Annual Technical Conference and Exhibition, San Antonio, Texas, U.S.A, 24-27 September.

McDowell, G.R. and Bolton, M.D. 1998. On the Mechanics of Crushable Aggregates. *Geotechnique*, 48(5): 667-679.

Menendez, B., Zhu, W., and Wong, T.F. 1996. Micromechanics of Brittle Faulting and Cataclastic Flow in Berea Sandstone. *Journal of Structural Geology*, 18(1): 1-16.

Mishra, B.K. 1999. Monte Carlo Simulation of Particle Breakage Process During Grinding. *Powder Technology*, vol. 110: 246-252.

Mody, F.K. and Hale, A.H. 1993. A Borehole Stability Model to Couple the Mechanics and Chemistry of Drilling Fluid Shale Interaction. Paper SPE/IADC 25728 presented at the 1993 SPE/IADC Drilling Conference, Amsterdam, the Netherlands, 23-25 February.

Morales, R.H., Suarez-Rivera, R., and Edelman, E. 2011. Experimental Evaluation of Hydraulic Fracture Impairment in Shale Reservoirs. Paper ARMA 11-380 presented at the 45th US Rock Mechanics / Geomechanics Symposium, San Francisco, California, U.S.A., 26-29 June.

Mou, J., Hill, A.D., and Zhu, D. 2011. New Correlations of Acid-Fracture Conductivity at Low Closure Stress Based on the Spatial Distribution of Formation Properties. *SPE Production & Operations*, 26(2): 195-202.

Mueche, T.W. 1979. Formation Fines and Factors Controlling Their Movement in Porous Media. *Journal of Petroleum Technology*, 31(2): 144-150.

Mungan, N. 1989. Discussion of an Overview of Fromation Damage. *Journal of Petroleum Technology*, 41(11):1224.

Navarrete, R.C., Holms, B.A., McConnell, S.B., and Linton, D.E. 1998. Emulsified Acid Enhances Well Production in High-Temperature Carbonate Formations. Paper SPE 50612 presented at the European Petroleum Conference, the Hague, Netherlands, 20-22 October.

Nierode, D.E. and Kruk, K.F. 1973. An Evaluation of Acid Fluid Loss Additives Retarded Acids, and Acidized Fracture Conductivity. Paper SPE 4549 presented at the Fall Meeting of the Society of Petroleum Engineers of AIME, Las Vegas, Nevada, U.S.A., 30 September-3 October.

Ramkrishna, D. 2000. Population Balances: Theory and Applications to Particular Sytems in Engineering. San Diego, California: Academic Press.

Ramurthy, M., Barree, R.D., Kundert, D.P., Petre, E., and Mullen, M. 2011. Surface-Area vs Conductivity-Type Fracture Treatments in Shale Reservoirs. *SPE Production and Operations*, 26(4): 357-367.

Reed, M.G. 1977. Formation Permeability Damage by Mica Alteration and Carbonate Dissolution. *Journal of Petroleum Technology*, 29(9): 1056-1060.

Reed, M.G. 1980. Gravel Pack and Formation Sandstone Dissolution During Steam Injection. *Journal of Petroleum Technology*, 32(6): 941-949.

Reid, K.J. 1965. A Solution to the Batch Grinding Equation. *Chemical Engineering Science*, vol. 20: 953-963.

Rivers, M., Zhu, D., and Hill, A.D. 2012. Proppant Fracture Conductivity with High Proppant Loading and High Closure Stress. Paper SPE 151972 presented at the SPE Hydraulic Fracturing Technology Conference, the Woodlands, Texas, U.S.A., 6-8 February.

Ouyang, L. 2013. Theoretical and Numerical Simulation of Non-Newtonian Fluid Flow in Propped Fractures. PhD dissertation, Texas A&M University, College Station, Texas (December 2013).

Palisch, T., Duenckel, R., Bazan, L., Heidt, J.H., and Turk, G.A. 2007. Determining Realistic Fracture Conductivity and Understanding its Impact on Well Performance. Paper SPE 106301 presented at the SPE Hydraulic Fracturing Technology Conference, College Station, Texas, U.S.A., 29-31 January.

Palisch, T., Duenckel, R., Chapman, M., Woolfolk, S., and Vincent, M.C. 2010. How to Use and Misuse Proppant Crush Tests: Exposing the Top 10 Myths. *SPE Production & Operations*, 25(3): 345-354.

Palisch, T.T., Vincent, M.C., and Handren, P.J. 2010. Slickwater Fracturing: Food for Thought. *SPE Production & Operations*, 25(3):327-344.

Papazis, P.K. 2005. Petrographic Characterization of the Barnett Shale, Fort Worth Basin, Texas. MS Thesis. The University of Texas at Austin, Austin, Texas (August 2005).

Parker, M.A. and McDaniel, B.W. 1987. Fracturing Treatment Design Improved by Conductivity Measurements Under In-Situ Conditions. Paper SPE 16907 presented at the SPE Annual Technical Conference and Exhibition, Dallas, Texas, U.S.A., 27-30 September.

Parker, M., Glasbergen, G., van Batenburg, D.W., Weaver, J.D., and Slabaugh, B.F. 2005. High-Porosity Fractures Yield High Conductivity. Paper SPE 96848 presented at the SPE Annual Technical Conference and Exhibition, Dallas, Texas, U.S.A., 9-12 October.

Peterson, T.W. 1986. Similarity Solutions for the Population Balance Equation Describing Particle Fragmentation. *Aerosol Science and Technology*, vol. 5: 93-101.

Portas, R.M. and Slatt, R. 2010. Characterization and Origin of Fracture Pattern in a Woodford Shale Quarry in Southeastern Oklahoma for Application to Exploration and Development. Search and Discovery Article 50352 adapted to poster presentation at AAPG Annual Convention and Exhibition, New Orleans, Louisiana, U.S.A., 11-14 April.

Pournik, M., Zou, C., Malagon Nieto, C., Melendez, M.G., Zhu, D., Hill, A.D., and Weng, X. 2007. Small-Scale Fracture Conductivity Created by Modern Acid Fracture Fluids. Paper SPE 106272 presented at the SPE Hydraulic Fracturing Technology Conference, College Station, Texas, U.S.A., 29-31 January.

Sanchez, M. 2013. Classnotes of “Transport Phenomena in Porous Media”.

Sharma, M.M., Yortsos, Y.C., and Handy, L.L. 1985. Release and Deposition of Clays in Sandstones. Paper SPE 13562 presented at the SPE Oilfield and Geothermal Chemistry Symposium, Phoenix, Arizona, U.S.A., 9-11 March.

Sharma, M.M. and Yortsos, Y.C. 1986. Permeability Impairment Due to Fines Migration in Sandstones. Paper SPE 14819 presented at the 7th Symposium on Formation Damage Control, Lafayette, Louisiana, U.S.A., 26-27 February.

Shelley, B., Grieser, B., Johnson, B. J Fielder, E.O., Heinze, R.J., and Werline, J.R. 2008. Data Analysis of Barnett Shale Completions. *SPE Journal*, 13(3):366-374. SPE-100674-PA.

Terzaghi, K. 1928. The Physical Properties of Clays. *M.I.T. Technology and Engineering News*, vol. 9: 10-11, 36.

Tek, M.R., Coats, K.H., and Katz, D.L. 1962. The Effect of Turbulence on Flow of Natural Gas Through Porous Reservoirs. *Journal of Petroleum Technology*, 14(7): 799-806.

Tscapek, W. 1934. The Density of Adsorbed Water in Soils. *Z. Pflanzenernahr. Dung. Bodenk*, vol. 34: 265-271.

Van Dam, D.B. and de Pater, C.J. 1999. Roughness of Hydraulic Fractures: The Importance of In-Situ Stress and Tip Processes. Paper SPE 56596 presented at the SPE Annual Technical Conference and Exhibition, Houston, Texas, U.S.A., 3-6 October.

Varacchi, B., Jaiswal, P., Puckette, J., and Dvorkin, J. 2012. Elastic Properties of Silica-Rich Mudrocks: Woodford Shale, Andarko Basin, Oklahoma. Paper SEG 2012-1230 presented at the 2012 SEG Annual Meeting, Las Vegas, Nevada, U.S.A., 4-9 November.

Vincent, M.C. 2002. Proving It - A Review of 80 Published Field Studies Demonstrating the Importance of Increased Fracture Conductivity. Paper SPE 77675 presented at the SPE Annual Technical Conference and Exhibition, San Antonio, Texas, U.S.A., 29 September-2 October.

Wang, F.P. and Gale, J.F.W. 2009. Screening Criteria for Shale Gas Systems. *Gulf Coast Association of Geological Societies Transactions*, vol. 59, 779-793.

Warpinski, N.R. 2009. Stress Amplification and Arch Dimensions in Proppant Beds Deposited by Waterfracs. *SPE Production & Operations*, 25(4): 461-471. SPE-119350-PA.

Wiley, C., Barree, B., Eberhard, M., and Lantz, T. 2004. Improved Horizontal Well Stimulations in the Bakken Formation, Williston Basin, Montana. Paper SPE

90697 presented at the SPE Annual Technical Conference and Exhibition, Houston, Texas, U.S.A., 26-29 September.

Zhang, J. 2005. The Impact of Shale Properties on Wellbore Stability. PhD dissertation, The University of Texas at Austin, Austin, Texas (August 2005).

Zhang, J., Kamenov, A., Zhu, D., and Hill, A.D. 2013a. Laboratory Measurement of Hydraulic Fracture Conductivities in the Barnett Shale. Paper SPE 163839 Presented at the SPE Hydraulic Fracturing Technology Conference in the Woodlands, Texas, U.S.A., 4-6 February.

Zhang, Q., Zhu, D., and Hill, A.D. 2013b. Modeling of Spent-Acid Blockage Damage in Stimulated Gas Wells. Paper IPTC 16481 presented at the International Petroleum Technology Conference in Beijing, China, 26-28 March.

APPENDIX A

Procedures for Recording Gas Flow Rate Using TIO

Totalizer Input/Output Controller package (TIO) is the device attached to the gas flow controller to record the total gas volume flowed through the fracture and to output digital flow rates into the configuration and monitoring utility software. **Fig. A.1** shows the TIO package attached to the gas flow controller.

Fig. A.1–Totalizer Input/Output Controller package attached to the gas flow controller.

The software package can be installed on a PC to record the flow rate and gas accumulation over time. Steps to use the software are shown in **Fig. A.2**.

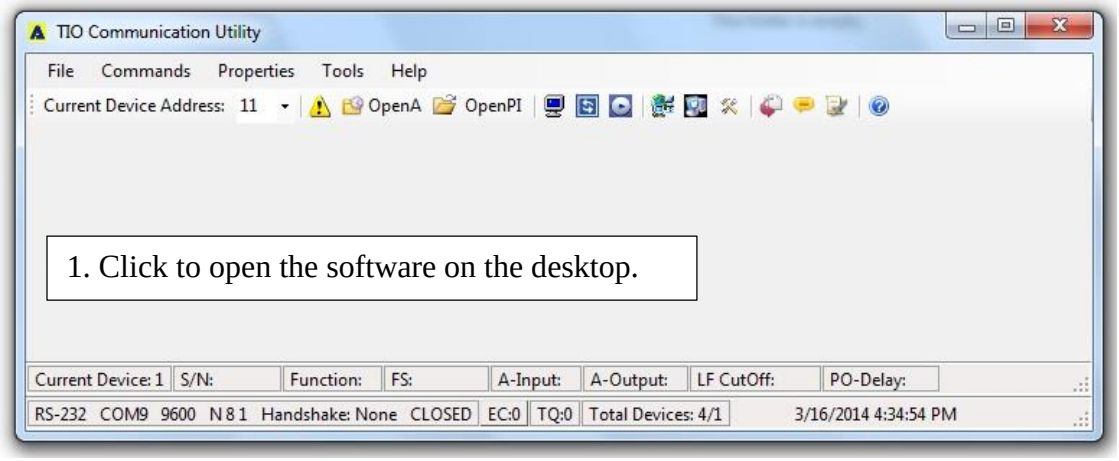

(a)

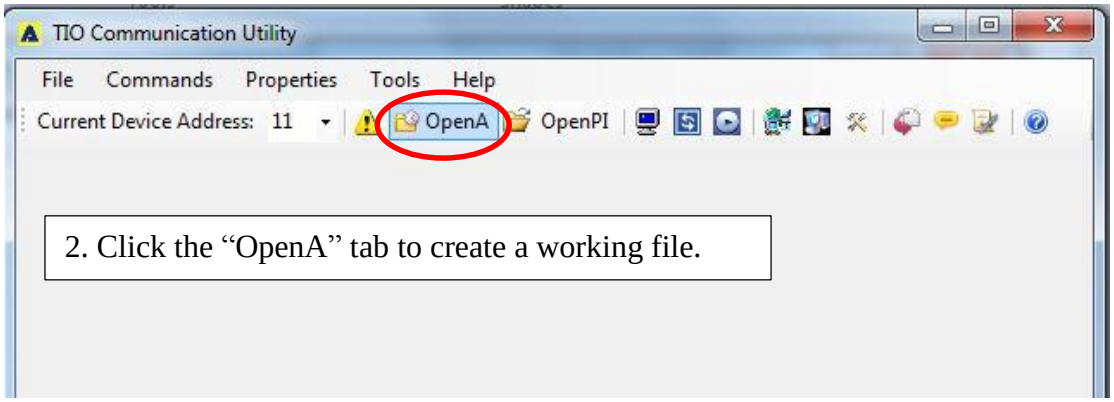

(b)

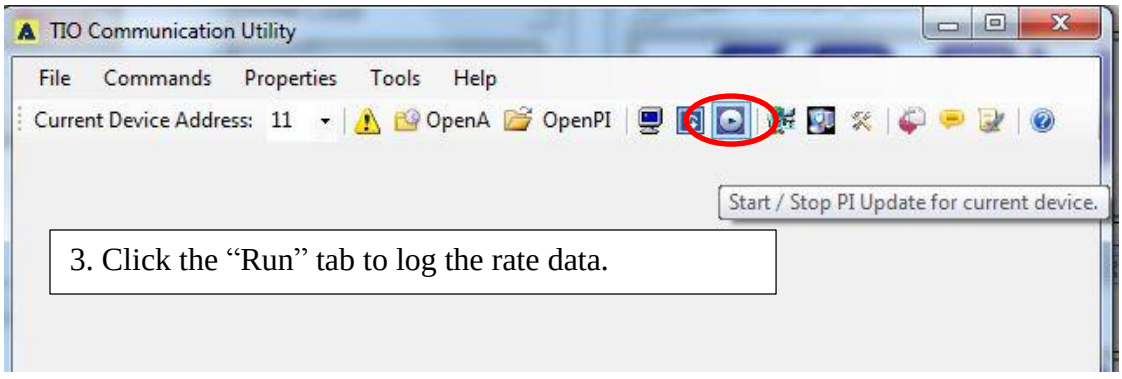

(c)

Fig. A.2–Procedures to record gas flow rate data using TIO software package.

APPENDIX B

Specifications of the Main Components in the Experimental Apparatus

Table B.1 contains the main components in the conductivity measurement setup, including the item, connection type, part number and the vendor. Product specifications, pressure and temperature ratings can be found in the online product catalogs.

Table B.1–List of the components in the laboratory setup.

No.	Item	Connection	Part No.	Vendor	Notes
1	Hydraulic load frame			GCTS	Compression/tension loading system
2	Gas flow controller	1/4" tubing fitting		Aalborg	Maximum differential pressure 100 psi
3	TIO	Vendor provided	TIOS-010001	Aalborg	
4	Conductivity cell assembly	316 stainless steel		Low Speed Wind Tunnel, TAMU	Maximum closure stress tested to 10,000 psi; maximum temperature 300 °F.
5	Pressure sensors		DP-15	Validyne Engineering	
6	Rock samples			Kocurek Industries: Hard Rock Division	Call Steve Kocurek for specific core shaping and quotation.
7	Medium-flow metering valve	1/4" tubing fitting, 316 stainless steel	SS-31-RS4	Swagelok	Used as back pressure valve.
8	Quarter-turn Plug	1/4" tubing fitting, 316 stainless steel	SS-4P4T	Swagelok	Connected to pressure sensors and flow lines.
9	In-line particulate filter	1/4" tubing fitting, 316 stainless steel	SS-4F-40	Swagelok	Connected to pressure sensors and the outflow end.
10	Poppet check valve	1/4" tubing fitting, 316 stainless steel	SS-4C-1	Swagelok	Connected to the gas flow controller and the union cross at the gas-flow end.

No.	Item	Connection	Part No.	Vendor	Notes
11	Union elbow	1/4" tubing fitting, 316 stainless steel	SS-400-9	Swagelok	
12	Union cross	1/4" tubing fitting, 316 stainless steel	SS-400-4	Swagelok	
13	Port connector	1/4" tubing fitting, 316 stainless steel	SS-401-PC	Swagelok	
14	PTFE-lined, braided hose	1/4" tubing fitting, 316 stainless steel	SS-4BHT-24	Swagelok	
15	Union tee	1/4" tubing fitting, 316 stainless steel	SS-400-3	Swagelok	
16	Nitrogen tank				Industrial grade dry nitrogen; talk to facilities manager for refill.
17	Silicone rubber		RTV 627 (2 PT KIT)	R.H. Hughes (Distributor)	Momentive is the manufacturer; it can be purchased from many distributors.
18	Primer		SS 4155	R.H. Hughes (Distributor)	Help the silicone rubber attach to the rock.

APPENDIX C

Discretized Population Balance Equation for Size Reduction

The population balance equation for size reduction takes the form of,

$$\frac{\partial}{\partial x}\left[\frac{\partial P(x,\sigma)}{\partial \sigma}\right] = -S(x)\frac{\partial P(x,\sigma)}{\partial x} + \int_{y=x}^{x_{max}} \frac{\partial B(y,x)}{\partial x}\frac{\partial P(y,\sigma)}{\partial y} S(y)dy \quad \text{..... (C-1)}$$

Discretizing the equation,

$$L.H.S = \frac{1}{\Delta\sigma\Delta x}\left[\left(P_i^n - P_i^{n-1}\right) - \left(P_{i-1}^n - P_{i-1}^{n-1}\right)\right] \text{..... (C-2)}$$

$$R.H.S = -S_i^n \frac{P_i^n - P_{i-1}^{n-1}}{\Delta x} + \sum \bar{S}_j^n \left(\frac{P_j^n - P_{j-1}^{n-1}}{\Delta y}\right)\left(\frac{B_{j,i}^n - B_{j,i-1}^n}{\Delta x}\right)\Delta y \text{..... (C-3)}$$

Assuming $\Delta x = \Delta y$,

$$\begin{aligned}&\frac{1}{\Delta\sigma\Delta x}\left[\left(P_i^n - P_i^{n-1}\right) - \left(P_{i-1}^n - P_{i-1}^{n-1}\right)\right] \\ &= -S_i^t \frac{P_i^n - P_{i-1}^{n-1}}{\Delta x} + \sum \bar{S}_i^n \left(\frac{P_i^n - P_{i-1}^{n-1}}{\Delta x}\right)\left(\frac{B_{j,i}^n - B_{j,i-1}^n}{\Delta x}\right)\Delta x\end{aligned} \quad \text{.....(C-4)}$$

Rearranging,

$$\begin{aligned}P_i^n &= -S_i^n\left(P_i^n - P_{i-1}^{n-1}\right)\Delta\sigma \\ &+ \sum \bar{S}_i^n \left(P_i^n - P_{i-1}^{n-1}\right)\left(B_{j,i}^n - B_{j,i-1}^n\right)\Delta\sigma + \left(P_{i-1}^n - P_{i-1}^{n-1}\right) + P_i^{n-1}\end{aligned} \quad \text{.....(C-5)}$$

The initial condition is,

$$P_i^n\Big|_{n=0} = P_i^0 \quad \text{.....(C-6)}$$

The boundary condition is,

$$P_i^n\Big|_{i=1(x=x_{max})} = 1 \quad \text{.....(C-7)}$$